Auxetic power amplification mechanisms for low frequency vibration energy harvesting

Submitted by William Ferguson

to the University of Exeter

as a thesis for the degree of

Doctor of Philosophy in Engineering

in March 2020

I certify that all material in this thesis which is not my own work has been identified and that no material has previously been submitted and approved for the award of a degree by this or any other University.

Signature: William Ferguson

Abstract

Energy harvesting from locally available small amplitude vibrations can struggle to generate sufficient power for wireless sensor nodes, which thereby constrains their use for structural health monitoring. This work discusses a selection of two-dimensional auxetic substrate designs used to increase a piezoelectric harvester's power output by 2.18-14.5 times by concentrating the ambient strain energy into the piezoelectric material. The harvesters were modelled and their auxetic designs optimised in COMSOL before empirical testing under sinusoidal or dynamic strain oscillations. The investigated auxetic designs included re-entrant honeycombs, rotating squares, triangles and hexagrams, and I-hole structures; the most effective of which was found to be the honeycomb design, with a gain of 5.66 and a raw output of 570 μW at 10 Hz, 100 με. This work also compared PZT (Lead Zirconate Titanate), LN (Lithium Niobate), and MFC (Macro-Fibre Composite) as materials for the active piezoelectric layer. The former was found to be detrimentally brittle but delivered the greatest output, while the LN was stronger but with a significantly lower output. The MFC was more flexible, with only a modest reduction in output compared to PZT, and was found to be the most viable of these materials for future research. A crucial issue during the design stages was appropriately modelling the mechanical losses associated with the bonding between substrate and piezoelectric material; this adhesion was modelled using thin elastic layers (TELs) to emulate each sample by comparing to its output. The value of the stiffness constant per unit area in these TELs was found to be consistent for each sample across a range of input excitations. These kinds of energy harvesters open up many new avenues for wireless self-powered structural health monitoring sensor nodes in infrastructure, buildings, and vehicles, where the ambient vibration energy would otherwise be too diffuse to harvest from.

Acknowledgements

I wish to thank my supervisors, my fellows in the Energy Harvesting Group, all those involved in the Centre of Doctoral Training in Metamaterials (of which I am an associate), and the EPSRC DTP for providing the finances for this work (grant numbers: EP/N509656/1 & EP/L015331/1). I am also indebted to Ausrine Bartasyte and Giacomo Clementi for the opportunity to test their lithium niobate material (see chapter 4). Most of all I'd like to thank all those who supported me throughout this endeavour.

Contents

List of Figures

List of Tables

List of Common Symbols

$\blacksquare_i$	Subscript Indicates Electrical Polarisation Axis	–
$\blacksquare_j$	Subscript Indicates Mechanical Action Axis	–
E_i	Electrical Field	V/m
D_i	Electric Displacement Field	C/m^2
T_j	Stress in *j* Direction	N/m^2 (or Pa)
S_j	Strain in *j* Direction	– (or με i.e. 'micro-strain')
s_{ij}^E	Elastic Compliance	m^2/N
d_{ij}	Piezoelectric Charge Coefficient	V/m (or C/N)
e_{ij}	Piezoelectric Strain–Flux Coefficient	N/Vm
g_{ij}	Piezoelectric Voltage Coefficient	Vm/N
h_{ij}	Piezoelectric Electric Field–Strain Coefficient	m/V
ε_0	Permittivity of Free Space	8.854…×10^{-12} F/m
ε_{ij}	Relative Permittivity	–
ρ_x	Material *x*'s Density	kg/m^3
ν_x	Material *x*'s Poisson Ratio	–
E_x	Material *x*'s Elastic (Young's) Modulus	N/m^2 (or Pa)
P_{Opt}	Optimal Power Output	W
R_{Opt}	Optimal Load Resistance	Ω
π	Mathematical Circle Constant	3.1415926535…
f	Excitation Frequency	Hz
L_p	Length of Piezoelectric Layer	m
W_p	Width of Piezoelectric Layer	m
A_p	Area of Piezoelectric Layer ($L_p \times W_p$)	m^2
t_p	Thickness of Piezoelectric Layer	m
t_g	Thickness of Glue (Epoxy) Layer	m
k_a	Spring constant per unit area in Thin Elastic Layer	N/m^3
L_s	Length of Substrate	m
W_s	Width of Substrate	m

t_s	Thickness of Substrate	m
L_{clp}	Length of Clamping Region	m
W_{clp}	Width of Clamping Region	m
L_{AR}	Length of Auxetic Region	m
L_{buf}	Length of Auxetic Region Buffer	m
L_c	Cell Length of Re-Entrant Honeycomb	m
H_c	Cell Height of Re-Entrant Honeycomb	m
M	Number of Re-Entrant Honeycomb Cells in W_s	–
N	Number of Re-Entrant Honeycomb Cells in L_{AR}	–
t_b	Thickness of Beams in Re-Entrant Honeycomb	m
t_j	Adjustment to t_b	m
α	Cell Angle in Re-Entrant Honeycomb	°
d	Deformation Ratio in Re-Entrant Honeycomb	%
def	Deformation Length in Re-Entrant Honeycomb	m
cb	Crossbeam Ratio in Re-Entrant Honeycomb	%
CB	Crossbeam Length in Re-Entrant Honeycomb	m
fr	Fillet Radius in Re-Entrant Honeycomb	m
h_A	Baseline Elliptical Slit Semimajor Axis Length	m
h_a	Crossing Elliptical Slit Semimajor Axis Length	m
h_b	Elliptical Slit Semiminor Axis Width	m
r	Slit Length Ratio ($h_a = h_A \times r$)	%
R	Slit Grid Spacing Ratio	%
θ	Slit Crossing Angle Relative to Baseline	°
φ	Grid Baseline Angle Relative to Substrate Axis	°
sep_{ax}	I-Hole Axial Spacing	m
sep_{lat}	I-Hole Lateral Spacing	m

1 Introduction

1.1 Context and Motivation

There are many scenarios in which it may be desirable to acquire sensor data about a local environment, e.g. structural health monitoring of a building or machine, a pervasive sensor network, or wearable medical instruments, which may not otherwise have a suitable power supply. Both wired and battery powered sensors may be undesirable or impractical in many cases; for example, in the former instance retrofitting sensors and wires may be too difficult or a grid supply may be unavailable, and in the latter case there would be a requirement for regular replacement or perhaps a risk due to chemical reactivity. The current generation of energy harvesting devices may have difficulty in some locations to extract sufficient ambient energy to power most sensors of interest. This thesis presents work on a new generation of energy harvesting devices which concentrate the environmental strain energy into a more potent power supply.

1.2 Aim and Objectives

The aim of this work was to increase the power output of a vibration energy harvester, by using auxetic components to concentrate the ambient mechanical energy into the harvester and thus harness it more effectively. This would facilitate a sensor and its associated electronics (i.e. a sensor node) which are better able to power themselves using ambient energy, thereby opening up new locations as viable sources for self-powered sensor nodes.

The objectives were to have:

- A finite element model of an auxetic harvester for power output prediction.
- An optimised auxetic design from this model, which maximised power output within tolerable stress limits.
- Model validation through experimental tests of this design.
- A baseline non-auxetic design of the same size and material.
- Comparisons with alternative transducer and substrate materials, and types of auxetic structure.

1.3 Thesis Structure

The following chapter surveys the background literature on the topics of: energy harvesting (focusing primarily on vibration energy harvesting); piezoelectric materials; and auxetic materials. Finally, these three topics are brought together with a review auxetic and piezoelectric materials used for vibration energy harvesting.

Chapter 3 discusses an initial proof of concept work into this combination. This strain energy harvester, with an auxetic re-entrant hexagonal structure under the piezoelectric layer, PZT, was designed with finite element simulations, then manufactured and subjected to harmonic strain excitations. This framework was found to increase the power output by up to 14.5 times a baseline plain design (up to 202 vs. 14.1 μW at 10 Hz, 250 με) at any viable input excitation amplitude or frequency. The model was validated effective, provided appropriate values for adhesion strength are included. The power increase encouraged further work, but the damage to the PZT under a modest force (230 N at most for the auxetic samples) led to a need for a stronger material.

To this end, lithium niobate (LN) replaced PZT as the piezoelectric material, as discussed in chapter 4. This material was kindly supplied by the Femto-ST institute through Ausrine Bartasyte and Giacomo Clementi. It proved more resilient (the auxetic sample withstood 500 με, equivalent to 415 N), but produced less power (25 vs. 7.5 μW at 10 Hz, 250 με) and a smaller gain of 3.3 times. An alternative way to increase the power output was therefore desirable

Making the harvester larger would allow it to produce more power and use more complex auxetic designs. Chapter 5 discusses how a design developed from the proof of concept with multiple re-entrant units was built and optimised in the model, and how it was tested experimentally. Tests using bulk ceramic PZT layers were compared to the same designs with piezoelectric-composite MFC layers. The PZT produced more power (auxetic: PZT: 623 & MFC: 468 vs. plain: PZT: 100 & MFC: 47 μW at 100 με and 10 Hz), but the gain using MFC was greater: 6.2 vs. 11.8 times, and so these were taken on to the final stage of work.

The final technical phase of this work, chapter 6, discusses modelling and testing of a variety of other auxetic designs using these MFC layers on longer

aluminium substrates. The optimised designs (appended with experimental gains over the plain baseline output of 100.7 μW at 10 Hz, 100 με) were the re-entrant honeycomb array again (gain of 5.66×), the rotating triangles (5.29×), the rotating rhomboids (3.24×), the I-holes (2.18×), and the rotating hexagrams (4.35×). The finite element model was found to be applicable to all these designs. Any one of these would be suitable for energy harvesting applications.

The general discussion, drawing all this work together, is in chapter 7. The final conclusions are given in chapter 8, with some suggestions for future researchers wishing to build on this work in chapter 9.

1.4 Research Contribution

This research demonstrates an effective new means of increasing the power output for strain driven vibration energy harvesters using auxetic designs. These could be used to power monitoring devices in infrastructure, buildings, vehicles and elsewhere, to provide stakeholders with information about their current state and advanced warning of any damage. This thesis also demonstrates the efficacy of finite element modelling for this endeavour, providing the research community with a reliable method for generating improved designs in future.

This research has been presented at several conferences: Energy Harvesting Network, 2017; Materials Research Exchange, 2018; PSMA Inaugural International Energy Harvesting Workshop, 2018; and the Materials for Clean Energy Conference, 2019. The work in chapter 3 has been previously published as '*Auxetic structure for increased power output of strain vibration energy harvester*' by Ferguson, et al.[1], and the work discussed in chapter 6 is due to be in included as a chapter in '*Energy Harvesting in Wireless Sensor Networks and Internet of Things*', edited by Faisal Karim Shaikh and Sherali Zeadally.

2 Background and Literature Review

2.1 Energy Harvesting

2.1.1 Overview and Applications

Energy harvesting is concerned with collecting small amounts of power from surrounding sources and converting this into usable electrical power (typically on the scale of a few hundred μW to tens of mW, though in some cases it may reach a few Watts)[2–6]. Sources include ambient or mechanical vibrations[1,2,5–14], thermal gradients[2,5,11], background radio and microwaves[8,15], fluid currents[2,8,10,16–23], and the human body for wearable applications (such as charging a battery by walking)[8,10,24–26]. Other works may dub this field 'energy scavenging'; the distinction (where made) is that harvested sources can be well characterised in advance, while scavengers operate in more unknown or unpredictable environment where drawing on multiple surrounding sources may be necessary[5]. Although the phrase 'energy harvesting' could arguably encompass many grid-scale renewable energy technologies that take energy from their environment, these are considered a distinct field due to their much larger scale[17,27].

The main application of energy harvesting is to power systems for remotely monitoring an area for changes over a long timescale[2,28–30]; typified by structural health monitoring. This uses sensors to record measurements of the environment to notify maintenance engineers of any changes which could indicate structural damage, along with its location and severity[2,12,20,28–32]. This could for example be used throughout a building or bridge to give advance warning of cracks before they become visible[12]; under a train to monitor the condition of the train's undercarriage as well as of the tracks[28,33]; detecting leaks in a pipeline[20,31]; in an aircraft to detect growing fatigue in the fuselage, wings, or fuel tanks[32]. Many companies find this kind of asset management or predictive maintenance preferable to bi-annual checks or scheduled replacements (which could miss rapidly developing faults or lead to functional equipment being scrapped)[32].

Another use of energy harvesting could be powering many mobile and wearable devices[8,34–36]. These could include medical devices (e.g. sensors monitoring heart rate, activity, or glucose levels), inertial measurement for a low-power supplement to GPS positioning in cars and animal trackers, or more aesthetic devices (such as light up heels powered by walking)[8,34–36]. Such

harvesters could also provide a secondary power source to portable devices, such as phones, watches, and wireless peripherals[24] (potentially becoming 'batteryless' altogether in lower-power devices[6,37,38]). There is ongoing research into recharging the batteries in pacemakers using the body's motion (reducing the number of invasive surgeries to change them)[36,39]. Harvesting devices might one day be used as internal backups for mains powered systems, recovering and storing some wasted energy for use in an emergency. An energy harvester could also serve as independent power supply to a smoke detector[40], or maintaining safety and security detectors.

One major advantage to an energy harvesting system is that it does not require wires, either for power or data transmission[2,10,12,20,28–32,37]. This makes retrofitting into existing structures much easier, as well as subsequent node repositioning or expansion of the network[2,10,12,29,32,37]. In the use case of buildings and infrastructure, the process of wiring sensors into them could involve hundreds, or even thousands, of meters of cable[32]. Even during initial construction this would be an expensive proposition, let alone retrofitting additional cables into an existing structure. There are also many older buildings where the appearance of wiring would be undesirable[41]. In the case of vehicles or off-grid structures, they don't consume energy from the on-board fuel or batteries. If placing sensors into airplanes, the additional weight of cables and the risks associated with chemical batteries near fuel tanks make a self-powering sensor node more desirable[32]. Where batteries are an option, these would require routine replacement which could be difficult or expensive to access thus limiting their effective working life[10,20,32]. These primary cell[a] powered nodes are more regular and predictable in their data output than energy harvesting systems[37].

Wired sensors may have some advantages over battery or energy harvesting powered nodes however. The transmitted data is more secure than wireless ones (a physical connection is required to access any data) and reliable (only losing power in the case of damage or power cut, and otherwise could take data near continuously)[42]. Fibre optic sensors share many features with wired sensor systems, except that the wire itself is the sensor[33,41,43]. They are particularly applicable to harsh or toxic environments as the fibre is chemically stable and its

[a] Primary Cell: single-use, non-rechargeable battery.

power inputs are remote[43]. Through multiplexing, a single fibre could have many branches and different kinds of sensor distributed along it, allowing for a much smaller footprint, but returning convoluted data[43]. The cost of this fibre would be considerable, as each one must be bespoke, unlike the off the shelf components used in the above electrical networks[43]. They would also require the entire fibre to be replaced should damage occur to any part of it[41,43].

The small power output from energy harvesting systems only became usable with the improved efficiency of modern electronics[14]. A microprocessor can now be powered with a few hundred μW/MHz in a wireless sensor node[37,44]. The rest of the harvested energy can be used to collect data from a sensor (many of which also consume on the order of μW or less[10,14]), do some post-processing and transmit the data to a central hub. This radio transmission is the most energy intense part of the process, often requiring a few mW; the harvested energy must therefore be stored over a longer timescale to be released in a pulse[37]. Typically the initial connection to the network requires the most energy, as it may require dozens of radio pulses over several seconds before the central hub is free to respond and confirm access[45]. Once connected, a node could be placed into a low-power or sleep mode (where it only needs to maintain the memory state, run the clock, and listen for an activation signal) for much of the time[37]. It would only need to go through this intensive reconnection process if it loses all power[45]; an energy aware circuit in each node could help regulate its power flow to make this less likely, by for instance only activating the transmission or sensing cycle while sufficient stored energy is available to complete it[46,47]. These circuits will consume a small amount of the harvested power, but they could save much more wasted energy over the node's lifetime[46,47]. There is also a move to adapt the computing hardware and software (which are both usually designed with an assumption on a continuous power supply) to be more compatible with an energy harvesting system; e.g. by using ferromagnetic memory (FRAM) instead of conventional non-volatile flash memory[41], and changing the way the program uses the chip's memory to be more robust in the face of interruptions[48,49]. All these improvements would make the systems much more energy efficient, reliable, and enduring. While the power consumption of these electronics is coming down, the capability of harvesting systems to power them has been rising to meet their demands[14].

There are many potential sources of energy to harvest from that are presently untapped, utilising a variety of transduction mechanisms. The choice of which to use will depend on the intended application, its location, and cost. The following section focuses on vibration energy harvesting, while other potential sources are briefly covered in section 2.1.3. Having multiple transduction mechanisms in the same device could increase its reliability through diversification (this works best where volume, weight, or cost are not the most pressing constraints)[11,40].

2.1.2 Vibration Energy Harvesting

Vibration energy harvesting converts ambient kinetic energy into electrical energy[2,5,6,11–13,18,32,50,51]. Vibrations in the built environment are often generated by wind, or other variable loading, and are generally stochastic, low frequency, and of small amplitude[10–12,18]. For the purposes of this work: up to 30 Hz and 300 με respectively. A self-tuneable, broadband, or direct strain harvester may be considered preferable for these situations[5]. Vibrations from machines are usually more predictable, allowing for the possibility to design the harvester to resonate at those particular frequencies[32]. Many non-vibratory forms of kinetic energy, such as fluid flow or rotational motion, could be converted into linear vibrations of the harvesting piezoelectric material (though this would likely be less efficient than a turbine or dynamo, this approach may cause less disruption to these motions), while impacts (including footfalls and pressing a button) may be considered as very low frequency vibrations[38,52]. There are several classes of vibration energy harvester, the specific details of which will depend on the intended source[6,11]. Their primary energy extraction mechanisms shall here be divided into: inertial, and kinematic[6]. The latter may be further split into primarily tensile, compressive, and flexing (any out of plane combination of the two), and unlike inertial systems these do not rely on resonance[11].

Inertial vibration energy harvesters are usually based on a weighted cantilever, such as the example shown in Figure 2-1[5,10,11]. Here, an oscillation of the host surface moves the near end of the cantilever beam, while the free end has a proof mass which resists this motion by inertia[5,10,11]. The bending beam between them results in a driven harmonic oscillator with two main options for extracting energy: electromagnetism and piezoelectricity[5,10,11,23]. If the mass at the free end is a permanent magnet passing by a coil, this will generate electricity[5,10]. Practically

however, with low input frequencies or systems smaller than a few cm^3, the magnetic field tends not to vary fast enough to induce significant current (compounded by the limited space for multiple coil loops)[53]. Much work goes into up-scaling the oscillation frequency from the source or tuning the cantilever's resonant frequency to match likely input vibrations[5,10,11]. Placing piezoelectric material on the flexing cantilever is another common way to generate electricity, exemplified by the PZT in Figure 2-1[5,10–12,54,55]. The flexing of the beam causes the piezoelectric material to stretch and bend, thus generating a voltage between its top and bottom faces[5,10–12,54]; more detail behind this mechanism is discussed in section 2.2.1. A piezoelectric cantilever, while also dependent on the input frequency, produces higher voltages (into the tens of Volts) and lower currents (a few micro-Amps, which could present an issue if the leakage current of the attached circuit were higher) compared to an equivalent electromagnetic system[10,53]. Variations on this basic inertial harvester include beams fixed at both ends with the middle free to oscillate, putting multiple beams around a shuttle, plucking mechanisms (where the beam's oscillation is triggered by an impact on the free end to step up the frequency), or a mass on a spring[7,20,34]; all operate on similar principles.

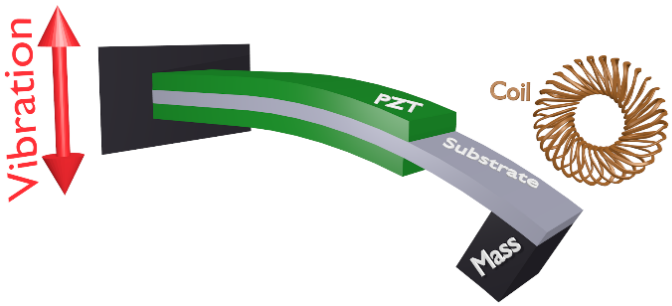

Figure 2-1: Diagrammatic vibration energy harvesting cantilever, shown with both inductive coil (if the mass were a magnet) and piezoelectric (PZT) bimorph layers. Note, these transducers are rarely used together.

Tensile vibration harvesters harness the straining of a volume or surface under an oscillatory load[46,56]. The simplest implementation is to place a piezoelectric material onto, or into, the strained material so that it will be stretched to generate electricity[56,57]. This mechanism can gain a great deal from the use of auxetic components underneath the piezoelectric material[55], as will be discussed in section 2.4 and in the subsequent chapters. The distributed, small-amplitude, in-plane nature of these vibrations makes piezoelectricity the most viable harvesting mechanism available[55].

Compressive vibration energy harvesters work by squeezing the electroactive materials, or pushing a magnet through a coil, to generate electricity[6,11,26,54,58,59]. The force can be applied by a momentary or traveling load (e.g. a car driving over a road or pedestrian walking along a pavement, with pressure pads embedded into the surface[54,58–60], or shoe heel[26]) with a spring force to restore its original shape. This kind of harvester would also work well under vibrating machinery, where it could simultaneously harvest power and damp the vibrations to the surroundings[47,61]. The common cymbal transducer is driven by compression, but uses this motion to stretch the piezoelectric material laterally, extending beyond the equivalent Poisson expansion under direct compression with the same force[26]. An alternative to piezoelectric compression harvesters are electrostatic dielectric elastomer generators (DEGs)[5,10,25,62] These use conductive plates and a polymer dielectric to form a flexible capacitor. When compressed the plates are pushed closer together, decreasing the charge density of the stretched out electrodes, increasing the capacitance; this state is easy to charge up. When the elastomer is allowed to relax, it becomes thicker, and the electrodes contract, increasing their charge density. The plates can then be discharged at a higher voltage. This system requires an initial supply to begin: it is a voltage amplifier, powered by the compression, rather than a strict harvester. Some DEGs can also operate similarly in tension[62]. Several induction-based compression harvesters have reached commercialisation[38,58,59], but either small amplitudes make the power output very low or, in the case of under-pavement harvesting, by allowing a large displacement underfoot the surface may become unstable to walk on (which limits use in public areas, as it's a trip hazard)[58,59,63].

2.1.3 Other Energy Harvesting Mechanisms

There are many other transduction mechanisms used to harvest energy from the environment, some of which shall be briefly discussed here along with their associated challenges, to provide broader context. The sources considered here will be kinetic energy (besides vibrations), ambient electromagnetic waves, and thermal gradients. Different harvesting mechanisms may be combined to diversify the power supply where space permits[11,40]. The choice of which to use is highly dependent on the application (e.g. amount and timescale of energy required) and location (e.g. type and amount of energy available).

While non-oscillating kinetic energy can be converted into a vibration to be harvested, see above, this introduces inefficiencies[5,17,38,64]. It would be simplest to harvest from a rotating system with a dynamo connected to its axel[5,17,38]; due to the magnetic breaking torque it would be counterproductive to harvest from a driven axle (e.g. in a car), but this could be used for regenerative breaking or to power a bicycle's lights[5,17,38]. Linear motion of a shaft, such as pistons or some wave-energy generators, could be harnessed using an electromagnetic coil[5,17,64].

Fluid flows are another source of motion that could be tapped[2,16,19–23,64]. These could be converted to a buffeted oscillating cantilever, but turbines would generally be more effective[19]. In air, such devices work best for high wind speeds, such as around tall buildings, aeroplane wings and cars (as long as the turbulence caused does not diminish the aerodynamics of the vehicle), or confined air in chimneys and exhaust vents[19,32,65,66]. Running water can be used in small or pico-hydro[b] projects[67–69], such as rainwater flowing down a gutter or small waterwheels placed around the base of a bridge to power monitoring of its structural health or of the river's water quality[30, c]. These direct methods may interrupt the original motion too much (e.g. turbines in plumbing systems would lose pressure[16]), so the vibration harvesting methods discussed previously would be preferable (e.g. a flapping cantilever buffeted by the flow[21–23]).

Triboelectric harvesting utilises the friction between differing materials to generate a dipole[2,70]. The triboelectric effect is most commonly experienced as static electricity from clothing of differing fibres rubbing together[70]. The effect is typically considered an impediment, for example when an aircraft passes through icy clouds where the charge build up can interfere with communications, and if not mitigated could spark[70]. The effect could be directed to generate high voltages[2,70]. Currently the power outputs of such devices require idealised conditions to generate more than a few μW, due to difficulties aligning these distributed asynchronous low current (typically nA range) sources into one output[2,70–72]. The ambition in future is to embed these kinds of harvesting devises into clothing and other wearables to power various bio-sensors[70].

---

[b] Defined as any hydroelectric generator yielding $\ll$ 5 kW[67].

[c] Note, this particular node was designed to be powered by solar panels, as their main aim was to optimise the node and the river sensor, rather than its power source[30].

The Sun remains the most potent energy source, at least outdoors in daylight[5,8,17,64]. The typical power density available from micro-solar photovoltaic panels in direct sunlight is 15 mW/cm^3, but indoors this drops to 15-20 μW/cm^3 [5]. Some structural health monitoring systems could run on just sunlight and overnight energy storage, depending on their position[30], but weather dependence could be an issue[11,40]. Other portions of the electromagnetic spectrum could be harvested too. Self-powered crystal radios take their energy from the radio waves absorbed by the antenna[8,73]. Using smaller antennae, shorter wavelengths can be absorbed for more power, up to microwave frequencies[8,73]. Electrical power lines and some machinery leak electromagnetic fields which could be harvested through induction[73].

Heat engines are mechanical means of utilising a thermal gradient, and Stirling engines are of particular interest for energy harvesting[8,27,64,74]. These use a closed-cycle working fluid (typically air, or another gas) between a hot and cold sink to generate motion of the pistons, which could be turned into electricity through many of the means previously discussed. A Stirling engine can be driven from any heat source (including concentrated sunlight[8,27,74]) because it is external to the cycle. They do not require high pressures, making them safer (and potentially quieter) than internal combustion engines[74]; hence they are used in many domestic combined-heat-and-power systems. They have a low power-to-weight ratio however, and like any engine they have many moving parts which become warn over time[27,74]. Small Stirling engines may be driven with thermal differences of between 0.5-100 K[74]. The accelerated rate at which the thermal gradient equalises while extracting power make them useful for waste heat recovery in coolant systems[74].

Thermal gradients may also be harvested directly via the thermoelectric (specifically, Seebeck) or the pyroelectric effects[2,5,8,11,13,32,37]. The Seebeck effect is the direct conversion of a thermal gradient into a voltage, or vice versa, through transfer of charge carriers from the hot side to the cold[5,8,37]. Typically this is realised by joining two dissimilar materials (of widely different Seebeck coefficients); their band energy levels are shifted (as in the joining of n- and p-type semiconductors), creating an electromotive force which shifts when one side is heated[5,8,37]. Thermoelectric generators using this effect are small, solid-state heat engines, though they are inefficient and expensive due to the rare minerals

often required[32]. They could be used to recover waste heat[13], and have been used in many deep space missions (using radioactive decay as the heat source)[2]. This effect is used in thermocouples and thermopiles to measure temperature[2].

Pyroelectricity generates a voltage during heating or cooling (whereas thermoelectricity works while the thermal gradient remains)[2,11,13,32]. This is a property of polar materials[d] which pushes unbound charges apart while changing temperature, amplifying (cooling) or reversing (heating) its polarisation[11]. Some of these materials can be poled by external electric fields, indicating they are also ferroelectric (see subsection 2.2.2)[2,11]. Small temperature changes (if applied quickly) can develop significant voltages, making pyroelectric materials suitable for passive thermal sensors[2,11]. An effective pyroelectric generator would require a rapidly fluctuating heat source (thermal mass usually limits this to <1 Hz[11]) and expensive materials to make, though there may be more efficient materials or MEMS structures to improve this in future[2,11,32].

2.2 Piezoelectric Materials

2.2.1 Piezoelectricity

Piezoelectricity is a property of certain materials where their electrical polarisation responds to applied mechanical stress; these materials also exhibit the converse effect, where an applied voltage causes mechanical stress[6,75–77]. Piezoelectricity is most commonly found in crystalline (quartz, Rochelle salt, etc.) or ceramic materials (PZT, ZnO, $BaTiO_3$, $KNbO_3$, etc.), but has also been observed in some biological matter (silk, bone, DNA, etc.) and polymers (PVDF, once poled)[6,75–77]. The effect is usually negligibly small, though in some specially synthesised crystals and ceramics it can produce a significant voltage (tens of Volts from even modest excitations; enough to create a spark), or conversely a small strain[6,75–77].

Figure 2-2 shows linear interaction effects between mechanical stress, *T*, and strain, *S*, and the electric, *E*, and displacement, *D*, fields[75], with arrows pointing in their customary cause to effect directions (though converse effects may also

[d] All pyroelectric materials are also piezoelectric, but crystal classes with central symmetry cannot be pyroelectric. Similarly, ferroelectricity is a subset of both pyro- and piezoelectricity.

occur). The term ‘piezoelectricity’ collectively describes the four emboldened interactions, in either direction. The direct effect starts from one of the mechanical nodes and moves to either electrical node, while the converse effect goes vice versa. Non-linear effects are omitted for clarity.

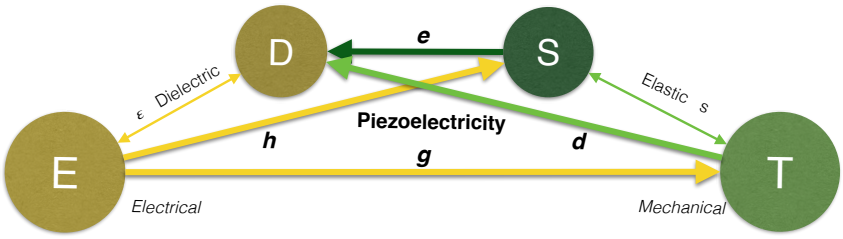

Figure 2-2: Linear interaction processes between electrical and mechanical effects; piezoelectric connections emboldened.

A non-linear effect that is sometimes confused with piezoelectricity is electrostriction[6,75,77]. This is where an applied electric field causes mechanical strain, but unlike piezoelectricity the direction of this strain remains the same if the field is reversed; this field will always attempt to pull the material apart. Electrostriction occurs in all non-monatomic dielectrics to a small degree, though the effect is negligibly small in most cases (especially compared to the piezoelectric effect in the materials discussed in section 2.2.2), and the magnitude of strain it induces is proportional to the square of the polarization between the constituents[6,75,77]. By contrast, piezoelectricity (both direct and converse) will flip direction under a reversed input: ideally, if a tensile force applied to a piezoelectric material produces a negative voltage, – *x* V, then the same force in compression results in + *x* V [e]; likewise reversing the polarity of an applied electric field would flip the direction of the piezoelectric strain[6,75,77, e].

Piezoelectric materials are mathematically defined using material constants[6,75–77], allowing them to be simulated using finite element modelling or, for simple cases, be calculated analytically. The mechanical and electrical coupling is characterised by the piezoelectric constants[6,75–77]. They come in four interrelated sets: *d*, *e*, *g*, and *h*, each indicated on the emboldened arrows in Figure 2-2 and defined by equations 2–1-4[75–77]; which set to use is a matter of convenience. The most commonly used are the piezoelectric charge constant, *d*,

[e] In practice, the same strain magnitude applied in opposed directions will not produce the same absolute voltage, due to electrostrictive and thermal effects which occur alongside the piezoelectric effect. Likewise for the converse effect[6,76]. These losses are considered negligible.

or the piezoelectric voltage constant, *g* (which is more often used for sensors)[6,61,75–77]. The *e* and *h* constants are rarely used, as they are effectively the inverses of *g* and *d*, respectively. Modelling also requires the elastic compliance of the material, s^E (defining its stiffness), and its relative permittivity, ε. Piezoelectric materials are anisotropic so all these properties vary in different directions. Each constant here takes the form of a matrix where every element indicates the strength of coupling between the axis *i* (electrical polarisation direction) and *j* (mechanical action direction)[6,61,75]; Figure 2-3 assigns the axes values. Piezoelectric polarization is generally considered as the *3*, or *z*, direction. By convention, shear motion around the *x* & *y* axes are referred to as *15* & *24* respectively[6,61,75]. Equations 2–5 to *2–8* are widely used to model piezoelectric effects; the general matrix form is given first, while their expanded forms have material parameters for tetragonal crystals (such as PZT, see section 2.2.2)[6,61,75]. Most materials have some parameters duplicated in another axis: e.g. s_{12}^E & s_{21}^E are mirrored in the diagonal of s^E, indicating the same in-plane structure.

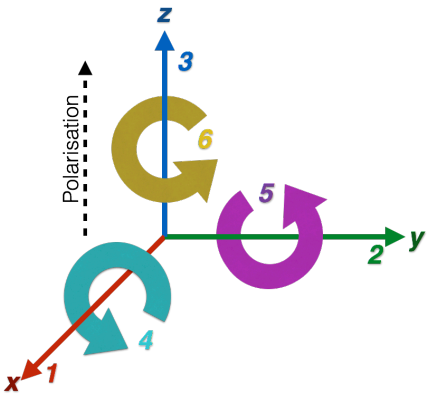

$$d_{ij} = \left(\frac{\partial D_i}{\partial T_j}\right)^E = \left(\frac{\partial S_j}{\partial E_i}\right)^T \quad \text{Eq.2–1}$$

$$e_{ij} = \left(\frac{\partial D_i}{\partial S_j}\right)^E = -\left(\frac{\partial T_j}{\partial E_i}\right)^S \quad \text{Eq.2–2}$$

$$g_{ij} = -\left(\frac{\partial E}{\partial T_j}\right)^D = \left(\frac{\partial S_j}{\partial D_i}\right)^T \quad \text{Eq.2–3}$$

$$h_{ij} = -\left(\frac{\partial E_i}{\partial S_j}\right)^D = -\left(\frac{\partial T_j}{\partial D_i}\right)^S \quad \text{Eq.2–4}$$

Figure 2-3: Crystal orientation directions.

$$\{S\} = [s^E]\{T\} + [d]'\{E\} \quad \text{Eq.2–5}$$

$$\begin{bmatrix} S_1 \\ S_2 \\ S_3 \\ S_4 \\ S_5 \\ S_6 \end{bmatrix} = \begin{bmatrix} s_{11}^E & s_{12}^E & s_{13}^E & 0 & 0 & 0 \\ s_{21}^E & s_{22}^E & s_{23}^E & 0 & 0 & 0 \\ s_{31}^E & s_{32}^E & s_{33}^E & 0 & 0 & 0 \\ 0 & 0 & 0 & s_{44}^E & 0 & 0 \\ 0 & 0 & 0 & 0 & s_{55}^E & 0 \\ 0 & 0 & 0 & 0 & 0 & 2(s_{11}^E - s_{12}^E) \end{bmatrix} \begin{bmatrix} T_1 \\ T_2 \\ T_3 \\ T_4 \\ T_5 \\ T_6 \end{bmatrix} + \begin{bmatrix} 0 & 0 & d_{31} \\ 0 & 0 & d_{32} \\ 0 & 0 & d_{33} \\ 0 & d_{24} & 0 \\ d_{15} & 0 & 0 \\ 0 & 0 & 0 \end{bmatrix} \begin{bmatrix} E_1 \\ E_2 \\ E_3 \end{bmatrix} \quad \text{Eq.2–6}$$

$$\{D\} = [d]\{T\} + [\varepsilon]\{E\} \quad \text{Eq.2–7}$$

$$\begin{bmatrix} D_1 \\ D_2 \\ D_3 \end{bmatrix} = \begin{bmatrix} 0 & 0 & 0 & 0 & d_{15} & 0 \\ 0 & 0 & 0 & d_{24} & 0 & 0 \\ d_{31} & d_{32} & d_{33} & 0 & 0 & 0 \end{bmatrix} \begin{bmatrix} T_1 \\ T_2 \\ T_3 \\ T_4 \\ T_5 \\ T_6 \end{bmatrix} + \begin{bmatrix} \varepsilon_{11} & 0 & 0 \\ 0 & \varepsilon_{22} & 0 \\ 0 & 0 & \varepsilon_{33} \end{bmatrix} \begin{bmatrix} E_1 \\ E_2 \\ E_3 \end{bmatrix} \quad \text{Eq.2–8}$$

2.2.2 Materials for Vibration Energy Harvesting

Many piezoelectric materials are used in energy harvesting research[6,10,11,52,57,76–79], but by far the most discussed material is PZT (Lead Zirconate Titanate: $Pb(Zr,Ti)O_3$), due primarily to its strong piezoelectric coupling and wide availability[6,11,14,52,76,78]. Other commonly used materials include barium titanate ($BaTiO_3$: BT)[77], potassium sodium niobate ($K_{0.5}Na_{0.5}NbO_3$: KNN)[80] and its related substances[6,11,81,82], zinc oxide (ZnO)[6,83–85], Polyvinylidene (di)fluoride (PVDF)[6,78,79,86,87], or active fibre composites like MFC (Macro Fibre Composite, with fibres cut from bulk PZT 5A1)[56,88–90].

PZT, BT and KNN are perovskite ceramics, with an atomic cell structure shown in Figure 2-4[6,77,91,]. Thick layers (≫100 μm) are manufactured by sintering their constituent powders, while thin (<1 μm) and thick (>1 μm) films are typically made by vapour deposition[2]. They are then ferroelectrically[f] poled by placing them in a strong electric field once heated to around their Currie point (where thermal activity breaks up all domains); the field is then maintained during cooling[76]. This gives a preferential polarization axis in response to applied stress, either *31*- or *33*-mode (indicated in Figure 2-5), throughout the crystal[6,76], which increases their accessible power output by reducing opposing domains[6,11,77]. Note that any of these ceramics that are *31*-poled are equally *32*-poled because of the *x*-*y* plane's identical structure in either axis; see section 2.4.1. In energy harvesting, it is beneficial for the polarisation to go through the thinnest dimension, to reduce electrical losses within the material[5,10]. In a typical cantilever setup, including this work, a *31*-mode crystal is preferred, despite its slightly weaker coupling than the material's *33*-mode[2]. Using 33-poled materials on cantilever-based harvesters requires interdigitated electrodes; making production more difficult[10]. A compressive vibration harvester could easily be stressed in the same axis as its polarization and would typically use *33*-poled material[2,5,10]. PZT has 'hard' (e.g. PZT-5H) and 'soft' (e.g. PZT-4) varieties determined by its dopants; named for their domain motilities. Hard PZT retains its properties under higher stress or fields, and is thus preferred for energy harvesting[2,92]. All PZT remains brittle however, with a yield strength of ~35-40 MPa (depending on variety)[92,93].

[f] Ferroelectricity is named by analogy to ferromagnetism (though iron isn't needed) as the electric domains align to the applied field; this polarisation persists once the field is removed.

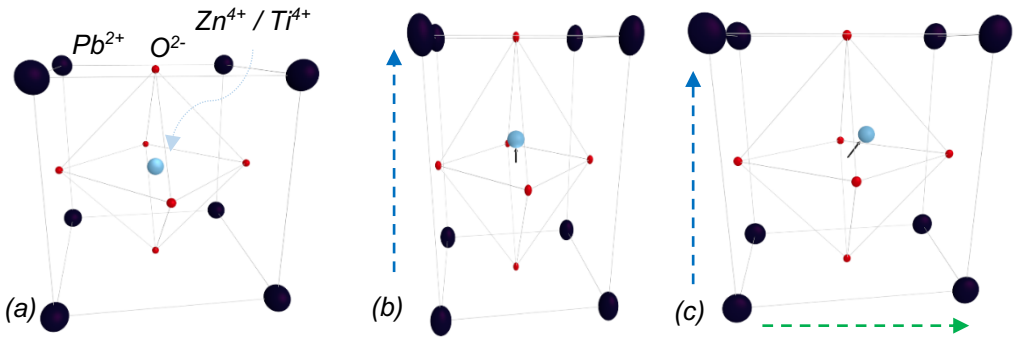

Figure 2-4: A 33-mode perovskite crystal unit cell, with PZT constituents indicated, under (a) no deformation (b) vertical strain, shown with the dashed arrow, and (c) strain in both the z & y directions. Polarization shown by the black arrows in (b) & (c).

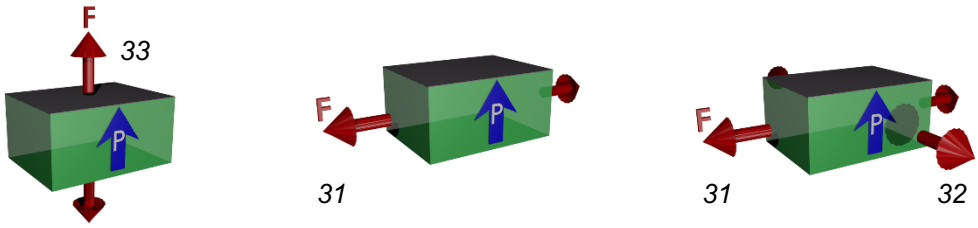

Figure 2-5: Resultant poling direction, P, from applied tension, F, for 33, 31, and 31 & 32 modes respectively.

Non-ferroelectric ceramics like ZnO, gallium nitride (GaN) or aluminium nitride (AlN) have their polarization axis defined by their intrinsic atomic structure[6,83–85]. They tend to have weaker piezoelectric characteristics than poled perovskite materials, making them less attractive for energy harvesting, but ZnO has been used in nanofiber triboelectric harvesters, mentioned in section 2.1.3[2,84]. They may also find use where lead-free materials are required[6,80,81].

Other lead-free alternatives to PZT are being proposed, such as KNN, LN (lithium niobate, aka $LiNbO_3$) and other alkali-niobate ceramics[6,11,14,80,82,94,95]. Researchers are still predominantly at the stage of determining material properties and optimal means of production, rather than specific applications, though they appear promising[80,82]. They can have high piezoelectric coefficients, and could withstand similar or greater strain than PZT in certain crystal orientations[82]; however, they are currently more difficult to make[80].

PVDF (polyvinylidene difluoride) is a piezoelectric polymer[6,52,78,79,86,87]. Its long chain structure, shown in Figure 2-6, can be ferroelectrically poled; putting all the fluorine and hydrogen groups on opposite sides[6]. The charge distribution between these sides changes when the molecule is stretched or distorted, giving rise to its piezoelectric properties[6]. Compared to ceramic materials, these

properties are very weak; severely limiting the power available from any harvester utilising PVDF[6]. It is however highly flexible and can endure much larger strains (up to ~2%[6]) than the brittle crystal or ceramic materials, making it suitable for embedding within fabrics for wearable energy harvesting[6,52].

Piezoelectric fibre composites, PFCs, and active fibre composites, AFCs, have been developed more recently, mainly for actuation and ultrasonic applications[6,76,90]. NASA developed macro fibre composite, MFC, using a layer of parallel rectangular fibres of PZT 5A1 with interdigitated electrodes embedded in epoxy[56,61,76,88,96]; shown in Figure 2-7. This material is flexible in both directions, yet retains much of the piezoelectric response of its ceramic base[5,6,56,76]. MFC has energy harvesting applications in the aerospace sector[5,9,18,44,56,61,76,88].

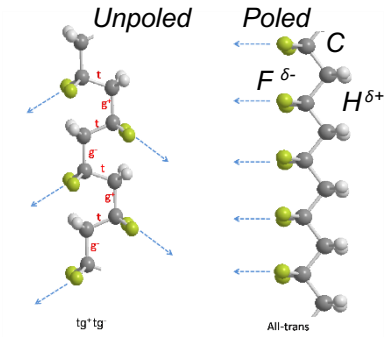

Figure 2-6: PVDF atomic structure: poled (right) & unpoled[g].

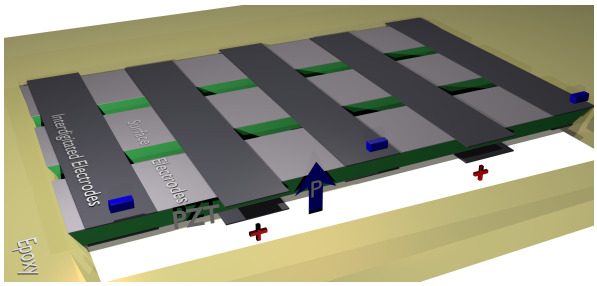

Figure 2-7: Diagrammatic 31-poled MFC cutaway.

2.2.3 Other Applications of Piezoelectricity

Piezoelectric materials have many applications besides energy harvesting[75,77,97]. Piezoelectric materials produce high voltages compared to the applied strain, and low currents[10,75]; this makes them useful for sensors or generating sparks (as used in some lighters)[75]. From the direct piezoelectric effect, the strain on the crystal can be measured by its voltage; attaching it to a surface forms a strain gauge[97,98]. This could be a self-powered device in an energy harvesting system[97,98]. Piezoelectric pickups use a similar mechanism to convert the vibrations of an acoustic instrument into an output signal[77]; these don't require steel strings[h], can makes the output sound sharper than using an external microphone, and reject the electromagnetic noise. Piezoelectric crystals

[g] Public domain image from: commons.wikimedia.org/wiki/File:Ferroelectric-wiki-w3.png

[h] Electric stringed instruments generally use a permanent magnet wrapped in fine copper wire. The vibrating steel string cuts through the magnetic field, inducing a current in the coil.

were used to convert the needle motion along a vinyl record track into the electrical signal for the speakers (magnetic induction is now more typical)[77].

The converse effect can be used as an alternative to many electromagnetic devices[24,61,76,77]. The high electric fields required to cause tiny changes in its dimensions make micro-actuators more precise than electromagnetic equivalents[76]; many scientific grade linear stages use multilayer piezo-ceramics for translations on the nm-μm scale[76] for aligning micro-mirrors or acousto-optic modulators[76]. Rotational stepper motors can use these linear extenders to push the rotor around[76]. The limitation with both of these is that their motion is slow and has a tiny range[76,99,100].

Quartz oscillators have long been used in many small clocks to keep regular time[75]. Piezo-ceramic disks are often used for compact, cheap, low-fidelity speakers or buzzers[76,77]. They are also used in the production and detection of ultrasonic frequencies (usually a PFC), which electromagnetic systems struggle with[75–77,81]. These ultrasonic devices may be used to: conduct medical scans, break up kidney stones, disintegrate material within a mixture, or in sonar[75–78].

2.3 Auxetic Materials

2.3.1 Overview

Auxetic materials have a negative Poisson's ratio, unlike conventional materials[101–105]. This means that they expand laterally when stretched, or vice versa compress laterally when squeezed. The word 'auxetic' was coined by Evans in 1991[101] as a collective term for such materials. Poisson's ratio, v, for isotropic materials is the perpendicular change in dimensions over the length change in the applied force direction, equivalent to transverse strain over the axial strain; with sign conventions ensuring most materials are within the $0 \leq v < 0.5$ range[103,104]. A negative value can be achieved by the material having a re-entrant or self-infolding internal structure at some scale[105,106]. Alternatively, a negative v can come from internal holes between hinged units[105,107,108].

Much of the early research discussed collapsed foam-based materials, utilised for enhanced sound absorption or more comfortable cushioning[102,109,110], but using an appropriate geometry can allow most standard materials to behave

in an auxetic manner; at least when considered in bulk (the material retains its usual Poisson's ratio at a localised scale)[105–108]. For example, the re-entrant honeycomb, shown in Figure 2-8, has a regular array of bow-tie holes cut out from a flat sheet, resulting in a pliable framework[105,111]. When stretched, this structure deforms so that the holes expand (tending toward rectangles in this case) and push the sides out laterally[105,111]. There are many other geometries which can achieve this effect[103,105,112]. Most of these structures utilise solid units (commonly squares or triangles), connected at their corners which rotate outwards when stretched[103–105,107,108], or re-entrant networks of connected beams[105,111–115]. Figure 2-9 shows a selection of such designs, and that many apparently disparate mechanisms are related[105]. Similar principles hold in three dimensions, for example Figure 2-10[103–105,116].

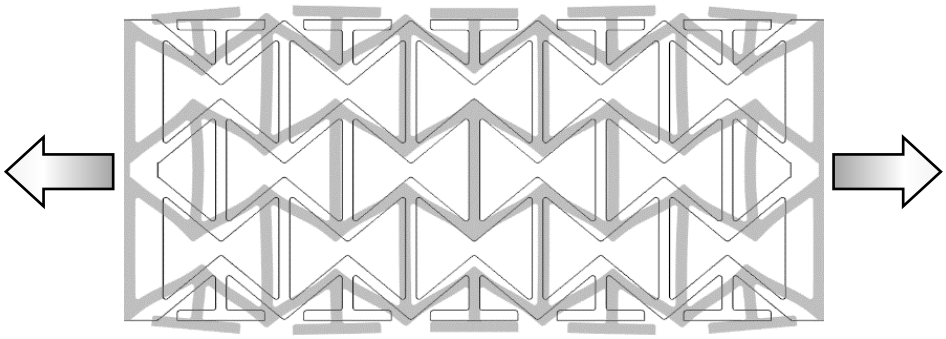

Figure 2-8: Example auxetic design: re-entrant honeycomb array, arrows show axial stretch directions, deformed result shown in grey; original shape in black outline.

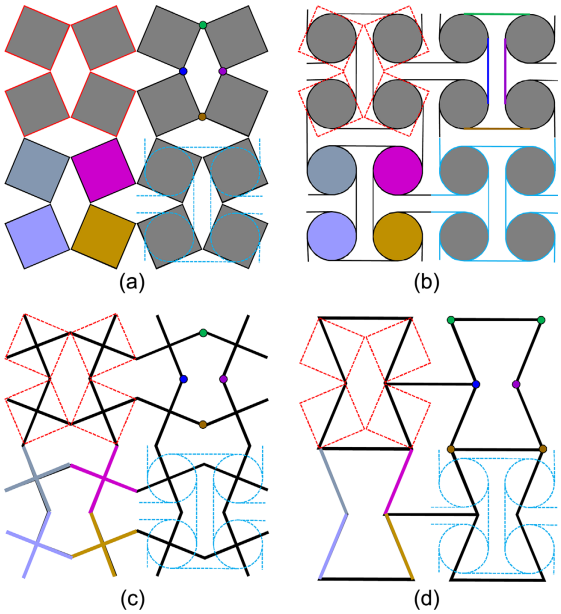

Figure 2-9: Four 2D auxetic designs, showing analougus mechanisms between them; taken from [105]. Models: (a) Rotating Squares; (b) Anti-Tetrachiral; (c) Missing Rib and (d) Re-Entrant Honeycomb.

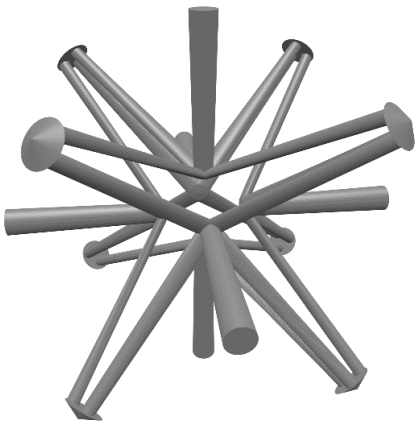

Figure 2-10: A single re-entrant 3D auxetic unit.

As a result of the negative Poisson's ratio, auxetics exhibit many other characteristics which could make them more hardwearing and adaptable materials[102,103,105]. These range from increased fracture toughness, a greater shear modulus, more resistance to indentation, and a greater (and tuneable) acoustic response[103,104,111,117]. A flat sheet of auxetic material can easily form into a dome (synclastic curvature), while regular sheets only tolerate saddle-shaped (anticlastic) curvature[103,104]. Auxetics' main limitation is concentrating internal stress into narrow bending or flexing regions, where they could easily crack or succumb to fatigue (a large network could be more resilient overall)[110]. These characteristics could classify auxetics as mechanical metamaterials[112,118–121].

2.3.2 Other Auxetic Applications

Many applications for auxetic materials are still at a research phase, though some are commercially available; e.g. some Nike trainers have auxetic soles (with a rotating triangle design), the supposed benefit being they expand in both in-plane directions, akin to the splaying of bare feet[122]. Conventional materials buckle away from an impact, but auxetic materials could expand into the force, see Figure 2-11[102,104]. Blast-proof fabrics can be made from auxetic fibres (which can be made by winding a narrow stiff fibre around a soft thick one, see Figure 2-12)[123–126]. Their synclastic curvature could be used for flexible bandages, particularly those going over joints[103,123]. There have been auxetic stent[i] designs[102]; which allows them to bend and slide through the vein until they reach the correct location, then expand outwards to support the walls. The heightened acoustic response of many auxetic materials could make more efficient noise absorption[103,127]. An auxetic filtering membrane could be expanded and contracted to select the particle size that is allowed through[103,104,123].

[i] Stent: a hollow tube placed inside a blood vessel, or similar, to hold it open temporarily.

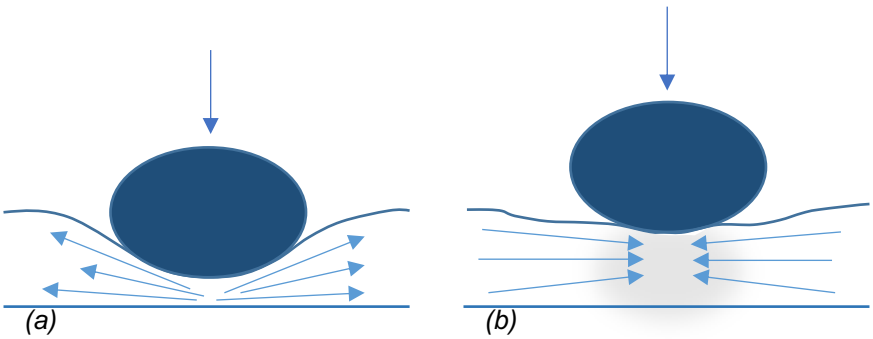

Figure 2-11: Effect of an impact on (a) conventional and (b) auxetic materials; its momentarily increased density under the projectile is indicated by the shaded area.

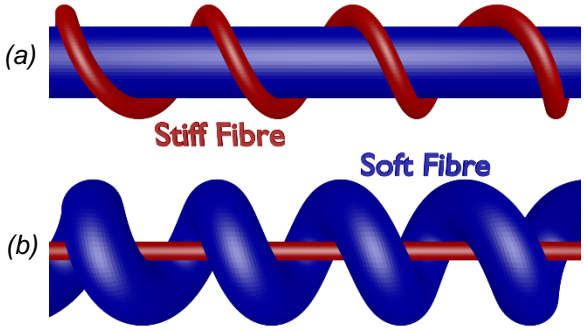

Figure 2-12: Example of an auxetic fibre in (a) relaxed state and (b) under tension.

2.4 Auxetic Piezoelectric Energy Harvesting

2.4.1 Theoretical Underpinning of Gain

This work focuses on combining auxetic metamaterials with piezoelectric materials for improved vibration energy harvesting[1]. This takes advantage of how any *31*-poled piezoelectric layer is also *32*-poled[55]; as discussed in section 2.2.2. By Poisson contraction, the *2*-axis will contract from tension applied in the *1*-axis, and vice versa, thus the average stresses in the *1* and *2* axes would typically be of opposing signs (the latter's absolute value being smaller)[55]; when this lateral *32*-axis is considered it is often only as a loss. Equation 2–9 gives the power output from the piezoelectric layer at its optimal resistive load, and shows how these opposing stresses, T_{11} *and* T_{22}, reduce the harvested power[55].

$$P_{opt} = \frac{2\pi f A_p t_p d_{31}^2}{\varepsilon_0 \varepsilon_{33}} (\overline{T_{11}} + \overline{T_{22}})^2 \qquad \text{Eq.2–9}$$

Here *f* is the oscillating excitation's frequency (far below material resonance), A_p and t_p are the area and thickness of the piezoelectric material, d_{31} is the piezoelectric coupling strength between the in-plane motions and the *z*-axis

polarisation (and here assumes $d_{32} = d_{31}$, as is typically the case in bulk piezoelectric ceramics[j]), ε_{33} is the relative permittivity through the thickness, and $\overline{T_{11}}$ & $\overline{T_{22}}$ are the average stresses of the piezoelectric layer in the *x* & *y* directions respectively[55]. If $\overline{T_{22}}$ were made to be the same sign as $\overline{T_{11}}$ (i.e. both axes in tension, or compression, simultaneously), then these terms would add and the power output would greatly increase. Auxetic designs, through their lateral expansion under tension, could facilitate this bidirectional excitation, and turn the typical *32*-axis loss into a gain[55].

2.4.2 Review of the State-of-the-Art

The use of auxetic materials in energy harvesting could lead to dramatic improvements in power output over currently available harvesters, and become important in opening up untapped sources that would otherwise be insufficient to power a vital sensor. This research is still at an early stage, based primarily on simulations rather than experiments. Li, Kuang & Zhu[55] have modelled a bimorph energy harvester with an auxetic substrate (shown in Figure 2-13) which they expect could generate 2.76 times the power of an equivalent plain, solid substrate. Their results show dramatic increases of stress in the PVDF piezoelectric layers over the slits in the auxetic substrate, compared to a plain substrate. The regions bonded over the solid squares of the substrate show a minimal stress increase; indicating that there is still much room for improvement on this principle.

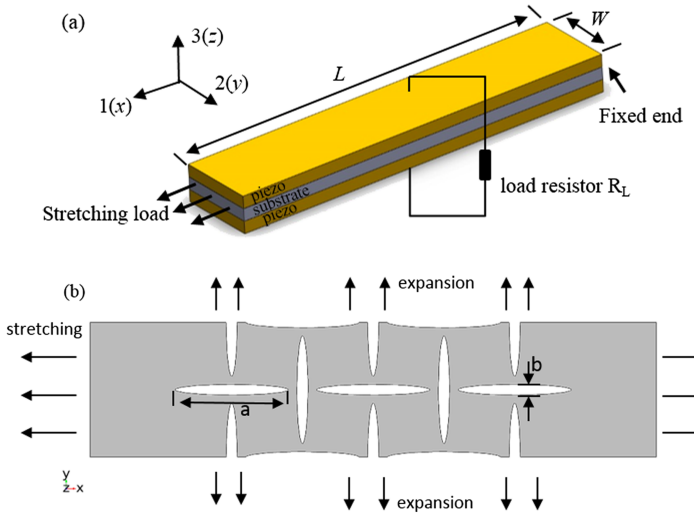

Figure 2-13: (a) Structure of bimorph and (b) substrate modelled by Li, Kuang & Zhu[55].

[j] If d_{31} were not this common factor, the bracket in equation 2–9 would be $(d_{31}\overline{T_{11}} + d_{32}\overline{T_{22}})$.

Fang et al.[79] modelled and tested this type of auxetic design in a flag harvester, cutting slits into the PVDF itself, resulting in improved energy conversion efficiency: from around 0.4% at best, up to 0.6-0.7%. They compared an uncut sheet with: unidirectional cuts (perpendicular to the applied tension), a square cut (similar to Figure 2-13(b)), and a fractal cut (some slits from the square cut are double length, intersecting crossing slits). They found all these cuts were able to increase the energy conversion efficiency during flag flutter testing in a wind tunnel over different windspeed bands; harvesting energy from lower windspeeds than the uncut sheet (absolute power was lower due to reduced wind energy input). They conclude architected cuts could be a simple way to tune the resonant response of PVDF without diminishing its piezoelectric performance.

Recalling Li, Kuang & Zhu's work[55], a means of further increasing the power output might be to make the holes a greater fraction of the substrate surface area. This has been modelled by Chandrasekharan & Thompson[128] for a cantilever bimorph harvester, though their aim was to increase the power-to-weight ratio (which they show improvements of up to 25%), and provide a new means of tuning its resonant frequency. They modelled a regular honeycomb framework as their substrate, shown in Figure 2-14, where the walls of the honeycomb were much thinner than the substrate thickness (152 to 760 μm respectively). They mention the possibility of using an auxetic honeycomb, based on the work of their student Adeshara[129], and shown in Figure 2-15, but dismiss it as slightly less effective than the regular honeycomb. This neglected design used the same thin cell walls, which would struggle to impose any of their lateral strain upon the stiff PZT layers. This lack of authority, combined with the slightly greater mass required for the auxetic honeycomb, results in a lower power-to-weight ratio (though still an improvement over the plain). These works[128,129] show that for auxetic components to be a benefit to energy harvesting there must be a balance between making the structure flexible, and the authority it needs to stretch the piezoelectric material.

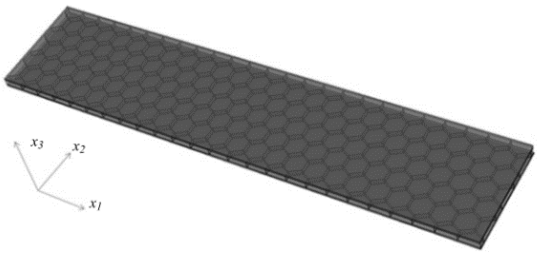

Figure 2-14: Honeycomb bimorph from Chandrasekharan & Thompson[128].

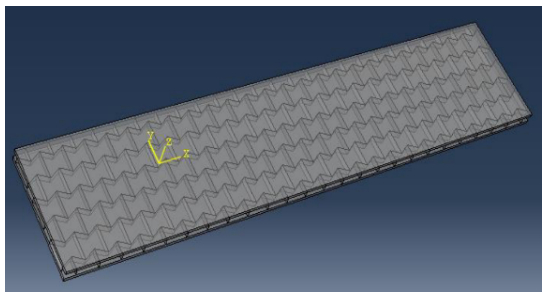

Figure 2-15: Re-entrant honeycomb bimorph modelled by Adeshara[129].

Umino et al.[118] modelled and tested a bimorph of a design similar to Adeshara's in Figure 2-15, but at a smaller scale (20×10×0.28 mm). They found that this auxetic design increased the power output by 1.6 times (47.4 to 29.8 μW), and reduced the resonant frequency (fundamental: 21.1 from 24 Hz) compared to an equivalent plain. This gain may be helped by their cell walls being only half the thickness of the substrate (100 to 200 μm) and therefore the substrate had more authority over its piezoelectric layer (PVDF), or it could be the substrate's greater flexibility. This shows that auxetic designs can be used to tune a resonant response in practice, as well as in simulations. The raw output was still low due to the small size and use of PVDF.

Another option is to have the piezoelectric layer's shape match the auxetic framework. De Bellis & Bacigalupo[98] designed and analysed an anti-tetrachiral auxetic lattice of PZT-5A layer sandwiched by protective polymer, shown in Figure 2-16(b). This profile could make a strain gauge >6 times as sensitive. The smaller amount of piezoelectric material due to the design's large empty spaces would limit the available power output, meaning to be fully self-powered this design may have to cover a much larger area than a solid plain equivalent; though for structural health monitoring of buildings and infrastructure this may not be a problem. Such a complex design would also be very difficult to manufacture from a brittle piezoceramic material.

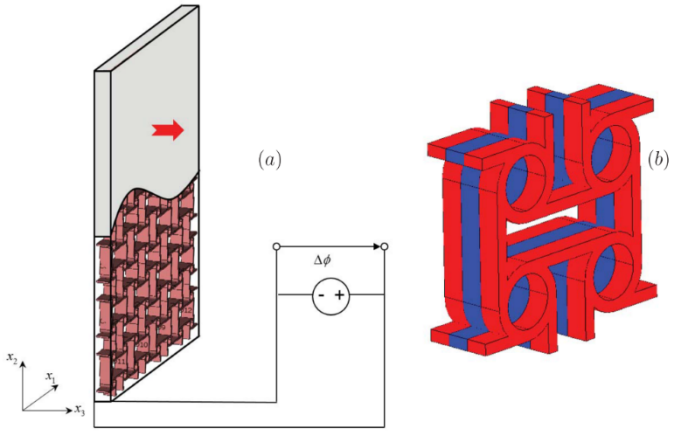

Figure 2-16: (a) Anti-tetrachiral strain gauge and (b) unit cell, showing (blue) PZT layer in the centre, sandwiched in (red) polymer, modelled by De Bellis & Bacigalupo[98]

Some work has been done in energy harvesting with auxetic components, without using piezoelectric materials. The US navy[25] have a patent using auxetic electrodes in an electrostatic dielectric elastomer generator (DEG) to fit in a boot's heel. The auxetic plates amplify the DEG's charge concentration effect by reducing their volume under compression. Another wearable DEG with an auxetic framework has been demonstrated by Bassani, Jean-mistral & Ruffald[62] in a backpack strap. This uses the inertial force between the backpack and the walking wearer to stretch the DEG (in both plane directions for the auxetic configuration) to harvest the energy from their walking. Their re-entrant 'bowtie' configuration gained 53% of its input energy, verses 32% from the non-auxetic baseline. These DEGs could be integrated into the straps of rucksacks, handbags, and even clothing. The initial voltage source is required however.

There is more available literature on the subject of piezoelectrically driven auxetic actuators[6,81,100,102,103], some of which could operate in reverse for harvesting. There are cases where actuation may be required in one phase, then ambient vibrations could be harvested during another phase; such as deploying a satellite's solar panels, then harvesting energy from those panel's vibrations for the rest of its working life[130]. Fey et al.[100] made a re-entrant honeycomb structure from bulk PZT; increasing the range of movement for actuation. While it could be used in reverse for harvesting, it would also be highly susceptible to damage under any excessive load it was exposed to.

Alternately, piezoelectric materials may be integrated into a structure. These could be used for actuating flexible fibre composites (which can be auxetic)[6,81,131]. Run in reverse, some of these composites could form integrated self-powered

strain gauges or energy recovery mechanisms. Topolov & Bowen[81] discussed auxetic polyethylene composites incorporating piezoelectric blocks, serving as more flexible replacements for bulk ceramic piezoelectric materials; this potential new generation of PFCs allow higher strain (and lead-free) applications in both actuation and harvesting. These kinds of piezocomposite devices are already used in some medical ultrasonic imaging sensors and sonar hydrophones, where their auxetic polymer matrix has been shown to improve the mechanical coupling to the piezoelectric components[81,102,103]. If used in reverse for harvesting, the polymer might absorb a significant fraction of the input energy, but these mechanical losses could be offset by being able to place the piezoelectric components under pressure from all sides and harvest from higher strains than a bulk ceramic could endure, resulting in a greater power output overall.

From this literature, the combination of piezoelectric and auxetic materials has been found to increase the power output for a range of mechanically driven harvesters; much of these efforts thus far have been purely theoretical however. Where empirical efforts have been made, the increased power has been a modest 1.6 times[62,118], while simulations find up to 2.76 times possible[55,79,128,129]. The aim of the following research is to demonstrate larger gains by focusing on optimising the substrate's auxetic design for power output; rather than for minimising weight or lowering resonant frequency, as much of the above work has. Such designs would make low strain ($\ll$ 300 με) environments more suitable for energy harvesting; generating enough in situ for many useful structural health monitoring applications that would otherwise require batteries (and the regular replacements that entails). The small oscillations caused on a building's superstructure from wind loading, pedestrians walking over a building's joists, or vehicles passing over the span of a bridge, could all become sufficient energy sources for remote sensor nodes[132]. As auxetic materials concentrate ambient stress, brittle piezoelectric materials could be easily damaged in turbulent or already high strain environments (where currently available harvesters could already be sufficient energy sources)[110].

The following chapters in this thesis will demonstrate that by introducing auxetic metamaterials to vibration energy harvesters their power output, from the same mechanical input, is greatly increased.

3 Proof of Concept Study of Auxetic Power Amplification

In the previous section, some efforts from the literature in utilising auxetic designs for energy harvesting were discussed, but these have been of limited success thus far. For this initial proof of concept study, a strain energy harvester was developed, incorporating an auxetic re-entrant hexagon structure in its substrate to concentrate applied strain into the piezoelectric layer. This was optimised using Finite Element Modelling (FEM) and tested under laboratory conditions with comparison to a baseline plain design. This design process was therefore validated for further developments. The work in this chapter has been previously published as '*Auxetic structure for increased power output of strain vibration energy harvester*' by Ferguson, et al.[1].

This chapter will describe the process of modelling and optimising the auxetic substrate design in section 3.1. Section 3.2 will discuss sample manufacturing and testing, and how the data was subsequently analysed. The results from this are then presented and discussed in section 3.2.4. Finally, section 3.3 draws out the conclusions.

3.1 Finite Element Modelling Design

3.1.1 Modelling Method

Finite element modelling was used to investigate the benefits of the auxetic region on the harvested power, and to optimise its design. This model, developed in COMSOL Multiphysics® 5.3, is schematically illustrated in Figure 3-1 with its dimensions listed in Table 3-1. The auxetic re-entrant hexagon geometry was selected, based on preliminary work comparing many auxetic geometries; which are developed in chapter 6.

The model consists of a mild steel substrate under a piezoelectric layer (PZT, specifically PIC151 from Physik Instrumente GmbH & Co.[133]). This off-the-shelf standard size piece (20×20×0.18 mm) guides the overall size of the substrate: 80×20×1.15 mm; with the auxetic region in the middle, under the piezoelectric

material. This substrate is as wide as the PZT, with enough length to be clamped into the testing apparatus, in a widely available thickness. An epoxy layer, ~8 μm thick, lied between these (its profile being a projection of the substrate's, as seen in Figure 3-1(a)); plausibly small variations in this thickness were subsequently found to have a negligible effect on the power output, see appendix A.I.ii. The properties of all these materials used in the model are listed in Table 3-2.

A parametric analysis was used to determine the optimal dimensions for the re-entrant hexagon. 'Optimal' is here defined as the highest power output obtainable within the peak stress limits of both steel and PZT at the maximum intended mechanical input (250 με); this was calculated with von Mises stress as it is independent of direction. There are four parameters defining the shape of the auxetic region: beam width, t_b, deformation angle, α, crossbeam length, *cb*, and filleting radius, *fr*; these are shown in Figure 3-1(b), with their parametric ranges and final values listed in Table 3-1. These were swept individually within physically plausible ranges to isolate their effects on the power and stress levels. The best values were iteratively carried through to the sweep of the next parameter to find the dimensions. This process was repeated, carrying the parameters through in different orders from different starting points to establish a consistent best case design. A case study is discussed in section 3.1.2.

The substrate has two clamped portions, each L_{clp} long, at either end. The top and bottom surfaces of one clamp were fixed, while those at the other end were subjected to a harmonic displacement of 10 μm in the positive *x*-direction to supply a peak-to-peak strain of 250 με on the free substrate. A frequency domain analysis simulates just the peak displacement and calculates the full cycle's output from half this peak power. This value is almost identical to that from a time domain study, but much more computationally efficient; see also appendix A.I.i.

A load resistor was connected between the bottom (ground) and top (terminal) faces of the piezoelectric layer. Its resistance matched the internal impedance of the PZT, to characterise its maximum power transfer at the excitation frequency, *f*, using equation 3–1. Other variables defined in Table 3-1 and Table 3-2.

$$R_{opt} = \frac{t_p}{2\pi f \varepsilon_0 \varepsilon_{33} L_p W_p} \qquad \text{Eq.3–1}$$

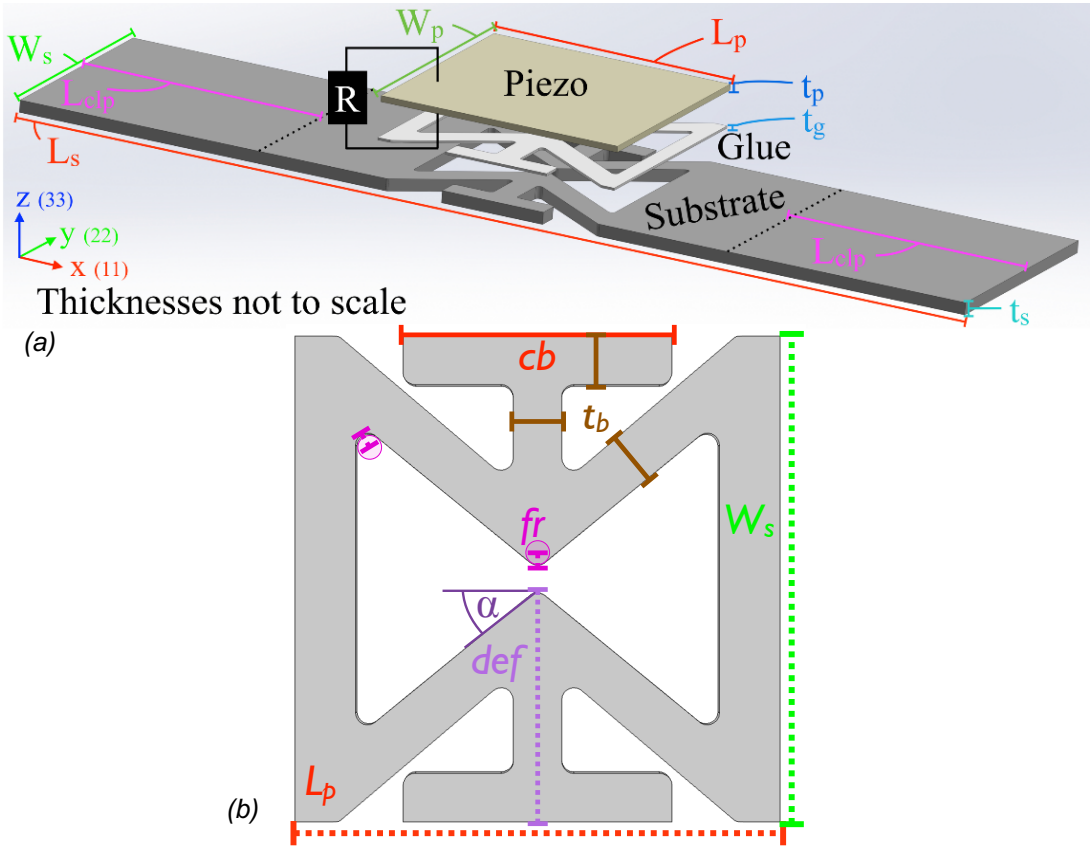

Figure 3-1: (a) Exploded render of model, annotated with external parameters and (b) parameters for the auxetic region (i.e. area of substrate directly under the piezo). Parameter values are listed in Table 3-1.

Table 3-1: Parameter values used in the model (final value given with modelled range where applicable).

Part	Parameter [unit]		Value (range)
Piezo-Layer	Length [mm]	L_p	20
	Width [mm]	W_p	20
	Thickness [µm]	t_p	180
	Resistance [kΩ]	R	384 (1-555)
Glue	Thickness [µm]	t_g	8 (1-10)
	TEL [GN/m³]	k_a	100 (1-1000)
Substrate	Length [mm]	L_s	80
	Width [mm]	W_s	20
	Thickness [mm]	t_s	1.15
	Clamp [mm]	L_{clp}	20
Auxetic Region	Beam Width [mm]	t_b	2 (1–3)
	Cell Angle [°]	α	33 (1–42)
	(Deformation [mm])	def	7.4 (1–9.8)
	Crossbeam [mm]	cb	11 (2–12.1)
	Fillet Radius [mm]	fr	0.47 (0.1–1.3)

Table 3-2: Model material properties

Material	Property [unit]		Value
PZT: PIC151 (Piezo-Layer) [133]	Density [kg/m³]	ρ_p	7500
	Compliance Matrix [µm²/N]	s_{11}^E	16.83
		s_{33}^E	19.00
		s_{55}^E	50.96
		s_{12}^E	-5.656
		s_{13}^E	-7.107
		s_{44}^E	50.96
		s_{66}^E	44.97
	Coupling Matrix [pC/N]	d_{31}	-214
		d_{33}	423
		d_{15}	610
	Relative Permittivity	ε_{11}	1936
		ε_{33}	2109
Epoxy (Glue)	Density [kg/m³]	ρ_g	1250
	Poisson's Ratio	v_g	0.35
	Elastic Modulus [GPa]	E_g	1.00
Steel: EN 10130 (Substrate)	Density [kg/m³]	ρ_s	7870
	Poisson's Ratio	v_s	0.29
	Elastic Modulus [GPa]	E_s	200

An equivalent plain energy harvester was also modelled to provide a baseline. It used a solid rectangular substrate with the same dimensions as described above but has no auxetic region. The piezoelectric material and excitation remained the same, and the epoxy layer filled the square area under this layer.

To account for the imperfection in the adhesive's bonding, thin elastic layers (TELs) were included at the epoxy's interfaces with both the substrate and the piezoelectric material. The TELs are a spring boundary condition in COMSOL which connects the opposing faces purely via visco-elastic forces, proportional to their relative displacement and velocity. The stiffness, i.e. spring constant per unit area, k_a, can be controlled; a high k_a corresponding to a stronger bond. These were necessary as the expected output without them was implausibly high; of the order of 0.6 & 1.5 mW from a mere 100 με excitation in the plain & auxetic models respectively[k]. By comparing the plain model under a range of k_a to the empirical work of Pozzi[56] (which used piezoelectric layers of the same size, in a similar surface mounted setup, with the same bonding agent), the required value of spring constant was found to be of the order of 100 GN/m^3. Part of the experimental testing would be to establish an empirical value for this fitting parameter.

3.1.2 Auxetic Region Parametric Study

The key parameters defining the shape of the substrate's re-entrant hexagonal auxetic region are the beam width, t_b, the deformation angle, α, the crossbeam length, *cb*, and the filleting radius in all the corners, *fr*. The parametric sweep study was used to optimise the auxetic region. The peak stress in the piezoelectric layer was almost always found to be less than a third of its tensile strength (35 MPa[92,93]); well below the 30 MPa safety factor. The limiting stress was in the substrate itself (yield strength: 280 MPa; safety limit: 200 MPa). The peak stress here would occur in one of the outward flexing corners; fluctuations seen in sections 3.1.2.1–3.1.2.4 are accompanied by a change in the most stressed corner. Its value and location varied slightly with different mesh qualities, but had sufficiently converged at the element size used here. The value of the

[k] This model was subsequently replicated in ANSYS by a master's student who found a similar overestimate in voltage output without these TELs, for both plain and auxetic models.

power output remained stable even at quite low average mesh quality[l]. Due to changing geometry during parametric sweeps the average element quality could vary between 0.6–0.7, with a typical minimum of 0.1–0.2. These values are sufficient for reliable modelling. The mesh was built from triangular prisms projected through all layers of the model, with many smaller triangles packed more densely around narrow and corner regions to have sufficient data regarding critical regions while reducing computation time. This mesh construction method was used for all models discussed in subsequent chapters, with similar element qualities. An example of the auxetic mesh is shown in Figure 3-2.

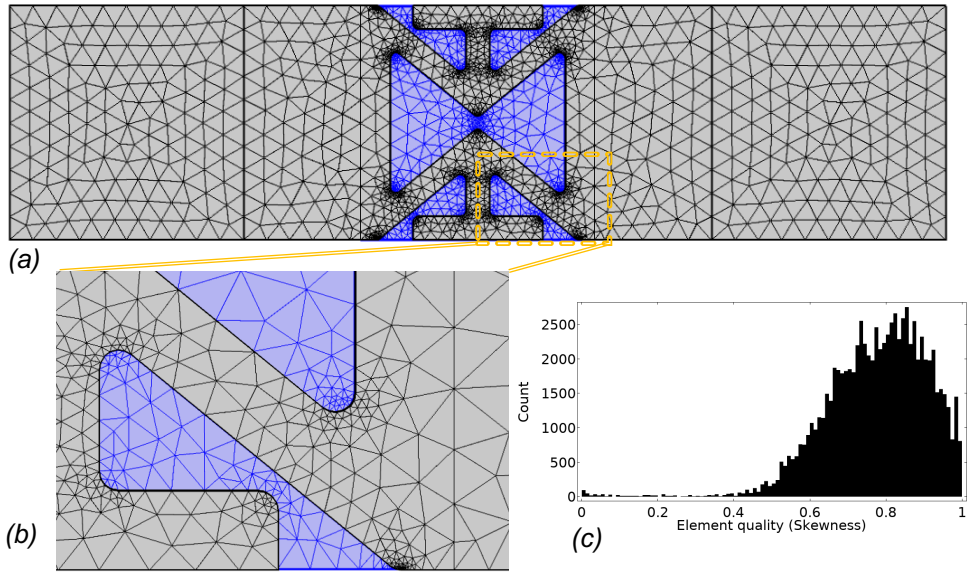

Figure 3-2: Example mesh viewed from underneath: (a) auxetic substrate and (b) Corner closeup, with PZT layer highlighted in blue; (c) Element quality histogram.

The following four subsections present a case study path, taking the result from prior steps onwards. The original process comprised many of these iterative pathways, beginning from different starting points to ensure that the outcome was consistent. Each pathway's results are based on at least 50 gradations between the minimum and maximum value of the parameter. Examples of the changing parameter's effect on the structure are given in part (c) of each figure to aid understanding in what they determine. The starting point here was: $\alpha = 35^{\circ}$; $fr = 0.3$ mm; with no crossbeam. The input was 10 Hz oscillation of 250 με, with the TELs' spring constant fixed to 100 GN/m^3 throughout.

[l] Mesh element quality is a value between 0 and 1, here determined by the skewness of the triangular mesh elements; i.e. how sharp the angles are and how much the side lengths differ (in a single element, and across the whole mesh). A lower value indicates a less reliable result.

3.1.2.1 Beam Width

The effects of varying the beam width, t_b, on the power output and the peak stress of the substrate are shown in Figure 3-3(a). The average stresses in the PZT are shown in Figure 3-3(b), along with the power output for comparison; this shows how each axis contributes to the power, with reference to equation *2–9*. As the beam width increases, the power arcs, with a maximum at 2.4 mm of 51 µW. The power's initial rise is due to the greater rigidity and contact area giving the beams more authority to strain the PZT. Beyond 2.4 mm the beams become too stiff, thus reducing the stress concentration effect and the transfer of strain to the PZT. Figure 3-3(b) shows the beam width affects the axial (i.e. parallel to the applied strain) and lateral (along the *y*-axis) stress components in a similar way, indicating b_t primarily affects the overall stiffness of the auxetic region.

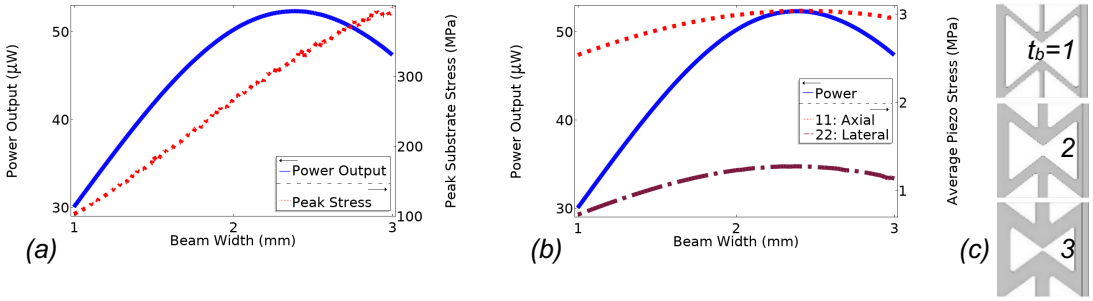

Figure 3-3: (a) Simulated power output from PZT (solid, smooth) and peak stress in substrate (dotted) against beam width, t_b; (b) Average piezo stresses in axial (dashed) and lateral (dot-dashed) directions, compared to power, against t_b; (c) Selected examples of t_b's effect on the structure.

The peak stress of the substrate generally increases with t_b despite the constant input strain. This can be attributed to the additional material in the flexing corners resisting motion. To help keep the substrate within the yield stress limit t_b = 2 mm was selected. The use of thinner beams is sub-optimal when considering only beam width, but allowed more space for a crossbeam; as discussed in section 3.1.2.3.

3.1.2.2 Re-Entrant Deformation Angle

How far the design re-enters itself is defined here by the deformation angle, α, but it could also use the deformation length, *def*; both are shown in Figure 3-1(b). This controls how far the unit can expand outwards when the structure is under tension. As the angle grows, stress is concentrated into tighter corners, but the

length of the beams also increases which can distribute their stress along a wider area; becoming less stiff overall. These factors explain the initial rise and subsequent fall in the peak stress shown in Figure 3-4(a). The optimum power output occurs at 30˚ (*def*=6.3 mm). Figure 3-4(b) shows that most of the power gain here comes from the lateral stress component, with only a small increase due the axial stress (from the reduced overall stiffness). The selected deformation is 33˚ (7.4 mm) as, as the lowered peak stress is desirable.

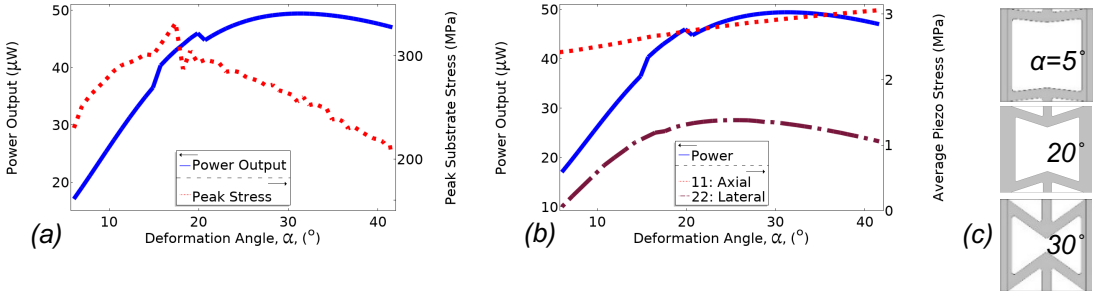

Figure 3-4: (a) Simulated power from PZT & peak substrate stress Vs. deformation angle, α; (b) Axial & lateral average stresses in PZT Vs. α; (c) α example structures.

The bump in the power output curve from around 15–20˚ is due to the angle of tension in the beams. Up until this region, the outward flexing corners in the middle of the substrate (between the angled beams and the truncated vertical ones, where the crossbeam will be added in the following section) are more than half the beam width further out than the inner corners between the angled beams and the rest of the substrate (where the peak stress usually arises). The tension is thus going across the angled beams. Through the raised portion, the corners become progressively closer to being in a horizontal line, making the tension more in-line with the beams and causing the peak stress to occur in the middle corners. The dip at around 20˚ marks the point where this tension is parallel to the applied tension, and thus there is only a minimal auxetic response (lowering the power output at this point). Beyond this angle, the beams are sufficiently re-entrant to push outwards again, stretching the PZT and increasing its output.

3.1.2.3 Crossbeam Length

A crossbeam is added to the truncated ends of the auxetic region to provide additional grip to the piezoelectric layer, which aids lateral strain transfer. Figure 3-5(b) shows all the benefit arises through this lateral component. Figure 3-5(a) shows the greatest output would be obtained when the crossbeam

is as wide as can physically fit into the available space (12 mm long); this full width would cause excessive stress in the PZT (where the two beams approach each other) and likely cause cracking here, as well as being difficult to laser cut. The substrate's peak stress otherwise remains quite stable throughout. Therefore, a length below this spike is chosen: 11 mm, around 91% of the available space.

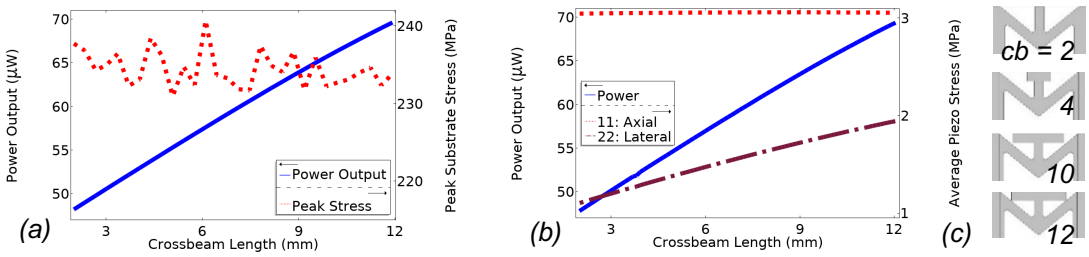

Figure 3-5: (a) Simulated power output and peak stress in substrate against crossbeam length, cb; (b) Axial and lateral average stresses in PZT against cb; (c) Effect of cb on the structure.

3.1.2.4 Filleting Radius

Sharp corners in the auxetic region, especially if flexing outwards, are prone to excessive stress concentration. Figure 3-6 shows the effect of filleting these corners to different radii; from the minimum most laser-cutters can achieve, 0.1 mm, up to the maximum curvature that fits behind the crossbeams, 1.33 mm. The reduction in power at larger radii is due to the added material in the corners which impedes flexing; this also accounts for the slight rise in substrate stress found in Figure 3-6(a) beyond ~0.6 mm. Figure 3-6(b) shows that the filleting radius affects both axes similarly. To maintain power while minimising the substrate's stress, filleting radius of 0.47 mm was selected.

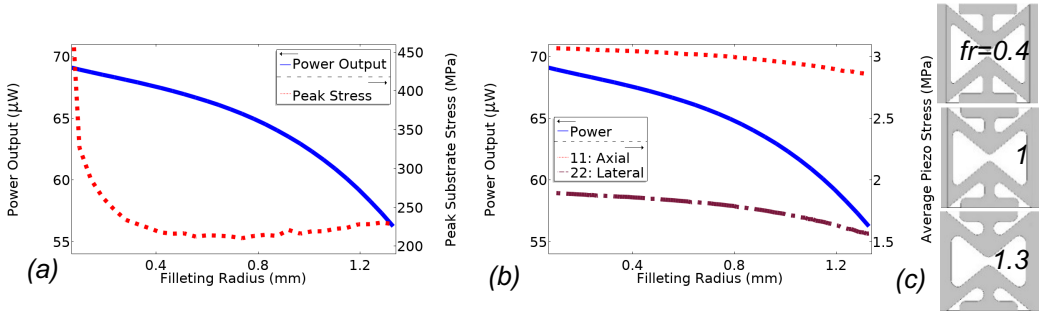

Figure 3-6: (a) Simulated power output and peak substrate stress Vs. filleting radius, fr; (b) Axial and lateral average stresses in PZT Vs. fr; (c) Example fr structures.

3.1.3 Modelling Results

The selected parameters (Table 3-1) result in an auxetic structure which would produce 66.8 μW from the given excitation (10 Hz, 250 με), while keeping the substrate's peak stress to 191 MPa. This peak is found at the apex of a corner flexing outward, see Figure 3-7(b). The peak stress in the piezo was almost always found to be <11 MPa, less than third of its tensile strength (35 MPa[92,93]).

The baseline for comparison was the plain harvester. Under the same model excitation, this generated 5.8 μW; with a peak stress of only 86 MPa (where the free substrate met the clamp, see Figure 3-7(a)). The final auxetic structure has power output 11.5 times higher than this plain. This gain factor was constant between structures when subjected to any matching excitations.

The modelled stress distribution in both designs are shown in Figure 3-7(a), with a slice view of the auxetic region substrate in Figure 3-7(b), and another of the piezoelectric layer alone in Figure 3-7(c). Note that the plain substrate has its stress distributed evenly along the free region (the green area between the clamps). By contrast, the auxetic substrate concentrates that stress into the pliable auxetic region. This concentration is an aspect of its power gain.

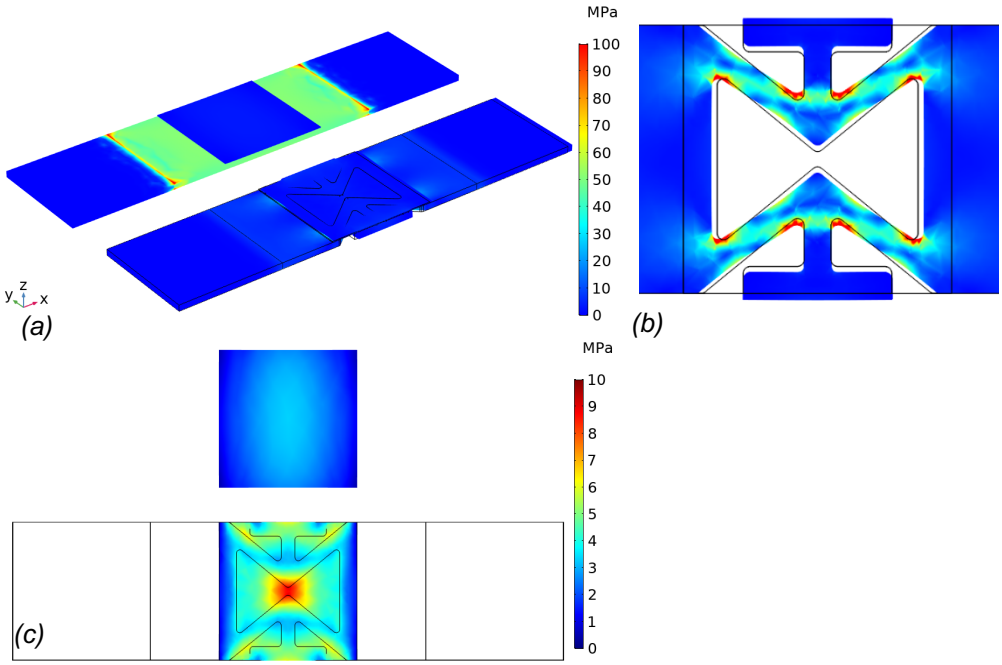

Figure 3-7: (a) False colour image of von Mises stress in: (a) Plain (upper left) and Auxetic models; slice through (b) auxetic region of substrate; (c) both piezoelectric layers (on independent colour scale). Colour ranges capped for visual clarity.

The lateral stretching of the piezo is however the more significant factor in the gain. The mean axial stress in the PZT is 3.0 MPa for the auxetic harvester, and 1.9 MPa for the plain one (a gain of 1.58, from the prior concentration effect). Meanwhile, their mean lateral stresses are 1.8 MPa and -0.46 MPa respectively; the sign change shows the piezo is placed in both axial and lateral tension by the auxetic substrate (with 3.91 times the magnitude). The combined effects lead to the 11.5 fold increase in power. The axial and lateral stress distributions in the PZT on both models are shown in Figure 3-8.

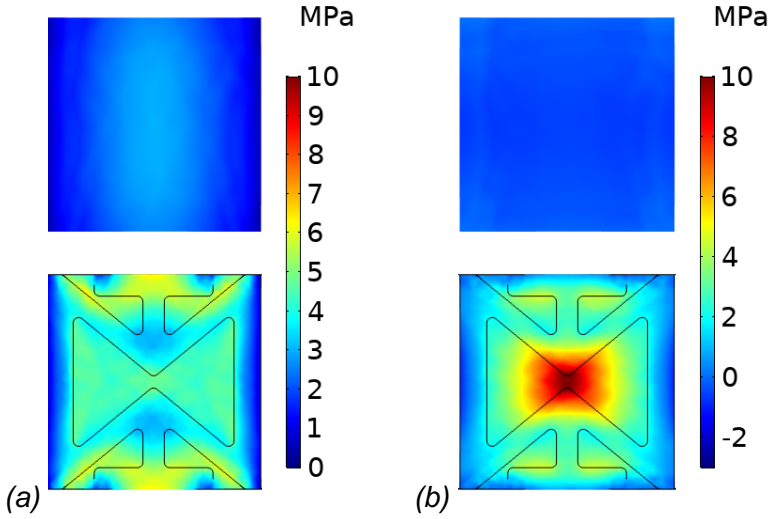

Figure 3-8: (a) Axial, 11, and (b) lateral, 22, stress distributions in PZT. Upper row shows the plain sample results, and the lower row shows the auxetic concentration.

The value of 100 GN/m^3 for the bonding adhesion, k_a, in the TELs was an assumption, and Figure 3-9 shows how the power at optimal load and peak stresses could be expected to vary with different spring constants (all at the same excitation as before). This demonstrates how a tighter bond (higher k_a) could lead to PZT damage from a given excitation; while it has much less impact on the stress in the substrate.

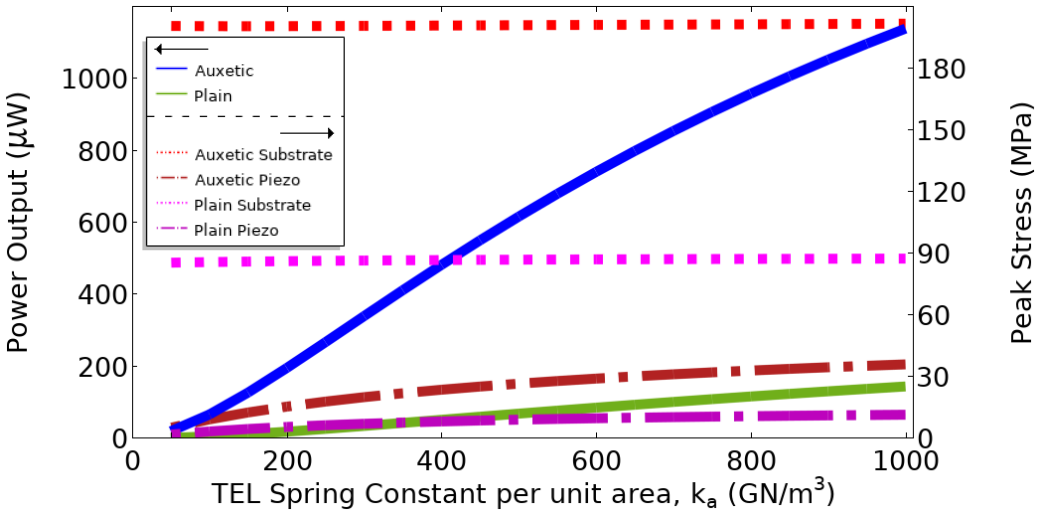

Figure 3-9: Comparison of simulated power output and peak stresses of Auxetic and Plain harvester designs against spring constant, k_a, in their Thin Elastic Layers.

The power output against k_a value is approximately linear in the region of interest (100-250 GN/m^3, see section 3.2.4) for both harvesters. Equations 3–2 & 3–3 define the fits to these respective regions (in the same units as Figure 3-9, with associated R^2 values). These were used to determine the appropriate k_a values to emulate a given sample from its experimental output.

$$P_{plain} = 0.1394\, k_a - 8.9016\,; \qquad R^2 = 0.9972 \quad \text{Eq.3–2}$$

$$P_{auxetic} = 1.3590\, k_a - 73.9508\,; \qquad R^2 = 0.999 \quad \text{Eq.3–3}$$

3.2 Experimental Method

3.2.1 Sample Manufacture

All plain and auxetic substrates were laser-cut from mild steel (BS EN 10130). Epoxy resin (Scotch-Weld™ 460[134]) was applied to the substrate surface and then the PZT layer (PIC151 from Physik Instrumente[133]) was placed on top. Excess epoxy was removed where possible. The sample was clamped between two melamine[m] coated MDF slabs in a vice for >24 hours while the epoxy cured at room temperature. Wires were then soldered to the PZT's electrodes. Three auxetic and two plain samples were successfully fabricated and tested; labelled with a letter if auxetic or a number if plain, and all shown in Figure 3-10.

[m] Melamine is a resin used for whiteboard surfaces. It provides a smooth, flat surface which is also quite resistant to epoxy; this was subsequently improved upon, see section 4.1.1.

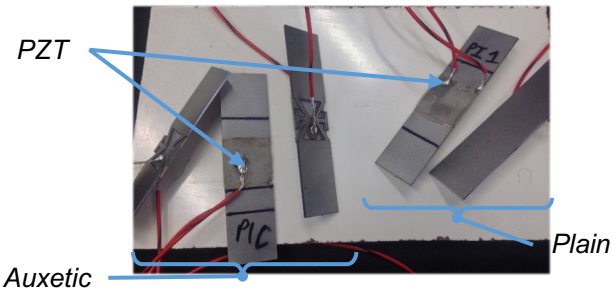

Figure 3-10: Three Auxetic (A, B & C) and two Plain (1 & 2) samples after epoxy is cured and wires attached.

3.2.2 Experimental Setup

For experimental validation, the harvester samples were clamped in an Instron ElectroPlus™ E10000 to a depth of ~20 mm at each end, as shown in Figure 3-11. The machine applied a harmonic strain to the sample for 10 s at an amplitude of 250 με peak-to-peak (i.e. a total displacement of 10 μm) at a frequency of 10 Hz to compare to the computer model. The excitation was controlled by displacement and was preceded by a 3 s linear extension to the midpoint of the excitation, 1 μm more than the mid-to-peak amplitude (i.e. to 6 μm in this case) to keep the sample in tension throughout the test; this was relaxed to zero displacement between tests. This adds to the maximum applied force, but only the oscillation amplitude affects power. The harvester's output wires were connected to a variable resistor (1-999 kΩ) to act as a load. The voltage across this variable resistor was recorded by a data log (National Instrument cDAQ-9174 with NI 9229 card) at 2000 samples per second. The total load resistance becomes the variable resistor in parallel with the 1 MΩ input impedance of this data log. The excitation was repeated 15 to 25 times at different load resistances to obtain the spread of datapoints shown in section 3.2.4; the optimum load and maximum power output could be found through fitting these points. The amplitude or frequency of the excitation was changed, and the tests repeated.

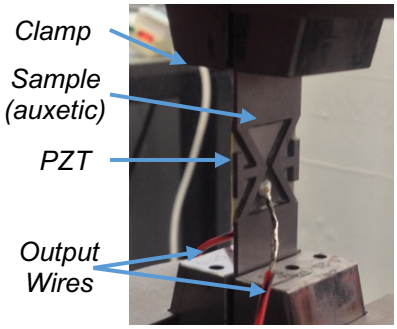

Figure 3-11: An auxetic piezoelectric energy harvester installed in the Instron.

3.2.3 Data Analysis

To find the average power generated over a cycle, the instantaneous power, P_i, was calculated ($\mathrm{P_i} = \mathrm{V_i^2/R}$) for each voltage measurement, V_i, at the load resistance throughout that test, R. The instantaneous energy, E_i, over the time interval, t_i, was calculated ($E_i = P_i\ t_i$) and integrated with the cumulative trapezoid method to find the accumulated energy. Its gradient is approximately linear after a few seconds (the Instron has an envelope on the excitation for its own, and the sample's, protection); this gradient is the average power output. This method generally gives a near identical result to averaging the instantaneous power over that period, but unambiguously eliminates the rise time while also filtering out large spikes. This gradient then becomes a datapoint on the results shown in section 3.2.4. An example of raw data, taken from Plain 2 excited at 10 Hz, 250 με, 478 kΩ (load includes NI interface), is shown in Figure 3-12 (the Instron excitation and voltage measurements are independent so the time axes are only synchronous for parts (b-d)).

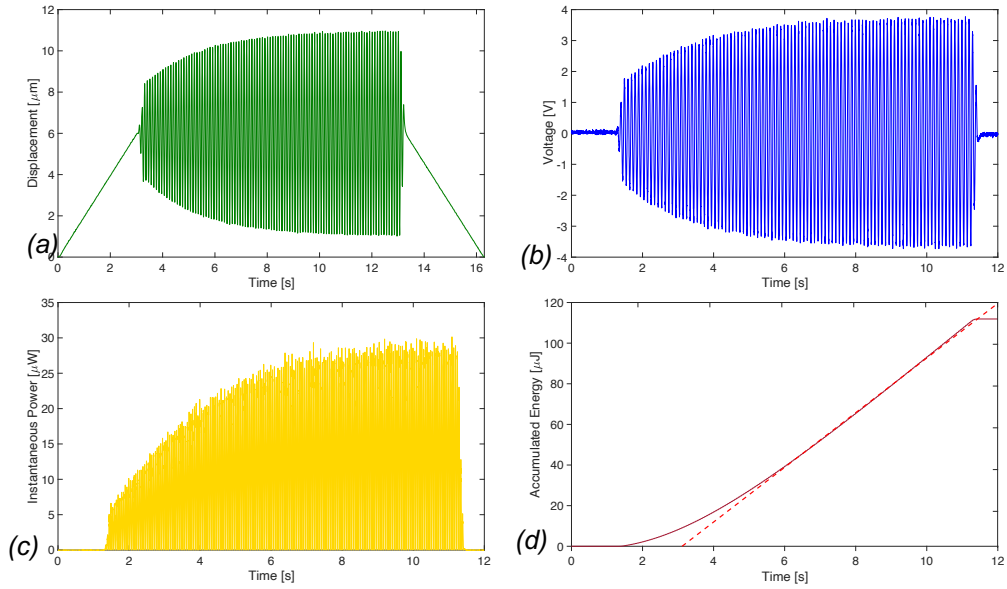

Figure 3-12: Example set of raw results showing a typical (a) Input Displacement, with the resultant: (b) Voltage output, (c) Instantaneous Power output, and (d) Accumulated energy with linear fit (dashed gradient is the stabalised cycle power).

Once the cycle power was found at each load, the optimal output was found by comparison to equation 3–4[55,75]; here equation 3–5 factorises the fitting parameters between this and equation 3–6. Equation 3–4 assumes the stresses,

T_1, T_2, & T_3[n], on the piezoelectric material are of constant and uniform sinusoidal amplitudes[o], however this is rarely the case. Fortunately for fitting purposes, their equivalent values did not need to be calculated. For any given excitation of a particular sample, both factors are constant across any load resistance.

$$\boldsymbol{P} = \frac{\boldsymbol{R}(2\pi f)^2}{2\left(1+\boldsymbol{R}^2\left(2\pi f\ \varepsilon_0\varepsilon_{33}\frac{L_p\,W_p}{t_p}\right)^2\right)}(d_{31}T_1 + d_{32}T_2 + d_{33}T_3)^2 \qquad \text{Eq.3–4}$$

$$\mathrm{A} = (2\pi f)^2(d_{31}T_1 + d_{32}T_2 + d_{33}T_3)^2/2\ ;\ \mathrm{B} = \left(2\pi f\ \varepsilon_0\varepsilon_{33}\ L_p\,W_p/t_p\right)^2 \qquad \text{Eq.3–5}$$

$$\boldsymbol{y} = \frac{A\,\boldsymbol{x}}{1+B\,\boldsymbol{x}^2} \qquad R_{Opt} = 1/\sqrt{B}\ ;\ P_{Opt} = A/2\sqrt{B} \qquad \text{Eq.3–6}$$

The experimental results against resistance shown in section 3.2.4 used a fit of the form of equation 3–6; the optimum load and power output were then found directly from its fitting parameters. If this load fell outside the tested resistance range then it could only be considered a guideline because the fitting becomes unstable without data either side of its peak.

Error bars were derived from the noise floor and accuracy of all the measuring instruments, the quality of data fitting at each step, and a factor to account for variations between repeated experiments (arising largely from misaligning the sample in the clamps, i.e. deviations from vertical or intended clamping length).

3.2.4 Results and Discussion

Figure 3-13 shows the experimental results from each of the five harvester samples when excited at 10 Hz, 250 με, alongside their equivalent simulations. The optimum power output and load resistance of each sample was found through the above method, and are listed in Table 3-3. The simulation emulating each sample uses the k_a value which delivers this optimal output, using equations 3–1, 3–4 and Figure 3-9; at 10 Hz, the model's optimum load is 384 kΩ. The k_a values are all in the expected order of magnitude, though up to double the assumed value, and are in reasonably close agreement to each other.

---

[n] T_3 is negligible beside T_1 and T_2, at least for surface mounted piezoelectric materials.

[o] If all strains on the piezoelectric material are known, constant, and uniform, then the rightmost bracket of eq.3–4 can be replaced with $(e_{31}S_1 + e_{32}S_2 + e_{33}S_3)^2$. S_3 is not negligible.

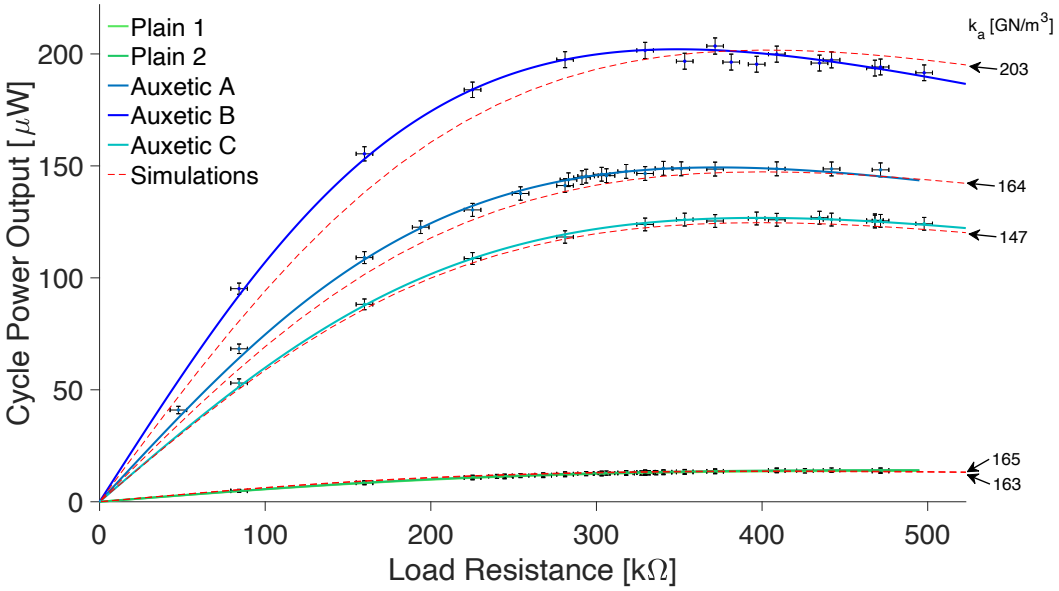

Figure 3-13: The experimental and simulated results from five harvester samples when excited at 250 με, 10 Hz. Simulation for each sample shown with TEL k_a value to meet its optimal output.

Table 3-3: Optimum values from Figure 3-13, with matching TEL spring constant, k_a.

Sample	*R_{Opt} [kΩ]*	*P_{Opt} [μW]*	*Gain*	*k_a [GN/m^3]*
Plain 1	*474*	*13.8*	*—*	*163*
Plain 2	*477*	*14.1*	*—*	*165*
Auxetic A	*373*	*149.3*	*10.7*	*164*
Auxetic B	*349*	*202.1*	*14.5*	*203*
Auxetic C	*398*	*126.8*	*9.1*	*147*

These results show that the auxetic samples generated dramatically more power than the plain ones from the same excitation. The gain of each sample (comparing its optimal output to the average of the two plain ones as its baseline) is listed in Table 3-3. The average gain due to the auxetic region was found to be 11.4 times.

The two plain samples were near identical in their response, but the auxetic samples each varied significantly from each other. Repeating tests with the same sample produced quite stable results, as demonstrated in Figure 3-14; the slight differences arose due to imperfect alignment of the sample when positioning it into the Instron. The difference between samples can be explained by excess epoxy having leaked into the flexing corners of the auxetic region, increasing the sample's stiffness by an uncontrollable degree. This only affected the auxetic samples, as excess epoxy leaking out the sides of the plain samples had no significant impact on their overall stiffness. Tuning the k_a value can account for this in a model. An automated fabrication process would greatly reduce this issue.

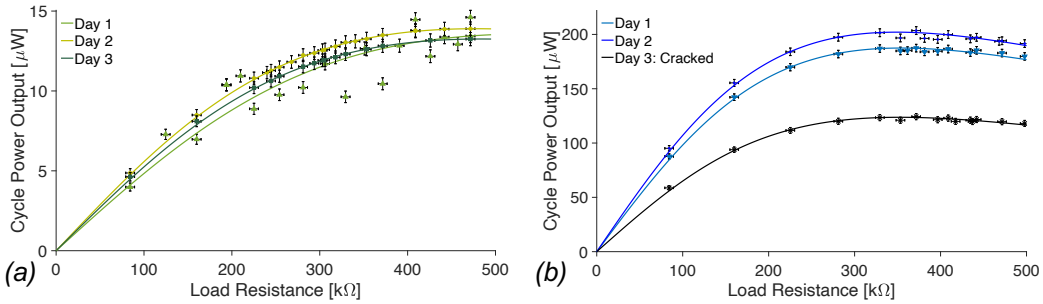

Figure 3-14: Repeatability tests at 10 Hz, 250 με on a given sample, using: (a) Plain 2 and (b) Auxetic B; note its final dataset came after a small crack developed in the PZT.

The gain factors from this input are also constant for different excitations. Figure 3-15 shows that as the amplitude of excitation is increased (while keeping the same frequency) the power output will increase quadratically. Figure 3-15 also shows two datapoints taken after hairline cracks formed in the piezoelectric layer during the test at 13 μm (325 με). These apparently superficial cracks, indicated in Figure 3-16, were only found upon shining a bright light through them. These datapoints have been excluded from the quadratic fitting on this basis.

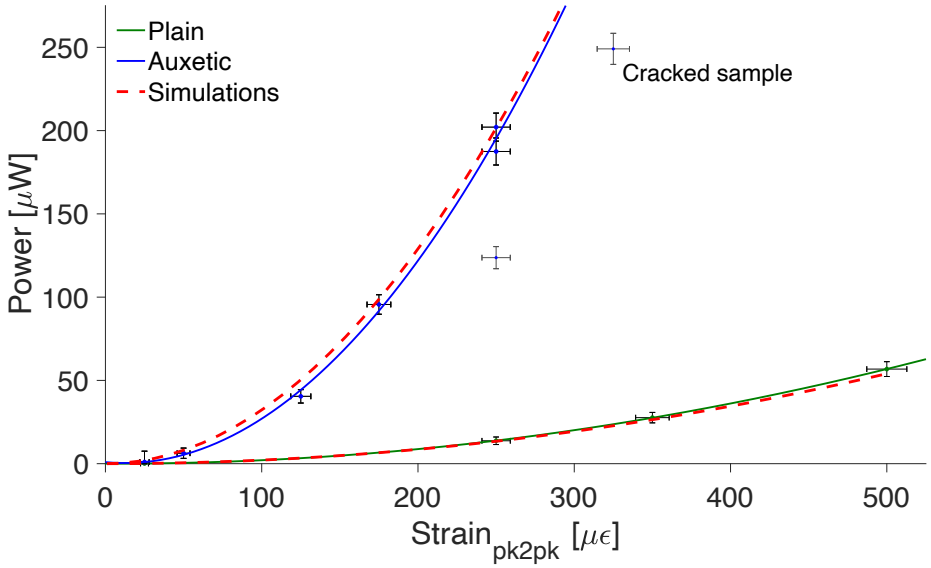

Figure 3-15: Experimental and simulated results of optimal power outputs from plain and auxetic samples excited at a range of strain amplitudes, all at 10 Hz.

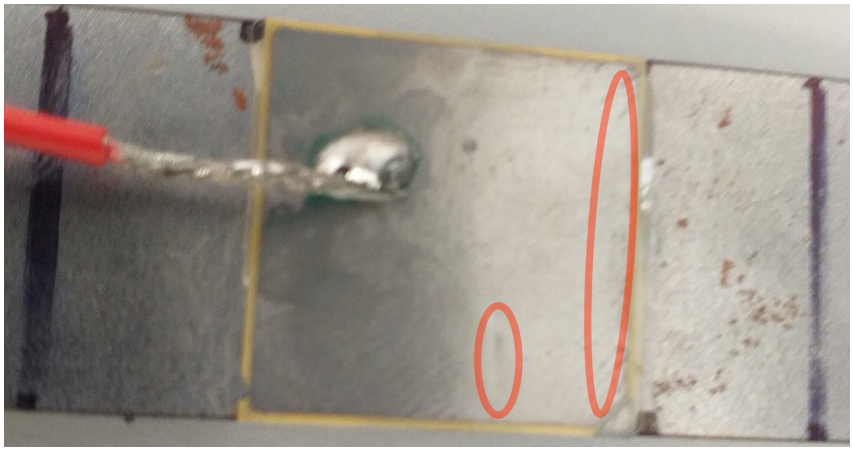

Figure 3-16: Photograph of cracked PZT on auxetic sample. Damage indicated in red rings.

Figure 3-17 shows the experimental and simulated effects of increasing the frequency of the applied excitation (while keeping the same amplitude). This resulted in a linear increase in power output. No auxetic sample remained undamaged long enough to obtain a full set of frequency sweep results. The presented results from sample B are therefore only to indicate that the auxetic samples also has a linear relationship, even when cracked (note that these excitations were not contributing significant further damage, as their amplitude was less than the cause of the crack). This damaged piece of PZT was still able to achieve a greater output than the plain sample. The simulated auxetic output now only accurately predicts the 10 Hz datapoint from which it was determined. The plain sample's simulation is well correlated to the experimental results.

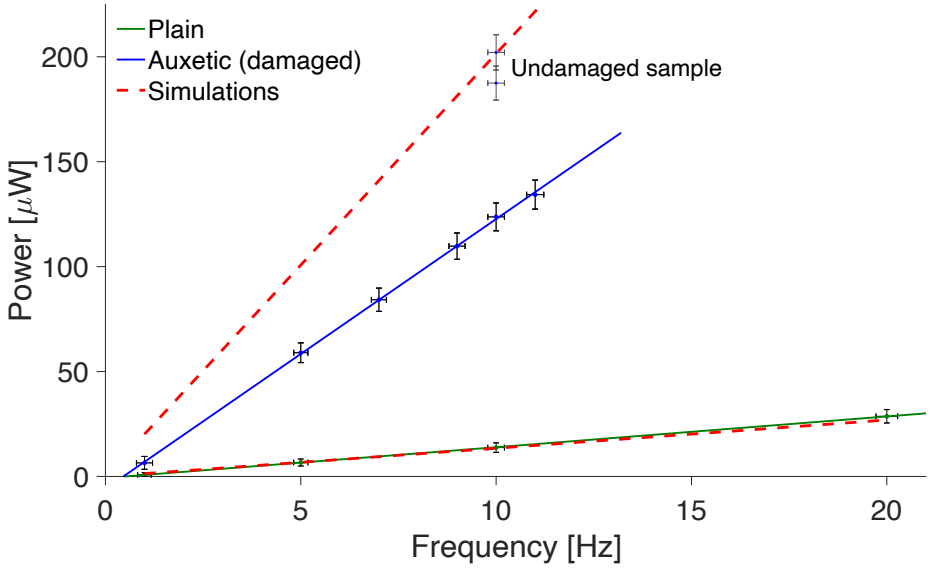

Figure 3-17: Experimental and simulated results of optimal power outputs from plain and auxetic samples excited at a range of frequencies, all at the same 250 με strain.

All simulations shown in Figure 3-15 and Figure 3-17 maintain the same k_a values for each sample; as given in Table 3-3. When the input strain was changed, this value continued to yield a close match to the strain sweep; until the stress became too high and the PZT cracked. Naturally this damage made the same k_a value ineffective at predicting the auxetic sample in the frequency sweep. The linear relation remained consistent however, and the simulation matched the plain sample well. That the same k_a value can be used to accurately predict a sample's harvested power under a range of tolerable conditions indicates it is a suitable method for modelling the adhesion strength of the bonding layers.

This cracking was an issue for the auxetic harvester. Sample A cracked during a test at 14 μm (a maximum applied load of 230 N), and sample C broke shortly after its first test at 10 μm (196 N). By comparison, a plain sample at the 10 μm excitation experienced 370 N peak-to-peak, and up to 730 N (during the 20 μm excitation), with no damage. The stress concentration effect was too strong.

The original design simulations indicated that the peak stress in the PZT would be within the safety factor (30 MPa) of its tensile strength (35 MPa[92,93]) even above 500 με input, but with was while assuming k_a=100 GN/m^3. As shown in Figure 3-18 (and suggested by Figure 3-9) a stronger bond might push the PZT over its stress limit at smaller excitations. Revising the simulation to 200 GN/m3, the maximum strain input safely below the limit would be 385 με. Recall that to keep the sample in tension the maximum strain on the sample will be 1 μm (25 με) more than the stated peak-to-peak strain, suggesting a maximum excitation of 14.4 μm peak-to-peak. This is still more than any auxetic sample endured, perhaps due to crystal imperfections or defects introduced during fabrication. A larger safety factor is used in later chapters, limiting peak PZT stress to <25 MPa.

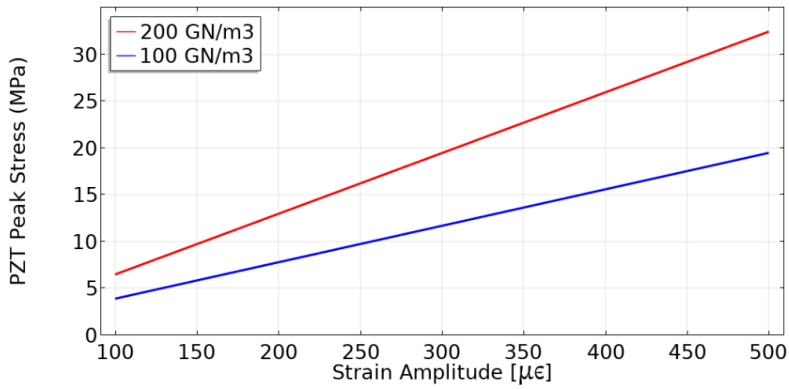

Figure 3-18: Simulated peak stress in PZT on auxetic substrate when under various excitation amplitudes (peak-to-peak), with two different k_a values in the TELs.

Even with this larger safety factor, it's clear this auxetic energy harvester would be unsuitable for applications in turbulent high-strain environs, such as aeroplanes, and would be more useful for infrastructure monitoring; where strains are typically <200 $\mu\varepsilon^{33}$ and predictable in advance. The auxetic design could concentrate these small ambient strains, focusing them into the piezoelectric layer and thus generate a more useable power output in areas otherwise considered unviable for harvesting. These proof of concept pieces were a step toward this, but were too small to generate sufficient power for remote sensor nodes. They have provided some validation of the design method.

The natural development of this auxetic design would be a multi-unit re-entrant honeycomb as the auxetic region, akin to the example shown in Figure 2-8, under a larger piezoelectric layer, to harvest more energy; see chapter 5. The TEL's ability to model the epoxy's bonding strength still required further investigation. Since the PZT cracking was a significant limitation, an investigation into stronger piezoelectric materials was also launched; see chapter 4.

3.3 Conclusion

The work in this chapter has shown that a simple auxetic geometry can deliver a significant increase of 9.1-14.5 times the power output of a strain energy harvester over a baseline plain equivalent. The gain factor of a sample remained constant for any matching input excitation. This improvement was achieved with the aid of a finite element model to optimise the prospective design for power output, within material stress limits. The modelling process required thin elastic layers to account for the imperfect bonding between the epoxy and other components, which served as a fitting parameter to the model. The bonding was stronger than initially anticipated, which led to many instances of the PZT cracking during tests of the auxetic samples. The modelling procedure and concept were nonetheless proven as quite effective.

4 Experimental Study of Lithium Niobate Piezoelectric Material

Following on from the previous chapter, where the auxetic substrate brought more power from the PZT but also broke it under modest forces, a stronger material was sought. A set of single crystal lithium niobate (LN) elements made were supplied by Ausrine Bartasyte and Giacomo Clementi of the Femto-ST Institute[82]. These were the same size and thickness as the PZT used previously, so a direct comparison can be drawn by using the same substrate design.

This short chapter will begin by discussing the sample manufacture, testing procedure, and data analysis methods in section 4.1. These are largely similar to the prior method, though because of LN low permittivity a high impedance SourceMeter was required for voltage measurements. The resistance sweep process was also automated; these are both covered in subsection 4.1.2. Following this are the LN results and discussion in section 4.1.4, including a comparison to PZT. Finally the conclusions on LN are given in section 4.2.

4.1 Method

4.1.1 Manufacturing

The LN samples were all manufactured in a similar way to the PZT ones, as discussed in section 3.2.1. Each substrate was laser cut from mild steel (BS EN 10130), epoxy was applied (Scotch-Weld™ 460[134]) to the middle area and the LN piece placed the on top. To ensure the crystal's Y-128˚ cut[p] was correctly aligned to the substrate, the LN was supplied with a mark on each top right corner. The samples were left to cure for over 24 hours under pressure between two wooden boards with card covered in resin proof tape[135, q]. The mirror smooth aluminium electrodes on the LN were more difficult to solder to, so thinner wires were used to reduce the thermal mass. Four samples were successfully made: two plain and two auxetic. They were made in two pairs: Plain 1 &

[p] This angle was intended to ensure the LN would be most resilient to applied stress.

[q] The tape prevents the epoxy from binding to the surface[135], then the card backing allows for a safe peeling off. The card layers were held together with spots of Blu Tack to prevent constituents sliding around during the application of pressure.

Auxetic A, and Plain 2 & Auxetic B; all shown in Figure 4-1. The former pair used less pressure than the latter pair, due to excessive caution, resulting in a glue layer ~10 μm thicker and a lower power output, as shall be seen in section 4.1.4. The latter pair's glue was similar to the thickness of the original PZT samples.

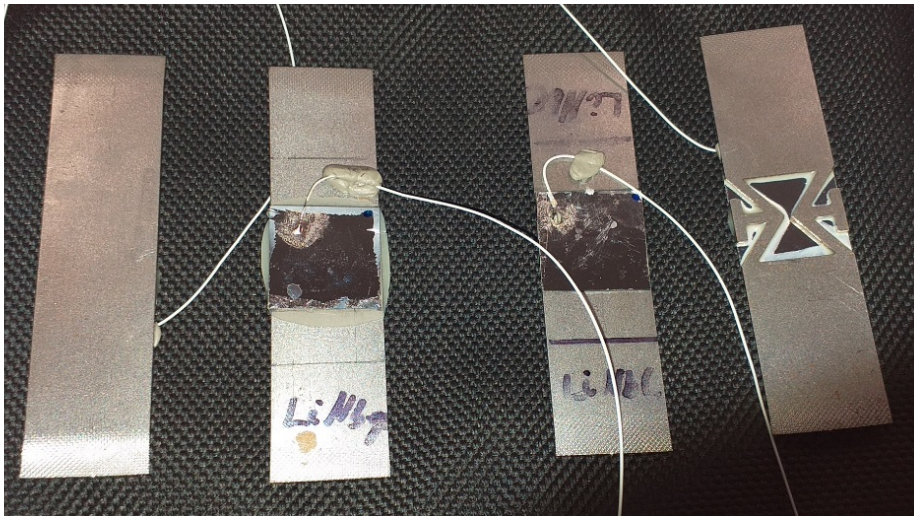

Figure 4-1: Photograph of lithium niobate samples. The two on the left are plain, the two on the right have auxetic substrates. The excess epoxy may be seen in white.

4.1.2 Experimental Setup

As the samples are similar to the prior PZT ones, the testing method is also similar to that described in section 3.2.2. The sample is clamped to a depth of 20 mm at each end into the Instron, which applies a sinusoidal extension of a set amplitude and frequency. Prior to excitation the sample is pre-loaded to 1 μm more than the amplitude to ensure the sample is in tension throughout.

The first difference was the use of the Agilent U2751A Switch Matrix relay to ratchet through the different load resistances; shown in Figure 4-2. It connected one of the four row resistors (R1-R4 in Figure 4-3) to one of the eight column ones (C1-C8 in Figure 4-3) in turn, giving 32 possible resistance values; a diagrammatic circuit is shown in Figure 4-3. With this, the load resistance on the sample could be steadily increased without having to stop the Instron's excitation; allowing a continuous 200 s long sinusoidal input and making data collection much quicker. The voltage measurements were started only after the excitation had achieved a steady amplitude (this took 1-5 s, depending on frequency). Without this rise time appearing in the voltage data, less than five seconds were required at each load before switching to the next one. The total voltage recording

thus took 160 s (which allowed some leeway during testing). Before use on the LN samples, this was trailed on the surviving plain PZT ones from the previous chapter and the resulting power output was almost identical; see Appendix B.I.

The other change to the method was use of the Keithley 2612b System SourceMeter® to measure the voltage. This was required because the impedance of the LN at low frequencies (<60 Hz) was higher than that of the LabVIEW interface (~1 MΩ)[r]. The SourceMeter's internal impedance is ~1 GΩ and was therefore suitable. It could only run at 500 samples per second to keep the whole record, but this was sufficient for analysis.

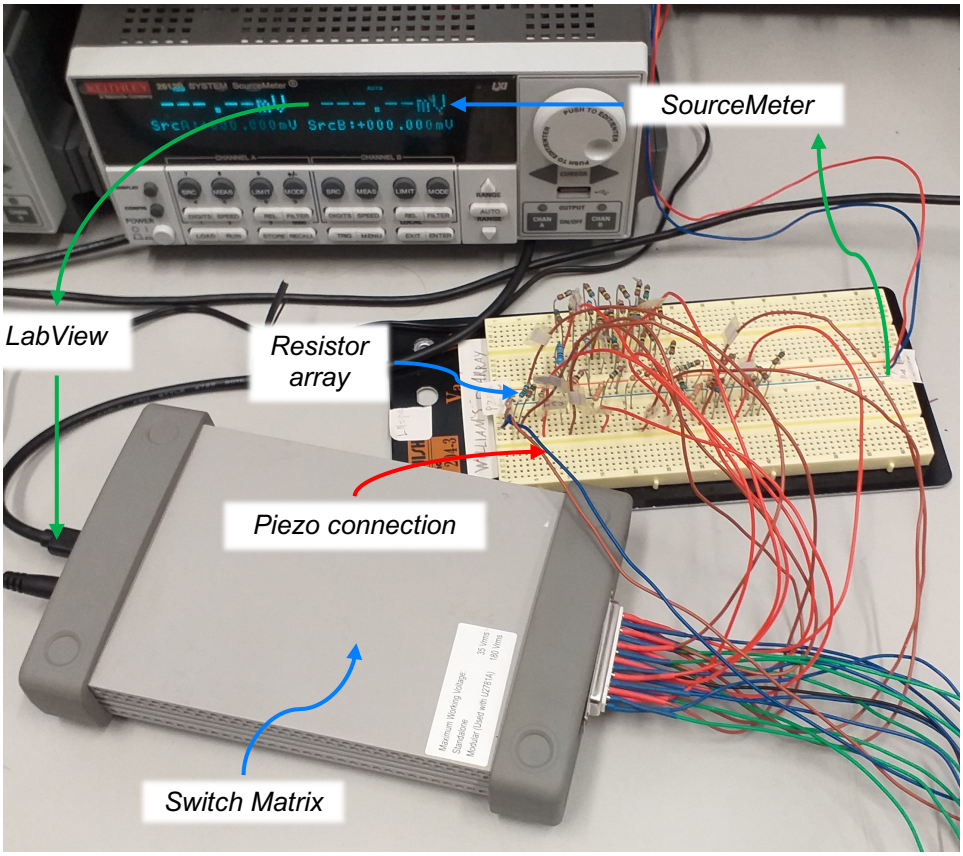

Figure 4-2: Photo of SourceMeter and Switch Matrix connected to the resistor array.

[r] Using this caused an apparent saturation of the power output above an optimum load.

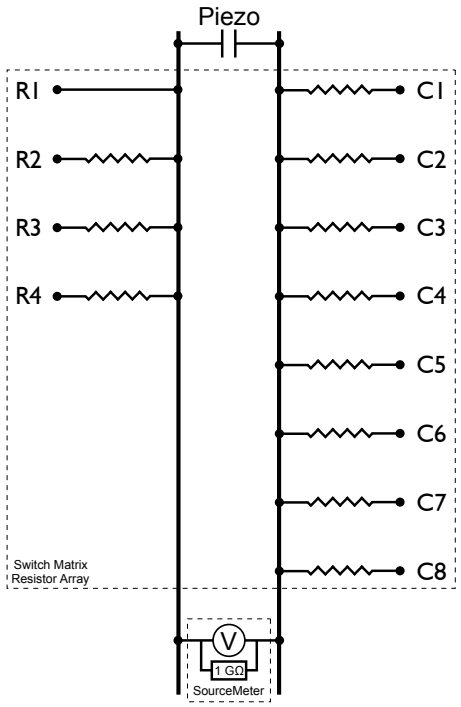

Figure 4-3: Diagram of Switch Matrix circuit. During a measurement one R node is connected to a C node to provide the load on the LN layer in turn, giving 32 combinations per test.

Table 4-1: Resistance values for Switch Matrix nodes, shown in Figure 4-3. Total resistance is R(i)+C(j).

Row / Column Node	*Resistance [MΩ]*
R1	*0*
R2	*25.829*
R3	*55.652*
R4	*81.19*
C1	*0.999*
C2	*2.200*
C3	*3.302*
C4	*4.702*
C5	*6.870*
C6	*10.307*
C7	*15.972*
C8	*20.065*

4.1.3 Data Analysis

With the automated resistance sweep the data processing was modified from that used prior. Figure 4-4 shows an example of an (a) input excitation and (b)-(d) the resulting electrical outputs of the Auxetic B sample excited at 10 Hz, 10 µm. Note, these electrical measurements' time axes are offset to the excitation. The Switch Matrix initial activation and switching between states every 5 s could cause spikes in the measured voltage[s], which may be seen in Figure 4-4(b). All voltage data within 0.25 s either side of these switches were thus filtered out from the subsequent analysis to remove these transient electrical effects (leaving the white spaces in parts (c) & (d)). This gave 4.5 s of steady voltage signal at each attached load resistance from which to calculate the cycle power output as described in section 3.2.3. An average of the instantaneous power in this timespan would give a good estimate of the average power, but if the signal were near the noise floor (most common for the lower amplitudes and frequencies,

[s] The Switch Matrix is briefly open, with only the SourceMeter's internal impedance as load.

especially from the plain samples) then this could bias that average. The gradient of the accumulated energy at each resistance was therefore used as before. At most excitations the difference was negligible. This set of gradients then supplies each point in the power verses load results shown in section 4.1.4.

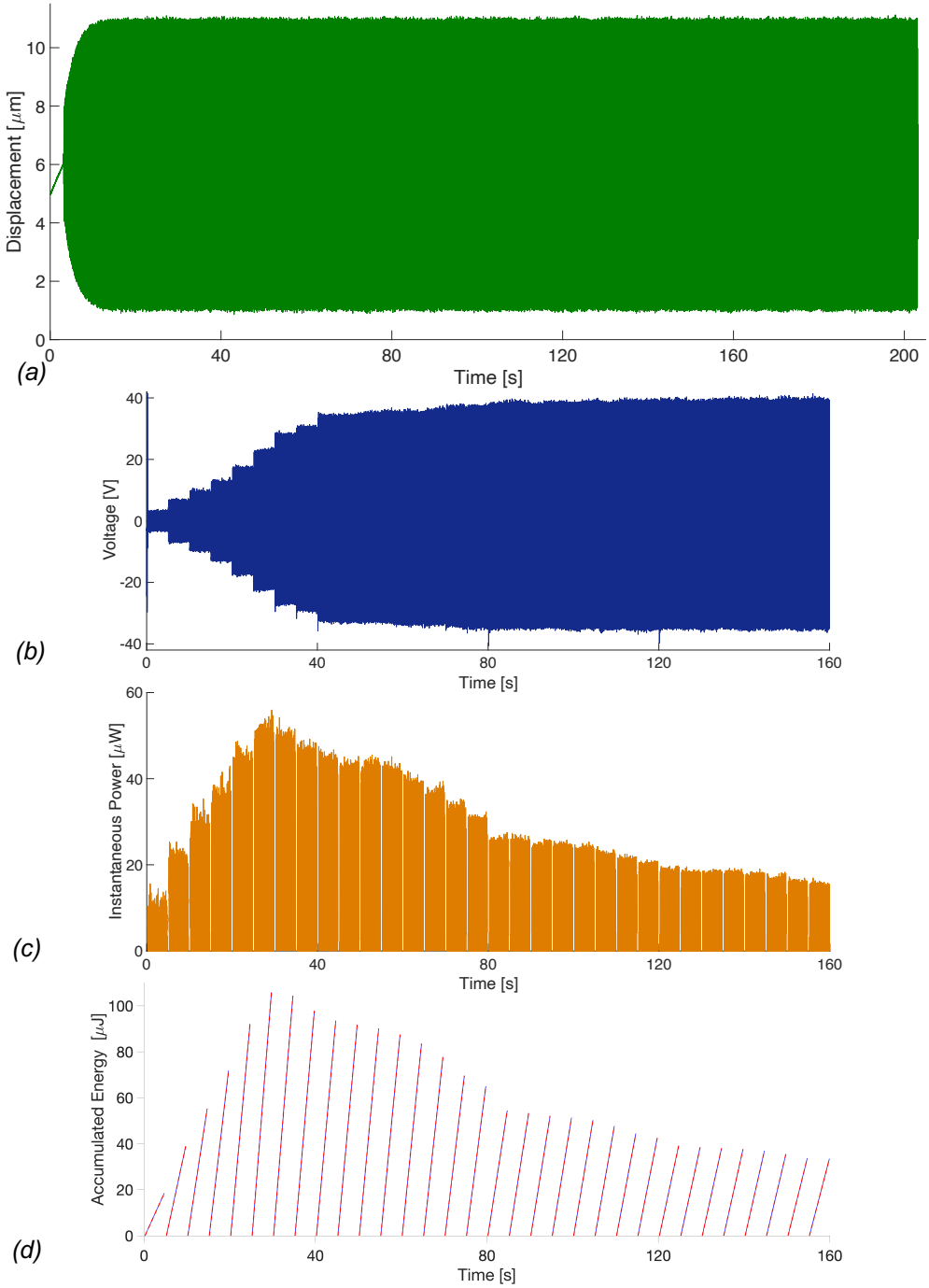

Figure 4-4: Example of a single 250 με, 10 Hz excitation from the auxetic B sample, showing: (a) Input displacement against time; with the resulting (b) Voltage output, (c) Instantaneous power output, and (d) Accumulated energy at each resistance.

4.1.4 Results and Discussion

The best resistance sweep results from each sample excited at 10 Hz, 10 μm (250 με) are shown in Figure 4-5. The optimum load and power outputs are listed in Table 4-2, derived using equation 3–6. This fit's optimum is often a slight overestimate compared to the data, presumably due to the LN's off-axis cut, but overall reflects the expected piezoelectric behaviour. These results demonstrate a clear difference between the first pair of samples made (*1* & *A*, dot-dashed lines) and the latter pair (*2* & *B*, solid lines); where the latter plain sample was on par with the original auxetic sample. Like the PZT samples discussed in section 3.2.4, each sample's output was consistent under the same excitation; what small variations there were related to the inconsistencies in positioning the sample into the Instron jaws.

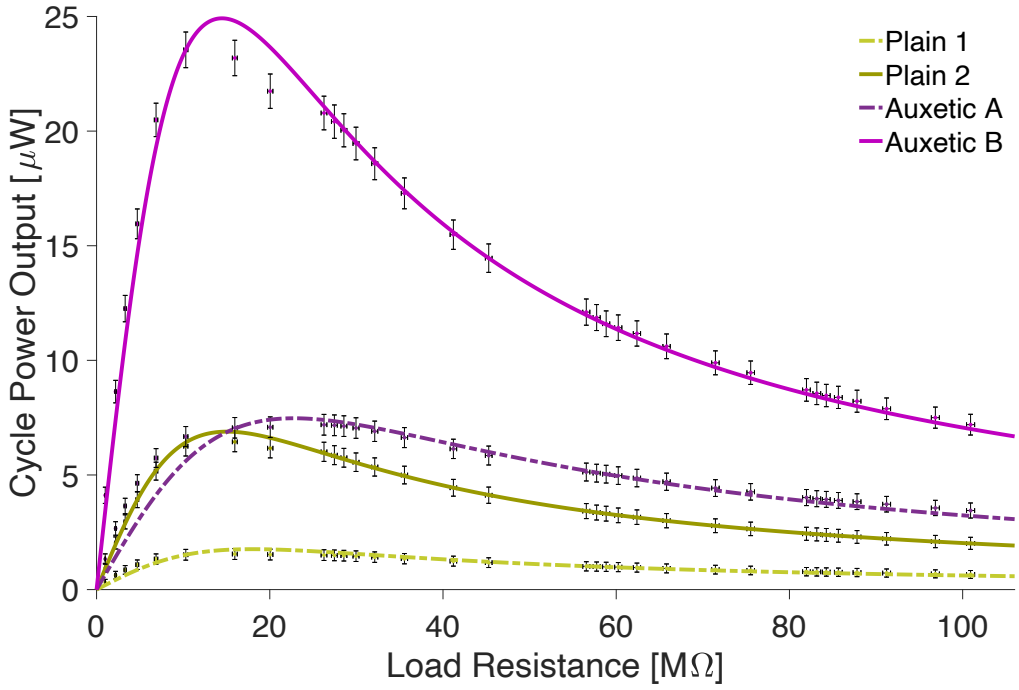

Figure 4-5: Experimental results for the four LN sample harvesters. Power against load resistance at a 10 Hz, 10 μm excitation.

Table 4-2: Optimum values from Figure 4-5. Gain factors given compared to their co-manufactured plain samples: A/1; B/2.

Sample	*R_{Opt} [MΩ]*	*P_{Opt} [μW]*	*Gain*
Plain 1	*23.4*	*1.8*	—
Plain 2	*15.1*	*6.9*	—
Auxetic A	*22.8*	*7.5*	*4.2*
Auxetic B	*14.5*	*24.9*	*3.6*

The fairest way to judge the gain of the auxetic samples was against the plain sample manufactured with them, as listed in Table 4-2. The difference between

these gain factors is proportionately within the variation found for the PZT samples, and can be accounted for in the imperfections of the manufacturing process. The difference between the two pairs of samples demonstrates how critical the bonding layer can be. More consistent gain would be found with industrial fabrication methods.

4.1.4.1 Amplitude Sweep

Repeating the tests at different excitation amplitudes yields the same quadratic increase in power output as found from the PZT in Figure 3-15. These results are shown in Figure 4-6. Thanks to the automated resistance sweep, and the greater resilience of the LN, data could be taken from a wider range of amplitudes. The LN layers on both latter samples withstood 500 με (20 μm peak-to-peak) with no sign of damage or subsequent diminution in power output. On the plain 2 sample, this strain amplitude corresponds to a 752 N peak-to-peak range, and 415 N on the auxetic B sample.

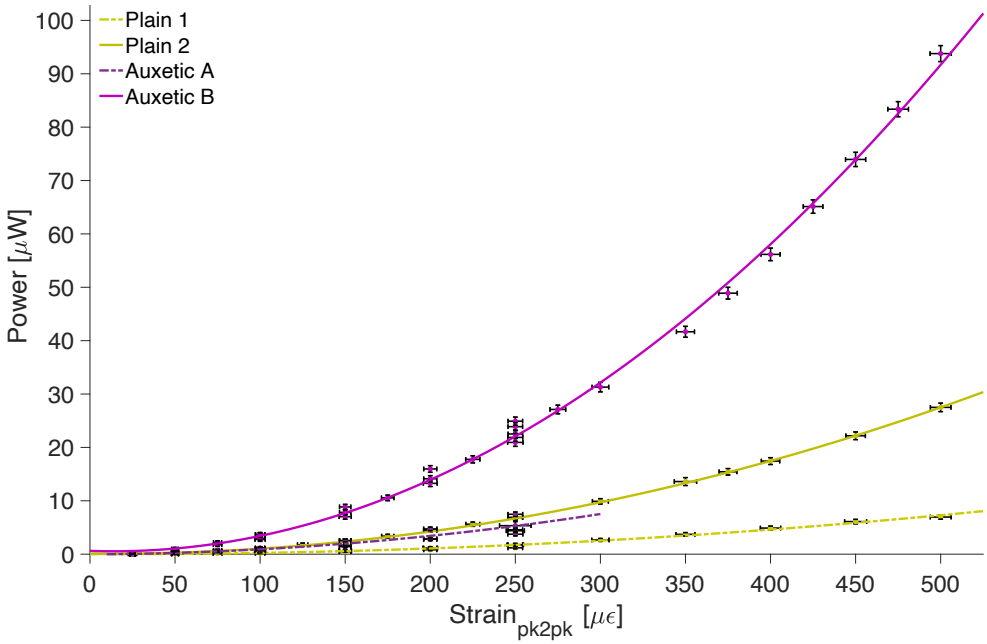

Figure 4-6: Results of power harvested from a range of input excitation amplitudes for the LN samples, while maintaining a constant input frequency of 10 Hz.

4.1.4.2 Frequency Sweep

Running the tests at a range of input excitation frequencies produced the expected linear increase in power output for all samples, as shown in Figure 4-7. In both the frequency and amplitude sweeps, the Plain 2 sample proved a superior harvester overall than the Auxetic A harvester.

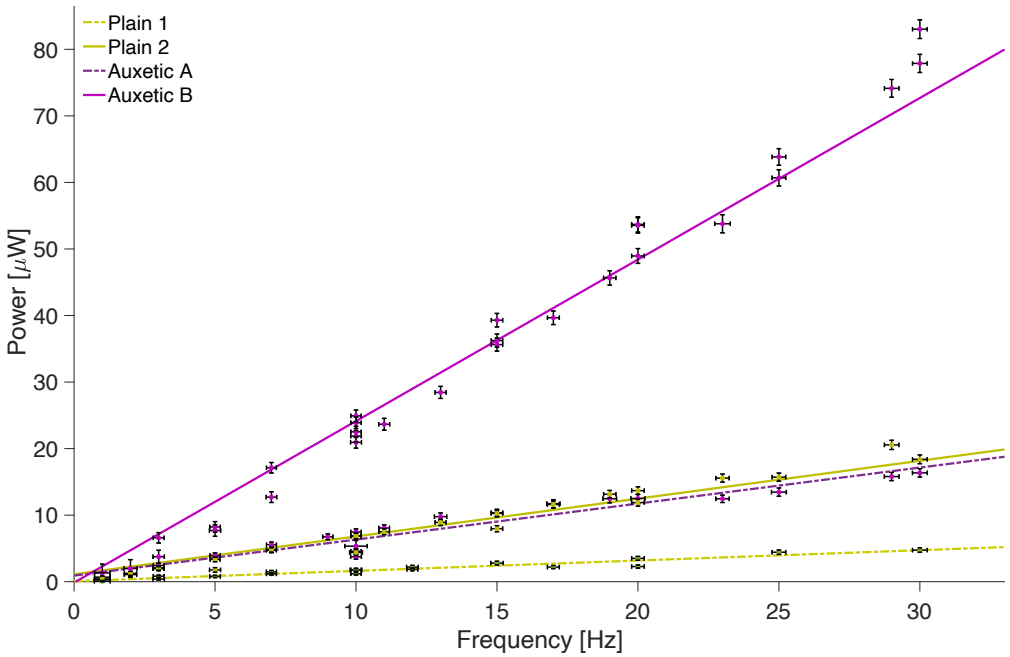

Figure 4-7: Results of power harvested from a range of input excitation frequencies on the LN samples, while maintaining a constant input amplitude of 250 με (10 μm).

4.1.4.3 LN Compared to PZT

The increased strength of the LN over PZT was significant. All LN samples could survive excitations up to 500 με (20 μm) without cracking. The plain LN sample required approximately the same force as the PZT one to apply this excitation (752 N vs. 730 N respectively), but while the auxetic PZT samples broke at an applied load of 230 N or less (at a smaller amplitude) the LN auxetic B sample endured ~415 N with no cracking. Tests at 250 με before and after the high amplitude sweep on the Auxetic B sample both produced a similar output: 20.9 & 22.5 μW respectively. This indicates that there was no internal damage to the LN layer, even at almost double the strain applied to the PZT versions.

Comparing the LN to the prior PZT results, the power output of LN was substantially lower; demonstrated in Figure 4-8. The voltage output from the LN was comparable or greater with that of the PZT, but the much higher load required for optimal power transfer greatly hindered the LN's output. The auxetic substrate was able to bring the LN over the plain PZT output, but the same substrate under a PZT layer delivers significantly more power. If the LN could be doped or mixed with other elements to increase its permittivity to nearer 1000 without compromising its strength, then it might be considered as a substitute for PZT. Alternatively, a sensor with an unusually high impedance it could be a suitable load for a LN-powered sensor node.

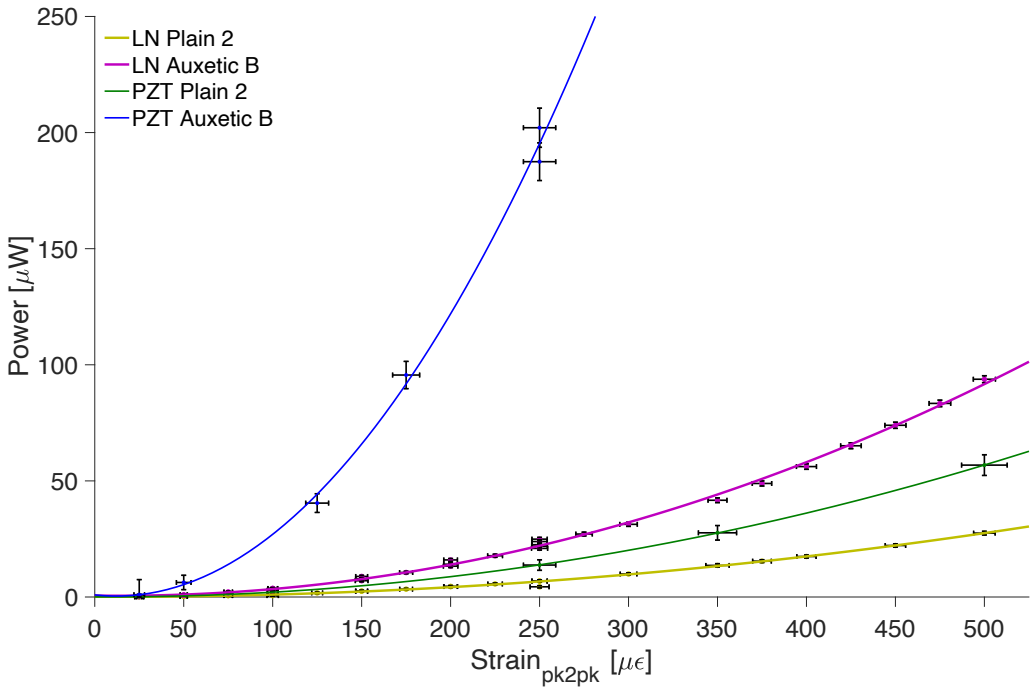

Figure 4-8: Comparison of results from LN and PZT. Power output against strain excitation amplitude at fixed frequency (10 Hz). Data from Figure 3-15 and Figure 4-6.

The gain brought on by the auxetic substrate was smaller for LN than that of the PZT (9.1-14.5 times), due to the greater strength of the LN layer. This increased stiffness makes it more difficult for the auxetic region to strain the LN. If the design process began with LN as the piezoelectric material, a different substrate design would likely be found to be optimal (probably one with thicker beams to provide a more authoritative structure).

4.2 Conclusion

Lithium Niobate demonstrated it was substantially stronger but produced significantly less power than PZT. All LN samples endured 500 με, but their power output was barely a tenth of the PZT's and the auxetic gain was only 3.6-4.2 times their plains'. The low output was due in large part to the MΩ resistances needed to achieve optimal power transfer. If the material could be doped or reformulated in such a way as to increase its permittivity without compromising its strength, then it would become a much more viable alternative to PZT which does not leech toxic substances. Bartasyte's group are continuing research into this material[82].

5 Simulated and Experimental Study of Auxetic Strain Energy Harvester

The proof of concept discussed in chapter 3 showed there is promise in the use of auxetic designs in energy harvesting, however the absolute power output was quite small. A larger piezoelectric layer would generate a more substantial output. This also allows a larger and more complex auxetic region beneath it than the previous single re-entrant unit. This chapter develops a re-entrant honeycomb array, again using finite element modelling to optimise the auxetic region's parameters. It also discusses the testing of MFC (Macro-Fibre Composite), a more flexible alternative piezoelectric material, and comparing it to PZT on both plain and auxetic substrates.

Section 5.1 describes how the new model operates, from the overall setup; through the processes of finding the best auxetic region through parametric sweep and subsequent optimisation, and the model results. The best design was manufactured and tested, as described in section 5.2. These experimental results are shown in section 5.2.3, including a comparison to the model results and a discussion on the preferable piezoelectric material. The chapter concludes with a summary in section 5.3.

5.1 Finite Element Model Designing

5.1.1 Model Setup

COMSOL Multiphysics® 5.3b was used to model the prospective designs, with the optimisation module to find the best design for the auxetic region. This model built on the previously validated proof of concept model, developed in chapter 3[1], but with the optimisation module that process was able to explore more of the design space more quickly. The larger overall dimensions (given in Table 5-1) allowed a more complex auxetic geometry to be used in the substrate. Figure 5-1 shows an exploded layout of the model.

To compare bulk ceramic PZT with MFC as the piezoelectric material, a standard size of MFC was selected (active area: 85×57 mm, with polyimide film protruding out to 103×60×0.3 mm overall[89]) which informed the size of the PZT

layer: 85×60×0.18 mm. The PZT thickness was continued from the proof of concept work, though it subsequently needed to be made thicker (0.55 mm) due to any supplier's ability to reliably manufacture and ship ceramic pieces of that large an area. For the work in this section, the PZT was still modelled as 0.18 mm; all model results from section 5.2.3 onwards use 0.55 mm. PZT thickness is shown in appendix C.I to have no significant effect on which auxetic designs operate best. Material properties used in these models are listed Table 5-2.

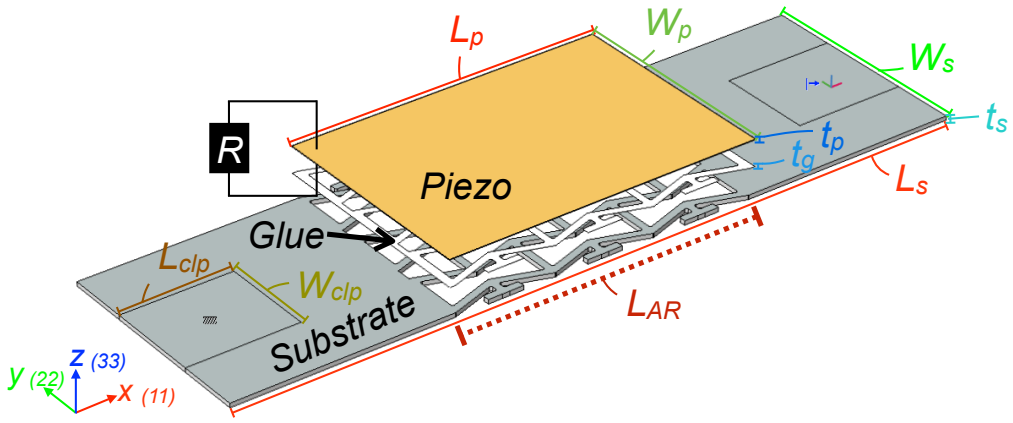

Figure 5-1: Exploded view of auxetic model dimensions, values in Table 5-1.

Table 5-1: Parameter values used in the COMSOL model.

Part	Parameter [unit]		Value
Piezo-Layer	Length [mm]	L_p	85
	Width [mm]	W_p	60
	Thickness [mm]	t_p	0.18† 0.3*
	Resistance [kΩ]	R	18.7 47.9*
Glue	Thickness [µm]	t_g	8
	TEL [GN/m³]	k_a	200
Substrate	Length [mm]	L_s	200
	Width [mm]	W_s	60
	Thickness [mm]	t_s	1.15
	Clamping region [mm]	L_{clp}	30‡
		W_{clp}	26

* Values for PZT | MFC respectively.
† During modelling phase; corrected to 0.55 mm in section 5.2.3.
‡ During modelling; corrected: 10 mm.

Table 5-2: Material properties used in the model. Piezoelectric values for PZT | MFC.

Material	Property [unit]		Value	
PZT/MFC	Density [kg/m³]	ρ_p	7600	5440
	Compliance	s_{11}^E	16.95	31.89
APC 855	Matrix	s_{22}^E	16.95	50.84
136	[µm²/N]	s_{33}^E	19.61	112.3
/		s_{44}^E	55.22	463.0
M8557-P2		s_{55}^E	55.22	413.2
88,89		s_{66}^E	43.72	188.3
		s_{12}^E	-4.910	-11.43
(Piezo-Layer)		s_{13}^E	-8.004	-13.45
		s_{23}^E	-8.004	-19.12
	Coupling	d_{31}	-276.0	-283.4
	Matrix	d_{32}	-276.0	-223.2
	[pC/N]	d_{33}	630.0	513.4
		d_{15}	720.0	560
	Relative	ε_{11}	3012	1950
	Permittivity	ε_{33}	3300	2544
Epoxy 3M DP 460 (Glue)	Density [kg/m³]	ρ_g	1250	
	Poisson's Ratio	v_g	0.35	
	Elastic Modulus [GPa]	E_g	1.00	
Steel: CS100HTP (Substrate)	Density [kg/m³]	ρ_s	7870	
	Poisson's Ratio	v_s	0.29	
	Elastic Modulus [GPa]	E_s	200	

The substrate's overall dimensions were then developed from this layer: 200×60×1.15 mm. These outer dimensions form its plain structure, used as the baseline for the auxetic region's optimisation. The substrate width is the same as the piezoelectric material, and its thickness derives from the prior work[1].

The model emulates how the harvester would be excited by the Instron under laboratory conditions. The clamping regions are areas of 30×26 mm (L_{clp}×W_{clp}) on the top and bottom surfaces in the middle of each end of the substrate; indicated by the black outlines in Figure 5-1. These large clamping regions were intended to provide a better grip to the substrate than the previous designs, however during testing it was found that a shorter clamping region worked better (by allowing a uniform strain across the substrate under the piezoelectric material[t]). In this section L_{clp} was 30 mm, while models in section 5.2.3 used 10 mm to match the experiment. At one end these faces were considered fixed. The opposite faces were excited by a harmonic prescribed tensile displacement (the maximum peak-to-peak amplitude). Throughout the design process, an excitation of 10 Hz and 28 μm peak-to-peak displacement (equivalent to 200 με on the free length of the substrate) was used as the expected maximum. A resistor was connected across the top and bottom surfaces of the piezoelectric layer; its load set to match the impedance of the layer, using Equation 3–1, for maximum power transfer. To reduce computation time, frequency domain analysis was used again; as demonstrated in appendix A.I.i, this is equivalent to a time-domain analysis.

The glue between the constituents was modelled with a layer of epoxy 8 μm thick. This continued the use of Thin Elastic Layers (TELs) as discussed in chapter 3[1]. This boundary condition modelled the imperfect adhesion at these interfaces. In section 3.2.4, k_a was found to be between 147 & 203 GN/m^3 to correctly emulate the experimental output. During the following design process, k_a was approximated to be 200 GN/m^3 for all plain and auxetic models. In precursor work, shown in appendix C.II, different k_a values were found to have a largely negligible effect on the relative output from different auxetic designs. The results of varying this parameter on the final model will be covered in section 5.2.3.

[t] This issue is rectified in chapter 6 by making the substrate 300 mm long with L_{clp} of 25 mm; see also appendix C.III.

Throughout the design stage the piezoelectric layer was only modelled as PZT. Considering it as MFC came after the optimisation, as appropriate homogenisation of the effective material properties of this composite remains somewhat contested[88]. The homogenised parameters from Kuang & Zhu[88] were selected due to them being derived specifically for energy harvesting purposes, and were experimentally validated using samples and an excitation method quite similar to the plain harvesters used in this work (see also appendix D.I).

5.1.2 Auxetic Region Optimisation Process

The central 82 mm (L_{AR}) of the substrate was given over to the auxetic region. This left a 1.5 mm buffer (L_{buf}) at either end to give the piezoelectric layer's ends a firm bond to the substrate. The re-entrant hexagon unit, from section 3.1[1], can be repeated to form a honeycomb array; such as the examples in Figure 5-2.

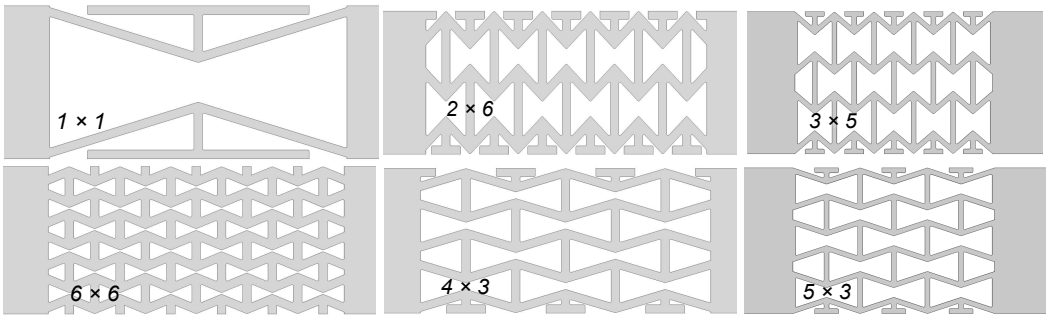

Figure 5-2: Some examples of M×N re-entrant honeycombs.

An annotated re-entrant unit is shown in Figure 5-3(a). Those units next to the edges are replaced by partial units, shown in Figure 5-3(b), with a crossbeam to aid in lateral strain transfer. Both base units were built as 2D parts in COMSOL. The model packs a whole number of re-entrant hexagon units into the auxetic region in both axes: *M* full units across the substrate (the y-direction in Figure 5-1), and *N* full units along the substrate (its x-direction)[u]. The units fitted together in the manner shown in Figure 5-4. Geometric parameters for the auxetic region are listed in Table 5-3, and its input control parameter values in Table 5-4.

[u] It would be possible to build a re-entrant honeycomb framework that is not restricted to integer values (easiest to implement by subtracting a regular array of bowtie shapes) but this makes the crossbeams neigh-impossible to implement in COMSOL and could lead to many broken off beams at the edges or lead the solid regions of the substrate to be weakly attached.

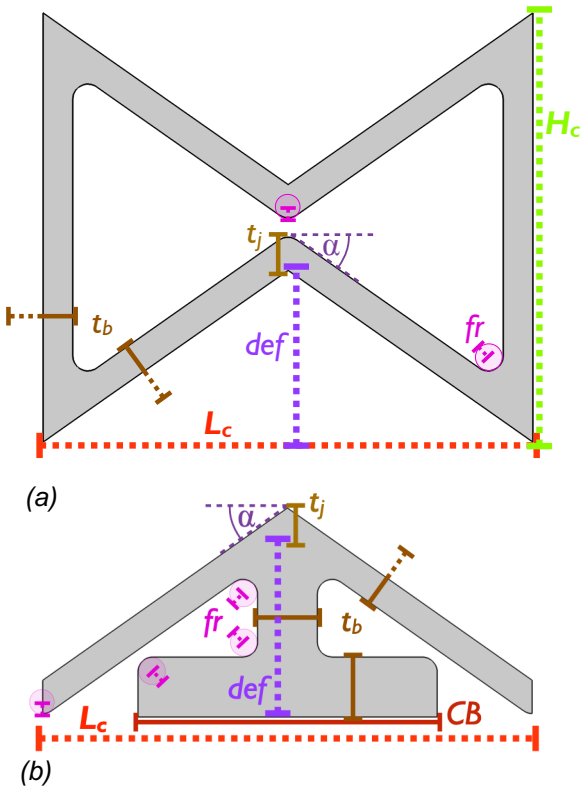

Figure 5-3: Parts for Re-Entrant Honeycomb Array (a) Hexagonal Unit and (b) Edge Unit. Parameters defined in Table 5-3 & Table 5-4. A full example array is shown in Figure 5-4.

Table 5-3: Auxetic region definitions with parametric variables emboldened, see Table 5-4.

Parameter [mm*]		Definition
Region Length	L_{AR}	82
Aux. Buffer	L_{buf}	1.5
Cell Length	L_c	$L_{AR}/\boldsymbol{N}$
Cell Angle [rad]	α	$tan^{-1}\frac{2\boldsymbol{d}(W_s-\boldsymbol{t_b})}{L_c(\boldsymbol{M}-\boldsymbol{d}(\boldsymbol{M}-1))}$
t_b Adjustment	t_j	$\boldsymbol{t_b}/(2\cos\alpha)$
Cell Height	H_c	$\frac{W_s-2tj}{\boldsymbol{M}-\boldsymbol{d}(\boldsymbol{M}-1)}$
Deformation	def	$\boldsymbol{d}\times H_c$
Crossbeam	CB	$\boldsymbol{t_b}+\boldsymbol{cb}\,L_c(1-\boldsymbol{t_b}/2def)$
Fillet Radius	fr	0.5

* Unless otherwise stated

Table 5-4: Range of input values for auxetic region, used during parametric sweep and optimisations.

Parameter [unit]		Swept Values	Opt. Range	
No. of cells in W_s	M	1, 2, 3, 4, 5, 6	[fixed]	
No. of cells in L_{AR}	N	1, 2, 3, 4, 5, 6	[fixed]	
Beam Width [mm]	tb	1, 2, 3	1	4.5
Deformation [%]	d	25, 30, 40	25	42
Crossbeam [%]	cb	0, 50, 75	40	88

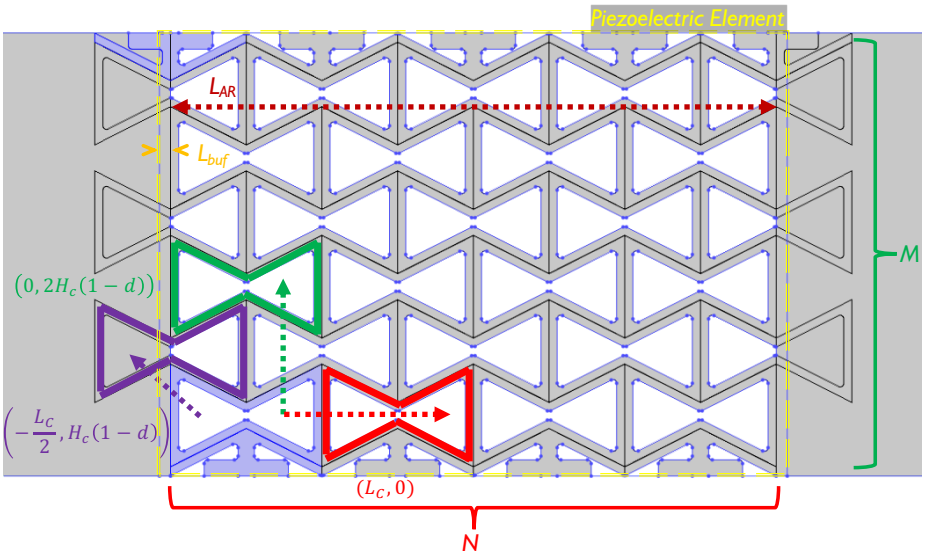

Figure 5-4: Example re-entrant honeycomb array before parts are united. Units placed manually are highlighted in blue with colour coded duplication of unit copies.

The first re-entrant unit and edge units were manually positioned on one end of the auxetic region. The re-entrant unit is then replicated into an interlocked column, stacked *M* units high. That column was then replicated *N* times along the length of the auxetic region to fill it. Sweeping through values of *N* was easy, but the construction of the initial column made sweeping *M* more difficult. There is a significant difference between odd and even values of *M*: if odd, the edge units mirror each other across the substrate; if even, these edges have an offset of half a unit length, which breaks the substrate symmetry; the examples shown in Figure 5-2 demonstrate this. The simplest solution was having six slight variations of the model geometry bundled behind a series of six '*if M==#*' statements (allowing a single parametric sweep to test all forms in one run). Each model would then proceed in the same way: replicating this column across, uniting the geometry, extruding the substrate and glue geometries, and adding the piezoelectric block on top.

The arrangement of these units was the first aspect to be optimised. COMSOL's optimisation module is not designed to handle a mixture of integer and floating parameters, so the first step was a parametric sweep of the combinations of values given in Table 5-4. This encompassed all 36 available *M*×*N* arrays; each array was then modelled with three different beam widths, t_b[v]; deformation fractions, *d*, and crossbeam ratios, *cb*. The filleting radius, *fr*, in all corners was 0.5 mm throughout, as it has no significant contribution to the output. This encompasses 972 variations of the auxetic honeycomb. A few produced geometric errors[w] (i.e. beam intersections) but most were viable options.

From the parametric sweep results, the viable arrays found to produce the most power, within stress limits, were taken as starting points for the optimisation module. The Nelder-Mead[137] method was chosen for this optimisation, as it can have arbitrary, non-differentiable, constraints; including a maximum stress limit in a component. This method first calculates a value for its objective function from the given initial parameters, then repeats for a few nearby points until it has one more result than free parameters. Each free parameter forms an axis in solution-

[v] Note that half of the beam width is found on each adjoining unit, as indicated in Figure 5-3.
[w] COMSOL could have skipped most of these invalid models using a parameter check before building the geometry to save processing time, see section 6.2.3.

space, and by having one additional point a simplex[x] is formed. The optimum within this region is estimated, and this point is tested. A new simplex is formed by replacing one point (typically the worst) with the latest one. If it is found to be worse than the current points, the next point may be outside the simplex (typically reflected from the worst point around the centroid of the remainders); thus the simplex iteratively walks around solution space seeking a suitable region to collapse into. Its final solution is found once the change from one optimum to the next is within a given tolerance (0.001 in this work) or a maximum number of iterations is reached. For every tested point, any breached constraint penalises its objective function result to steer the solution away.

A disadvantage of the Nelder-Mead method is that if the initial points cluster around a local maximum, then it may give that as its output[137]. With any non-differentiable method it is impossible to know whether one has found the global optimum, or merely a local optimum[137]. Repeating the optimisation from different starting points until a similar optimum design is reached multiple times was a good indication of having found the best parameters for a given array.

This method was used to find optimal values for beam thickness, deformation, and crossbeam length (allowable ranges listed in Table 5-4) for a given $M \times N$ array. If an optimised result was found at the limit of any range, that range was temporarily expanded and the optimisation repeated to ensure it was not artificially constraining the design. The objective function was to maximise the power output, while constraining the peak von Mises stress in the substrate and PZT within material limits (250 & 25 MPa respectively). Each array's optimisation was repeated from slightly different initial values to find a stable design.

5.1.3 Model Results

The results from the parametric sweep showed a few general tendencies. Removing the models that either failed to run, produced geometric errors, or had peak stresses over one of the material limits left 542 viable options. These are all shown in Figure 5-5, from which can be seen that most of the best models had between 4 and 6 units in each direction, while all the worst had 1 or 2 units in at

[x] A simplex is the simplest shape in *n*-dimensions; in 1D it's a line, in 2D a triangle, in 3D a tetrahedron, and in 4D it's a hyper-tetrahedron (a.k.a. 5-cell), etc.

least one direction. This suggests more small units have a greater authority over the piezoelectric layer than a few large ones, however the limited space in these smaller units require thinner beams which diminishes the output.

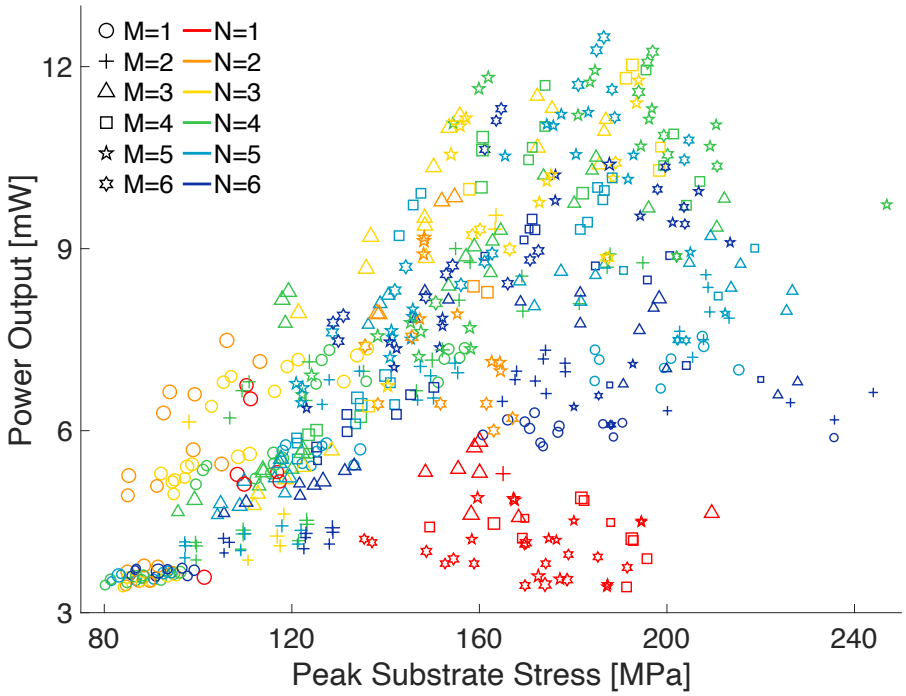

Figure 5-5: Parametric results of power output against peak stress in the substrate, with unviable designs filtered out. Marker shape indicates M value, and colour indicates N value, while its size indicates peak PZT stress.

The highest power results from the broad parametric sweep were picked out for further optimisation. As can be seen at the apex of the results in Figure 5-5, there are some duplicated *M*×*N* arrays which would be found within the same optimisation solution space, so only the highest power output forms are listed in Table 5-5; followed by their optimised versions.

Table 5-5: Best parametric sweep results, in descending order of parametric power output. These designs were optimised to achieve the final values. Chosen design emboldened, and depicted in Figure 5-6.

Parametric Input Values & Results								*Optimised Parameters & Results*					
M	*N*	t_b *[mm]*	*d [%]*	*cb [%]*	*Power [mW]*	*Peak Stress [MPa] Substrate*	*Piezo*	t_b *[mm]*	*d [%]*	*cb [%]*	*Power [mW]*	*Peak Stress [MPa] Substrate*	*Piezo*
6	5	2	40	75	12.48	186.5	23.1	2.0	41.0	81.2	12.50	149.7	22.0
6	4	2	30	75	12.25	197.0	23.0	**2.2**	**37.5**	**77.5**	**13.29**	**165.2**	**23.9**
4	3	3	30	75	12.03	192.6	24.7	3.3	39.4	79.0	13.12	158.9	~~26.5~~*
4	4	3	40	75	11.95	195.5	23.2	3.0	40.4	76.8	11.85	178.1	23.9

**Repeatedly did not converge to a design within this stress limit[y].*

[y] The issue may have been a failure to normalise all parameters and limits to ~1; the order of magnitude difference in the substrate and piezoelectric layers' peak stresses reduced the weight of the latter limit within the algorithm. This has been corrected in chapter 6.

The greatest power output after optimisation was found from the 6×4 design shown in Figure 5-6: 13.29 mW. This corresponds to a gain of 12.5 times the plain output of 1.06 mW. The optimised parameters for this auxetic region are therefore: M = 6, N = 4, t_b = 2.2 mm, d = 37.5%, cb = 77.5%.

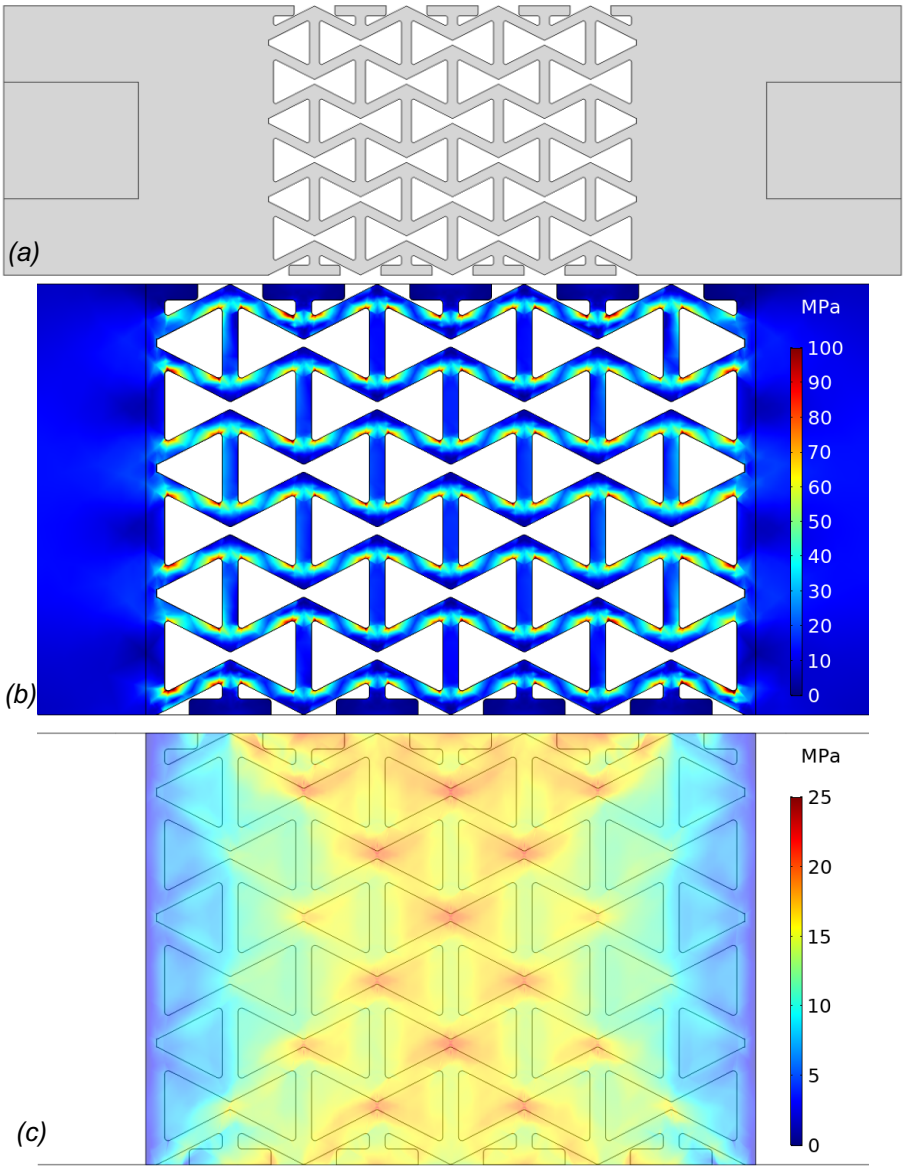

Figure 5-6: Optimised 6×4 auxetic substrate design: (a) overall (with clamping regions indicated); and stress distribution in (b) auxetic substrate region and (c) PZT.

When the piezoelectric layer was modelled as MFC instead of PZT, the power output for the plain was found to be 1.48 mW, while the auxetic model outputs 7.25 mW; a gain of 4.89 times. The stress distribution in the MFC was almost identical to that of the PZT (shown in Figure 5-6(c)) but all stresses were around half as high.

5.2 Experimental Study

5.2.1 Manufacturing

One each of the plain PZT, auxetic PZT, plain MFC and auxetic MFC harvesters, shown in Figure 5-7, were manufactured for experimental comparison in a similar manner to the previous samples. Both piezoelectric materials were too expensive to make duplicates. The substrates were all laser cut from stainless spring steel: CS100HTP (chosen for its high tensile strength and corrosion resistance). The piezoelectric layer was bonded to the substrate with epoxy: 3M Scotch-Weld™ DP 460[134]. This was clamped in a vice between two flat boards for over 24 hours at room temperature to allow the epoxy to cure. Output wires were soldered to the electrode surfaces of the PZT, where accessible (for the plain PZT sample, the connection was though the reverse side of the substrate). MFC has exposed terminals connected to its encapsulated electrodes.

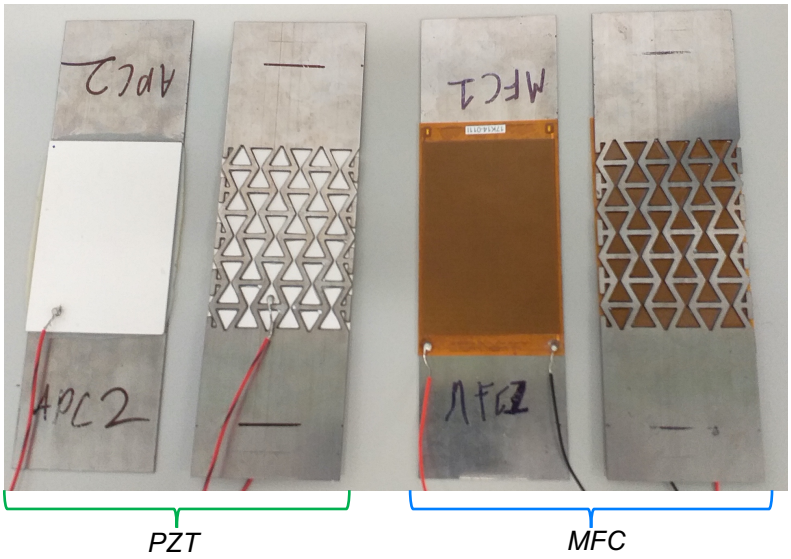

Figure 5-7: Annotated photograph of the four harvester samples. Auxetic samples upside-down to show substrate design.

5.2.2 Testing

Each harvester was tested by straining it with a sinusoidal excitation and measuring its output voltage, as before. Each sample was first clamped into the Instron ElectroPlus E10000, which applies the exciting strain onto the harvester at the given amplitude and frequency for 200 s. There is a pre-test extension of

1 μm more than its amplitude, to ensure the harvester remains in tension. The sample relaxes to its starting position between tests.

To measure the voltage, the output wires were connected to a NI-2992 interface. Its internal residence (1 MΩ) was in parallel with a resistor array controlled by the Agilent U2751A Switch Matrix relay (discussed in section 4.1.2). Every 5 s this automatically stepped through one of 32 resistances in the 1-945 kΩ range. From the measured voltage at each load, the accumulated energy was calculated, then the cycle's power output was calculated (as described in section 4.1.3). The optimum output and load resistance was found for a range of excitations, and for each sample.

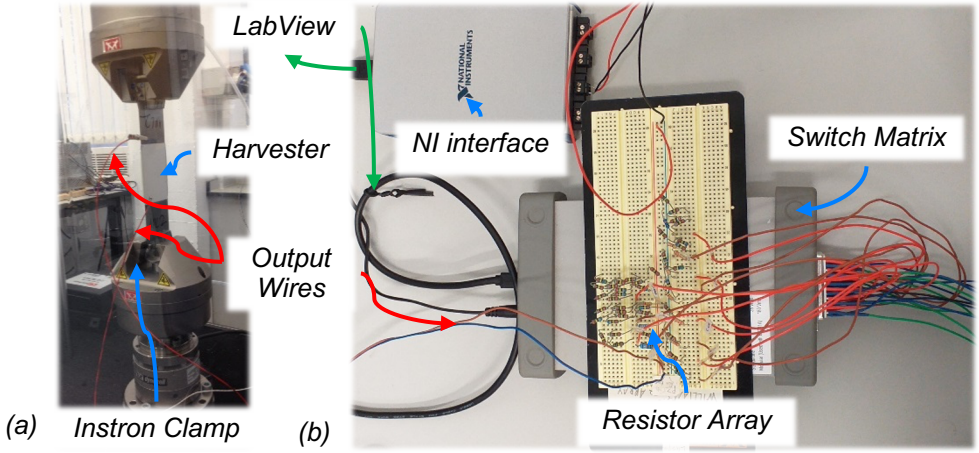

Figure 5-8: Annotated Photographs of (a) Plain PZT sample in Instron, and (b) Switch Matrix and resistor relay, with NI LabView interface.

After some initial testing, it was found the clamping length was too large, and more power could be obtained with a shorter L_{clp}. This was attributed to the strain being non-uniform by the time it reached the piezoelectric layer. By having at least three times the clamping length of free substrate before the piezoelectric layer, this effect was minimised, see also appendix C.III.

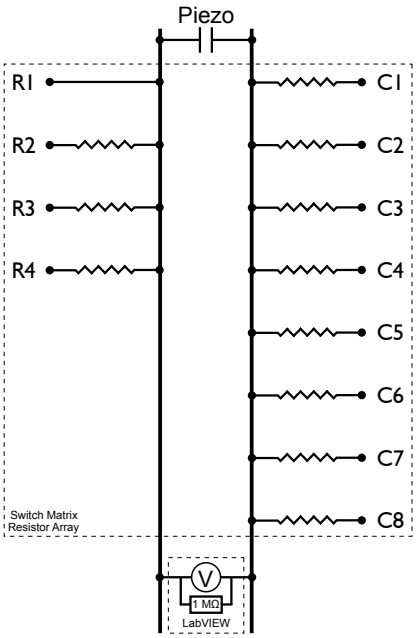

Figure 5-9: Diagram of Switch Matrix circuit. For measurements, an R node is joined to a C node to provide the load on the excited piezoelectric material.

Table 5-6: Resistance values for Row and Column nodes, shown in Figure 5-9. Total resistance is R(i)+C(j).

Row | Column Node	*Resistance [kΩ]*
R1	*0*
R2	*100.1*
R3	*411.5*
R4	*845*
C1	*1.000*
C2	*10.00*
C3	*21.88*
C4	*32.89*
C5	*50.94*
C6	*67.1*
C7	*79.1*
C8	*99.9*

5.2.3 Results & Discussion

Figure 5-10 shows the power output of all four samples under the same excitation (10 Hz, 18 μm (100 με) peak-to-peak). It demonstrates that the auxetic substrate delivers a dramatic improvement for both piezoelectric materials. All results at their optimal loads are listed in Table 5-7 (note that the theoretical optimum loads are 57.01 and 47.86 kΩ for the PZT and MFC respectively). These results show that the PZT generated more power than the MFC in both cases (in part due to the MFC's lesser volume of piezoelectric material), but that the gain for the MFC was almost double that for the PZT (due to the greater flexibility of the MFC compared to the PZT, which gave the auxetic substrate more authority).

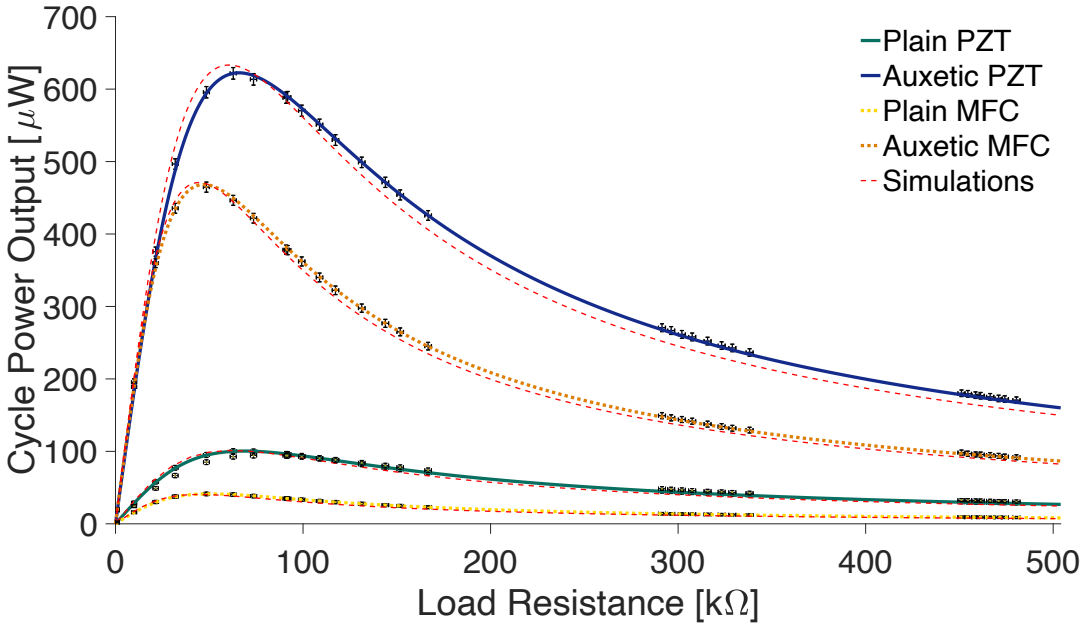

Figure 5-10: All harvesters' output when subjected to the same excitation (100 με peak-to-peak at 10 Hz using the resistance sweep); with appropriate model simulations.

Table 5-7: Optimum results from Figure 5-10, with fitted TEL spring constant, k_a.

Harvester	*R_{Opt} [kΩ]*	*P_{Opt} [μW]*	*Gain*	*k_a [GN/m³]*
Plain PZT	*68.6*	*100.4*	*–*	*35.7*
Auxetic PZT	*65.9*	*622.5*	*6.2*	*41.8*
Plain MFC	*50.5*	*41.3*	*–*	*13.5*
Auxetic MFC	*47.1*	*468.2*	*11.3*	*23.8*

The imperfect adhesion of the epoxy required a revision of the k_a value in the model's TELs. Before experimental testing, the value of 200 GN/m^3 for the TELs spring constant, k_a, was assumed. To fit a revised value to the experimental results, the models were updated with the correct clamping length (10 mm) and thickness for the PZT (0.55 mm), and simulated across a range of k_a values at the 10 Hz, 100 με excitation; as shown in Figure 5-11. In the region found to be of interest (1-75 GN/m^3) power is approximately linear with k_a. These four fitting formulae are listed in equations 5–1-4; where all P are in units of μW and k_a in units of GN/m^3. These allowed the determination of an appropriate k_a value to emulate the bonding quality of the harvesters from their power outputs.

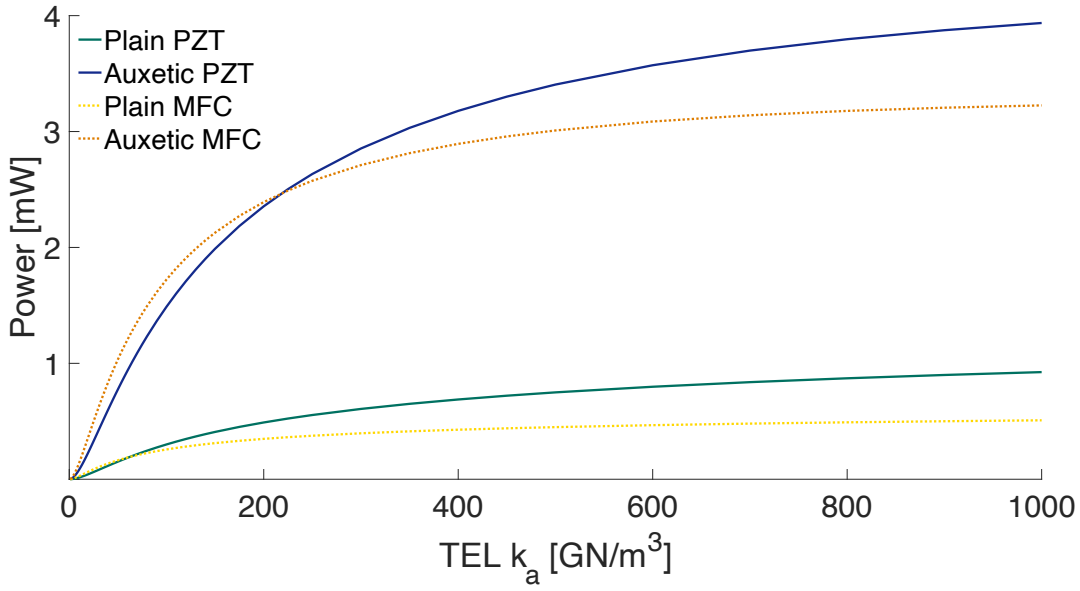

Figure 5-11: Simulated power output of plain and auxetic harvesters against spring constant per unit area, k_a, in the Thin Elastic Layers (TELs); to be used to compare to experimental output under the same excitation: 100 με at 10 Hz.

$$P_{Plain\ PZT} = 3.3531\ k_a - 19.433\ ; \qquad R^2 = 0.9984 \qquad \text{Eq.5–1}$$

$$P_{Auxetic\ PZT} = 17.333\ k_a - 101.30\ ; \qquad R^2 = 0.9994 \qquad \text{Eq.5–2}$$

$$P_{Plain\ MFC} = 3.6191\ k_a - 7.5591\ ; \qquad R^2 = 0.9961 \qquad \text{Eq.5–3}$$

$$P_{Auxetic\ MFC} = 24.139\ k_a - 106.94\ ; \qquad R^2 = 0.9999 \qquad \text{Eq.5–4}$$

These fitted k_a values are listed in Table 5-7, and are all much lower than the proof of concept PZT harvesters shown in chapter 3[1]. Previously, k_a was in the range of 147-203 GN/m^3. The difference was at least partly due having stainless steel as the substrate. It was much smoother than the former mild steel, and thus has a weaker bonding adhesion to the epoxy in each case. The values are similar for these four harvesters, though lower for both MFC harvesters due to its polyimide encapsulation having a lower surface roughness than the PZT's sputtered electrode for epoxy to bond to. It is also likely that the adhesion loss to carbon fibre was already factored into the material parameters by Kuang & Zhu[88].

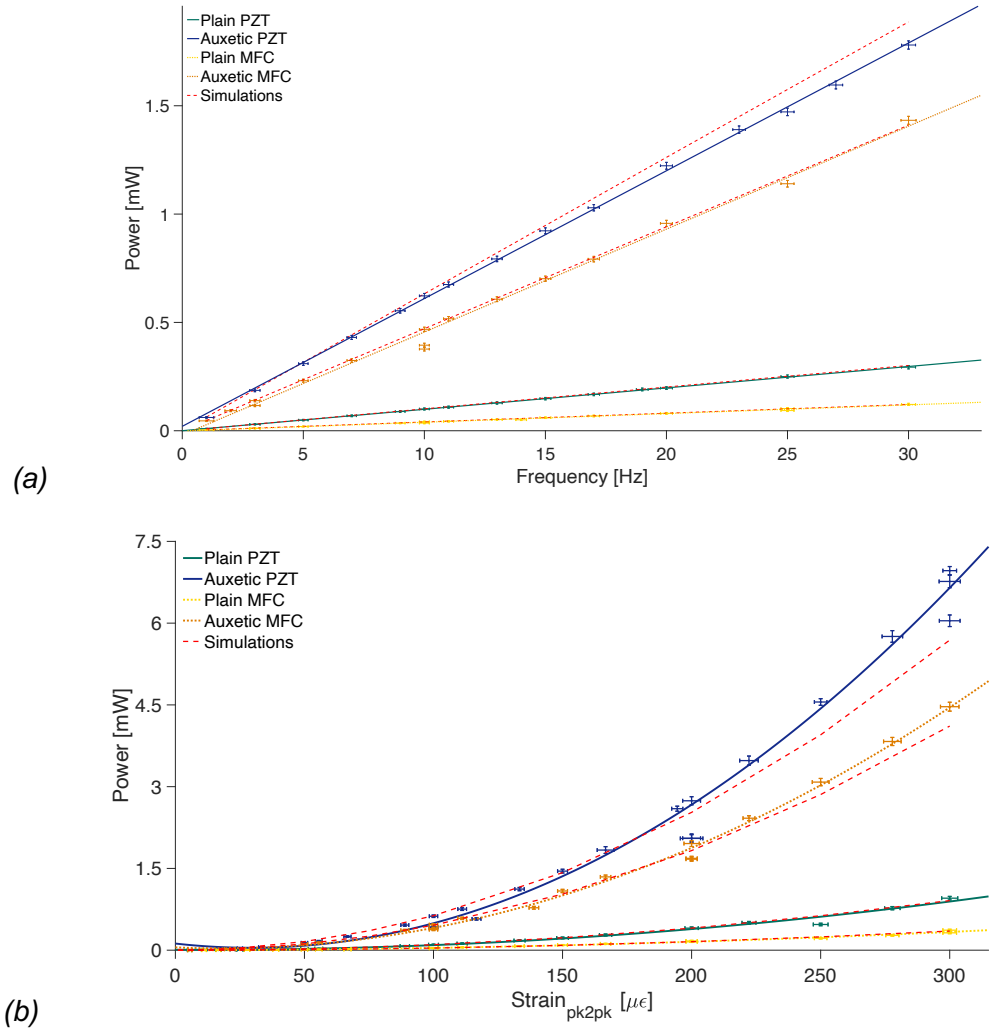

Figure 5-12: Results of all harvesters subjected to a range of input excitations: (a) Frequency sweep at 100 με; (b) Amplitude sweep at 10 Hz.

Figure 5-12 shows the optimum outputs from all harvesters under a range of excitations. The model outputs also shown maintain the revised displacement and k_a values found previously; demonstrating that the same k_a value applies to any excitation, as before[1]. All outputs were approximately linear with frequency and quadratic with strain amplitude for all harvesters, and the gain factors between the auxetic and plain versions are constant in both sweeps.

This chapter has shown that strain can be concentrated into piezoelectric transducers using auxetic designs to deliver usable power outputs. These kinds of harvester could provide a better power source for structural health monitoring devices or some IoT technologies. Though the MFC produced less power overall than the ceramic PZT, the auxetic substrate achieved higher gain. There is scope for an further improvement with MFC, since the substrate design was constrained by the breaking point of the ceramic and MFC is more resilient in this regard.

5.3 Conclusion

In this chapter, using an auxetic substrate has been shown to dramatically increase the power output of a piezoelectric strain energy harvester. Using ceramic PZT as the piezoelectric material, 6.2 times the power output from the same excitation was achieved (622.5 vs. 11.4 μW at 10 Hz, 100 με). With MFC as the active material the gain was 11.8 times (468.2 vs. 41.3 μW at 10 Hz, 100 με), due to its greater flexibility; though its absolute power output was still lower than the PZT under the same conditions. These gain factors are a function of the expanded re-entrant honeycomb geometry and chosen piezoelectric material, and were constant for any of our excitations. These auxetic designs could be applied to harvesting from low-strain environments, such as within infrastructure.

6 Simulated and Experimental Study into Other Auxetic Harvester Designs

Following the successful larger scale re-entrant honeycomb harvester described in chapter 5, the scope expanded into other auxetic structures[z]. This chapter discusses the testing and optimisation simulations for a revised re-entrant honeycomb, along with elliptical slits forming rotating triangle, parallelogram, and hexagram arrangements, and I-hole based structures. The five best auxetic designs were taken forward to the experimental stage to compare them empirically.

This chapter begins with establishing a value for k_a on a plain substrate, in section 6.1. This was taken into modelling the listed range of auxetic designs, in section 6.2. Section 6.3 covers the experimental procedure (which remained very similar to that of the prior chapter), with the results and their discussion in section 6.3.2. Final conclusions are drawn in section 6.4.

6.1 Plain Redux

The previous uncertainty in an appropriate value for modelling the bonding adhesion made some of the previous auxetic design work somewhat speculative. It would have been better to test a plain version of the substrate first, and use that to find an appropriate k_a (bonding stiffness per unit area) value for their TELs (thin elastic layers) to model the adhesion for the auxetic designs. This was done prior to the final phase of the auxetic design work. This also allowed a comparison of substrate materials: aluminium against the prior stainless steel.

The substrates used in chapter 5 were 200 mm long. For a rectangular specimen, the distance from the tip of the clamp to where the stress is uniform across the sample is generally around three times the clamping length; see also appendix C.III. Ideally the strain should be uniform by the point it reached the piezoelectric material. Previously this would mean a clamping depth of up to

[z] The basis of these designs were among the preliminary models (before the necessity for the TELs, among other factors, were known). This chapter describes a more rigorous analysis on these designs, incorporating modelling techniques discussed in prior chapters.

13 mm at each end, which wasn't ideal for gripping. To fix this in these final versions, the substrates were 300 mm long, with clamping areas of 25×26 mm.

MFC was used as the piezoelectric material, though for this subsection using pieces that are only 85×30×0.3 mm due to cost. These maintain the same length but only half the width to save on cost (it also allowed a comparison to a carbon fibre substrate previously investigated in Zhu's group[44,56,88,138]; see appendix D.I, though their carbon fibre was too brittle for auxetic designs). The MFC, CS100HTP steel, and epoxy material parameters used were the same as in the previous chapter; listed in Table 5-2. For aluminium 1050 the material parameters were: ρ_{Al} = 2700 kg/m^3, ν_{Al} = 0.33, and E_{Al} = 70 GPa. The model layout is shown in Figure 6-1, with the experimental samples in Figure 6-2. Due to the available stock, the steel was 1.15 mm thick, while the aluminium was 0.9 mm thick; this was taken into account for the models accompanying the experimental results in Figure 6-3, and those of Figure 6-4. Experimental testing and data analysis was conducted in the same manner as described in section 5.2.2.

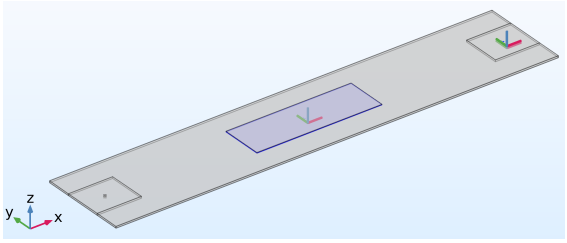

Figure 6-1: COMSOL setup of 300 mm plain substrates with narrow MFC in blue.

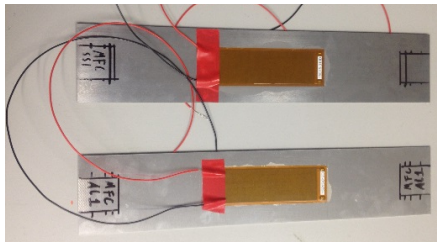

Figure 6-2: Photograph of steel (top) and aluminium samples.

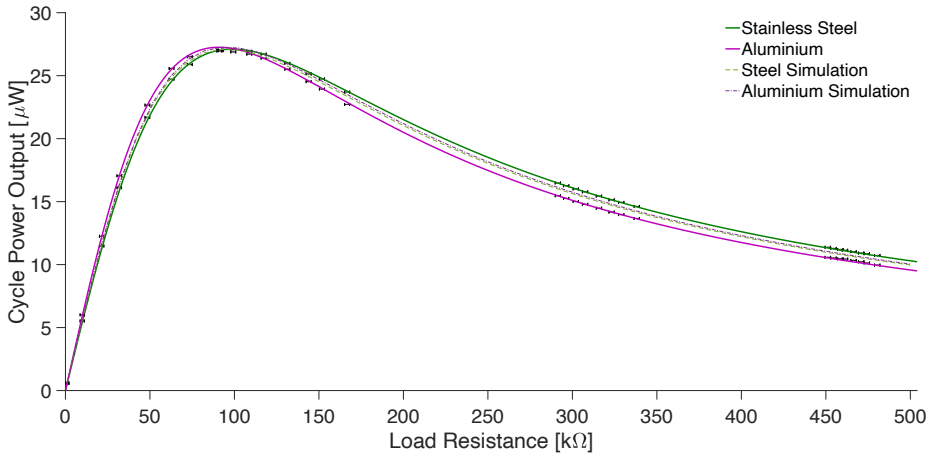

Figure 6-3: Experimental results for plain samples under a 10 Hz, 100 με (25 μm) excitation, with simulations using appropriate k_a values.

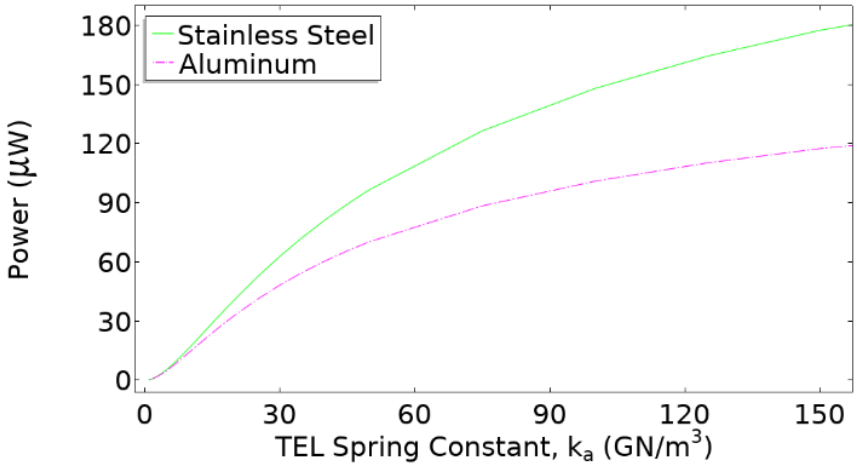

Figure 6-4: Simulations of both plain substrate materials over a range of k_a values.

From the results in Figure 6-3, there was little difference in output between the two materials as substrate. During the testing the aluminium sample was pockmarked by the teeth of the clamps more noticeably than the stainless steel was, indicating a better grip. It was also much lighter than the steel, which would be an advantage in many commercial applications. Using Figure 6-4, appropriate values of k_a to emulate these samples were found. For the steel this was 14.3 GN/m^3 (similar to the plain MFC value found in Table 5-7), and for the aluminium it was 16.5 GN/m^3. These values indicate that the epoxy's bonding to the aluminium is slightly stronger than to the steel.

Based on these results aluminium was selected for the substrate material and modelling throughout the following section will use this k_a value of 16.5 GN/m^3 for the spring constant in all TELs, until otherwise stated.

6.2 Auxetic Region Simulations and Results

6.2.1 Model Commonalities

For all the following models, there were many design constraints in common, only the design within the auxetic region of the substrate was different. The model was built from an aluminium substrate (300×60×0.9 [aa] mm), MFC as the piezoelectric layer (85×60×0.3 mm), and epoxy as the bonding agent (8 µm thick). The excitation was the same 10 Hz, 200 µε extension throughout (as an upper strain limit) analysed in the frequency domain. This was applied using the same

[aa] This thickness would later become 1.5 mm, the thinnest available in the required grade.

clamping setup as the prior plain structure. Early in the design process it was found that the yield of the original aluminium 1050 (~100 MPa) was too low and would restrict the designs, so the alloy 6082 T6 replaced it; for modelling purposes this had the same material parameters as the original aluminium but a yield of ~250 MPa. The stress limits were then 200 MPa in the substrate, and 17.5 MPa in MFC. This MFC limit was set conservatively low, as the assumptions made to homogenise the composite material may fail to account for any localised peak stress in its fibres. All parameters and limits were scaled to keep values seen by the optimiser in a similar order of magnitude; preventing undue weighting. The baseline model for all designs was a plain harvester with full size piece of MFC: under the same excitation, its output was 162 μW.

6.2.2 For Re-Entrant Honeycomb Array Redux

With the substrate now longer, made from aluminium, and the stress field more uniform, the design optimisation of the re-entrant honeycomb array was repeated. The model construction was largely identical to that described in section 5.1, except that the range of possibilities was expanded by allowing *M* & *N* to take integer values up to 7, as exemplified in Figure 6-5; which gave 49 variations on the re-entrant honeycomb. The parametric sweep values are listed in Table 6-1, with these results shown in Figure 6-6. The best results (i.e. highest power without exceeding stress limits) from the parametric sweep became starting points for the optimiser, as before. The best parametric results are listed in Table 6-2, alongside the optimised version of that *M*×*N* array.

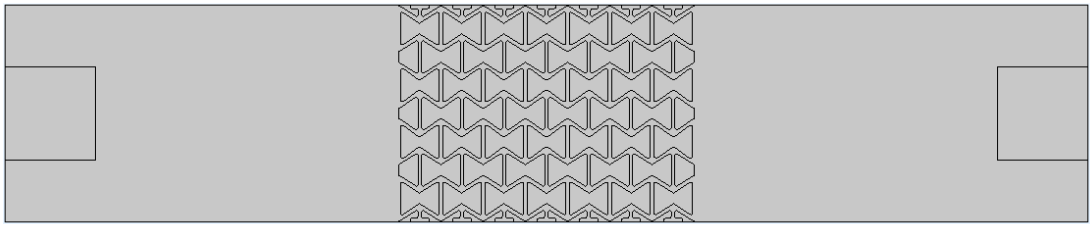

Figure 6-5: An example 7×7 re-entrant honeycomb substrate design.

Table 6-1: Re-entrant honeycomb inputs for parametric sweep and optimisations.

Parameter		*Swept Values*	*Opt. Range*	*Units*
No. of cells in W_s	*M*	*1, 2, 3, 4, 5, 6, 7*	*[fixed]*	*–*
No. of cells in L_{AR}	*N*	*1, 2, 3, 4, 5, 6,7*	*[fixed]*	*–*
Beam Width	*t_b*	*0.7, 1, 2, 3*	*1–4.5*	*mm*
Deformation	*d*	*25, 33, 40*	*25–42*	*%*
Crossbeam	*cb*	*0, 50, 75*	*40–88*	*%*

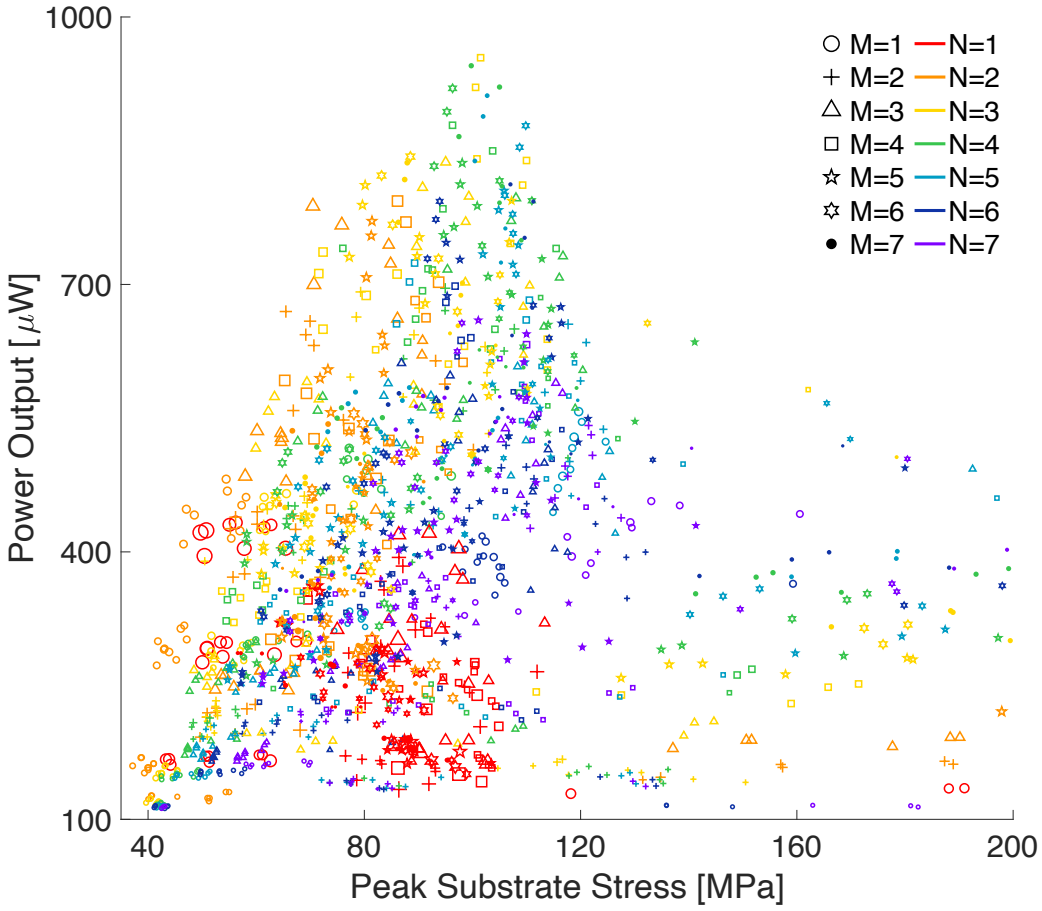

Figure 6-6: Distribution of re-entrant honeycomb parametric results, with overstressed and unviable models filtered out. Marker size indicates peak MFC stress.

Table 6-2: Best re-entrant honeycomb parametric sweep results, in descending order of parametric output, and the optimised designs found from them. Final design emboldened, and depicted in Figure 6-7

Sweep Input Values					*Sweep Results*			*Optimised Parameters & Results*					
M	*N*	t_b *[mm]*	*d [%]*	*cb [%]*	*Power [μW]*	*Peak Stress [MPa] Substrate*	*Piezo*	t_b *[mm]*	*d [%]*	*cb [%]*	*Power [μW]*	*Peak Stress [MPa] Substrate*	*Piezo*
4	*3*	*3*	*40*	*75*	*954*	*102*	*7.5*	***3.118***	***40.98***	***81.69***	***986***	***102***	***7.7***
7	*4*	*2*	*40*	*75*	*945*	*100*	*6.5*	*2.108*	*40.64*	*82.02*	*974*	*102*	*6.6*
6	*4*	*2*	*40*	*75*	*920*	*96*	*6.7*	*2.213*	*41.16*	*82.91*	*973*	*96*	*6.7*
7	*5*	*2*	*40*	*75*	*912*	*103*	*5.9*	*1.835*	*41.45*	*82.81*	*933*	*97*	*6.2*
4	*4*	*3*	*40*	*75*	*879*	*96*	*6.7*	*2.824*	*40.95*	*79.06*	*898*	*109*	*6.7*
6	*5*	*2*	*40*	*75*	*878*	*110*	*6.0*	*1.940*	*41.70*	*82.44*	*901*	*103*	*6.2*
6	*3*	*2*	*40*	*75*	*843*	*89*	*7.8*	*2.422*	*40.88*	*84.88*	*939*	*96*	*7.6*

Some general tendencies can be extracted from these results. The chaotic appearance of Figure 6-6 demonstrates the power output is too unpredictable to be calculated by analytic equations, and that the finite element models are necessary. The top parametric results show similar trends to those previously discussed in section 5.1.3, with some of the best designs being almost identical to those found in Table 5-5. Comparing Figure 6-6 and Figure 5-5 there is a similar overall spread of results rising from the origin up to the upper right, and

familiar clustering of many the N=1 results in the lower left of this main spread in both cases. Due to the different materials, these new results are shifted leftwards to lower stresses (allowing more of the scattered high stress results to be seen within the substrate's stress limit) and slightly downwards due to the reduced output of MFC compared to PZT. The newly included $N = 7$ designs were generally on the lower flanks of the main spread, while some $M = 7$ arrays were found amongst the apex designs; indicating that narrower re-entrant units don't stretch the MFC as effectively as a tall column of stacked units. Designs with fewer re-entrant units tended to fare poorly against designs with more, but thicker beams (with more authority over the MFC) could overcome this disadvantage. All the best parametric results listed in Table 6-2 come from the most re-entrant form of that array (40%) with the maximum available crossbeam (75%). These results omit some designs with different values for t_b, d, or cb accompanying one of the already listed $M \times N$ arrays (as these gave a lesser power output than this version and would be found within the range of the same optimisation); these were often used as an alternative starting point to find a stable maximum.

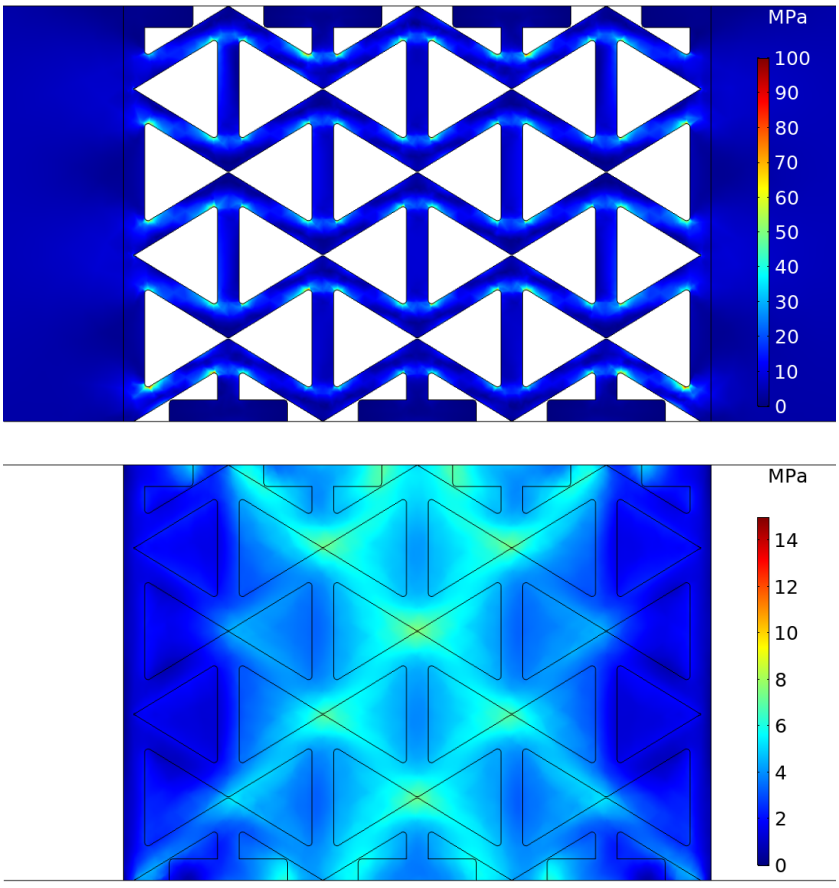

Figure 6-7: Selected optimal 4×3 re-entrant honeycomb design, shown as stress maps of the auxetic region of the substrate (upper) and piezoelectric layer (lower).

The best optimised design came from the 4×3 array, depicted in Figure 6-7. Its model output of 986 μW is a gain of 6.08 times the plain baseline. It was a small improvement over its parametric starting point; some other listed designs improved by a greater margin through their optimisations, and so it is possible, if unlikely, that an even more exhaustive search could find a still better design. The main improvements over the parametric starting point appear to be pushing the re-entrancy and crossbeam to their respective limits, with the beams almost touching; the tips are ~0.4 mm apart, which proved more difficult to manufacture.

This gain factor is much lower than that found experimentally in section 5.2.3 (11.3 times its plain equivalent), however in that case there was a difference in their corresponding k_a values (plain: 13.5 vs. auxetic: 23.8 GN/m^3). The expected outputs for those MFC models calculated with equations 5–3 & 4 using each of these k_a values find a gain of 6.6 or 5.3 respectively; in line with this new factor.

6.2.3 For Rotating Parallelograms

Rotating squares are a widely researched auxetic structure[104,105,107,108,112,139–142]. This design can easily be made by cutting elliptical slits in a sheet, leaving squares connected at their corners, as shown in Figure 6-8(a); forming hinges of a sort. These solid regions are connected in such a way that under tension they will preferentially rotate; this pushes their corners outward and opens the slits up, leading to their auxetic behaviour[107,108,141]. By altering the relative lengths and angles between slits, arrays of rectangles, rhombuses, or rhomboids can be created; these shapes are collectively called parallelograms, and are all exemplified in Figure 6-8. As these designs share a similar construction, it was possible to process all of them in the same COMSOL model.

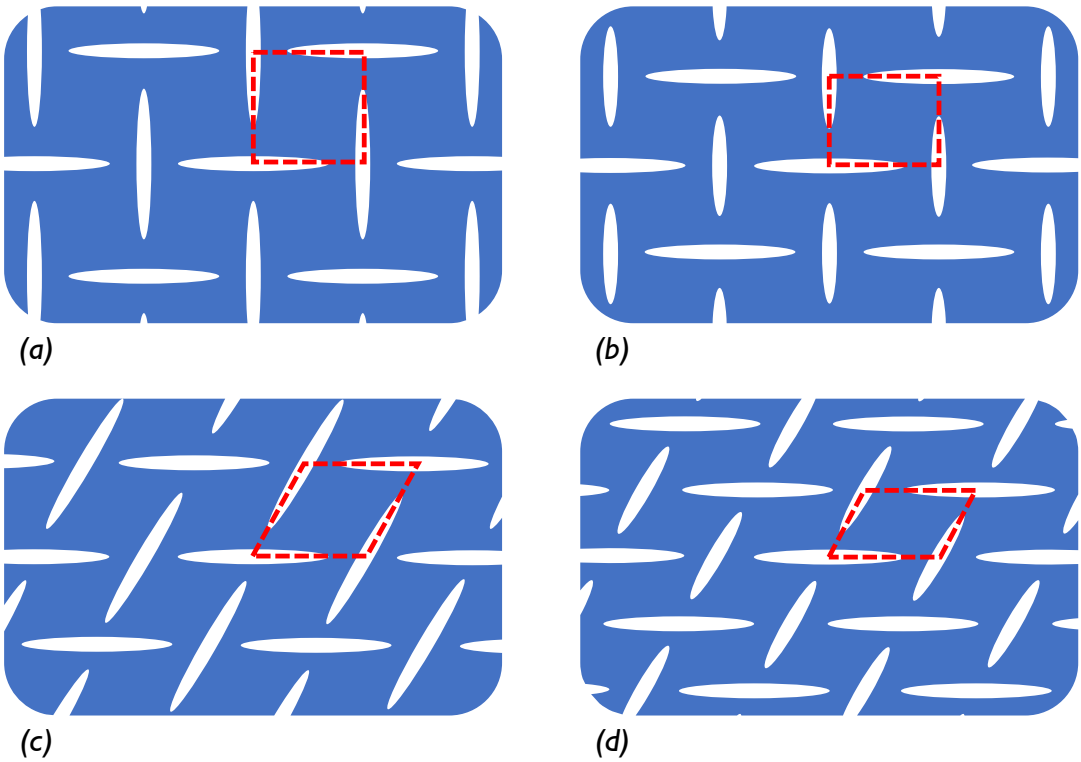

Figure 6-8: Diagrammatic rotating (a) square, (b) rectangle, (c) rhombus, and (d) rhomboid arrangements; collectively dubbed rotating parallelograms.

This rotating parallelogram model has six controllable parameters, depicted in Figure 6-9: h_A, the length of the baseline slits (controlled by the semimajor axis length of the baseline elliptical holes); h_b, the width of the slits (i.e. the semiminor axis length of all ellipses); r, the ratio of crossing slit length to the base slit length (for squares and rhombuses this is 1; less otherwise); R, the ratio of base slit length to grid spacing length (i.e. the distance between slit centres); θ, the angle between crossing gridlines (for squares and rectangles this is 90˚; less otherwise); and φ, the angle between the entire grid (parallel to the baseline slits) and the x-axis of the substrate (note, $\varphi = 0^\circ$ for all examples in Figure 6-8). Values in the parametric sweep for all of these are listed in Table 6-3. This design was built from the slit centred in the middle of the auxetic region outwards; this cut down the number of processed models through symmetry. To filter out impractical models, there were two checks before processing each design: before building the model, an estimate of the distance between nearest neighbouring slits ensured there was enough material there to sustain a load[bb]; after building the geometry there was a domain check to ensure the substrate had not been split

[bb] Parameter Check: $h_a R - h_a - h_A\, h_b / \sqrt{(h_A \sin(\theta))^2 + (h_b \cos(\theta))^2} < 0.5$ mm; break if true.

into multiple pieces. If a design failed one of these checks, the sweep or optimiser skipped processing it and built the next design. These checks filtered out most unviable designs, which were otherwise likely to cause the computer to crash or merely take the longest to process while contributing nothing of use.

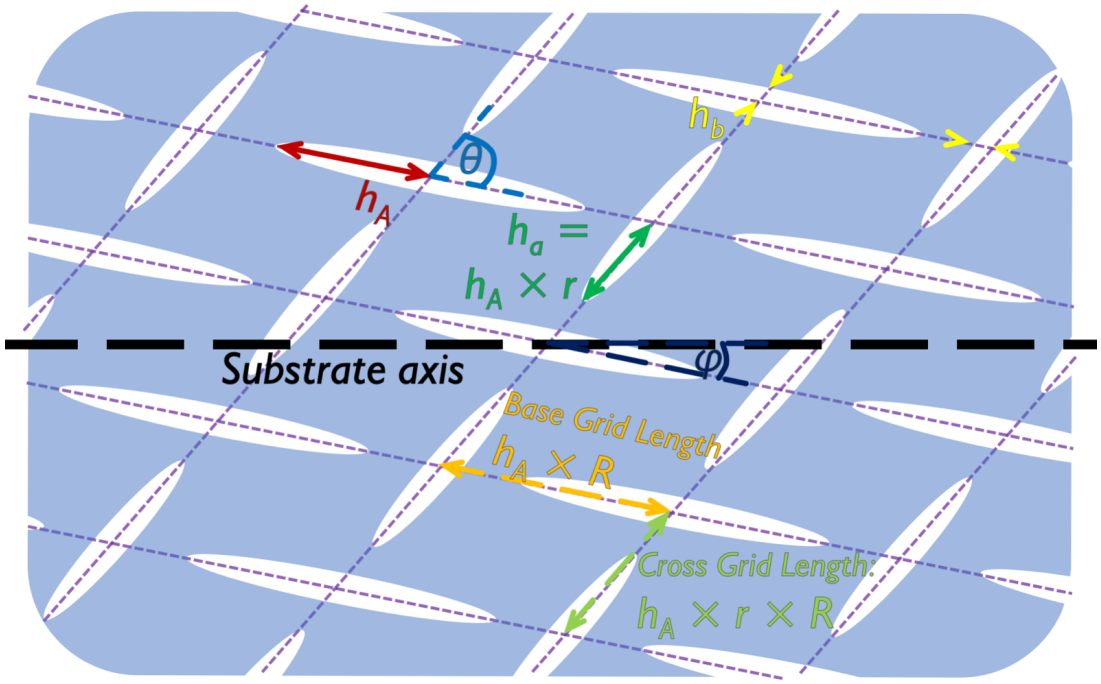

Figure 6-9: Diagram showing parallelogram model parameters: h_A, baseline semimajor axis; r, crossing axis ratio; h_b, all semiminor axes; R grid spacing ratio; θ, angle between grids; φ, angle between grid and substrate.

Table 6-3: Parameters swept in rotating parallelogram model.

Parameter		*Parametric values*	*Opt. range*	*Units*
Slit length	h_A	*10, 7.5, 5*	*1.5–15*	*mm*
Slit width	h_b	*1, 0.5*	*0.5–1.5*	*mm*
Slit ratio	*r*	*100, 75, 50*	*45–100*	*%*
Grid ratio	*R*	*300, 200, 175*	*155–250*	*%*
Slit angle	θ	*90, 60, 45*	*35–90*	°
Grid angle	φ	*0, 40, 60,100, diag**	*-45–100*	°

** diag is an angle calculated to orient the parallelogram's long axis parallel to the substrate's*[cc].

[cc] $diag = -\arctan\left(\frac{r\sin\theta}{1+r\cos\theta}\right)$

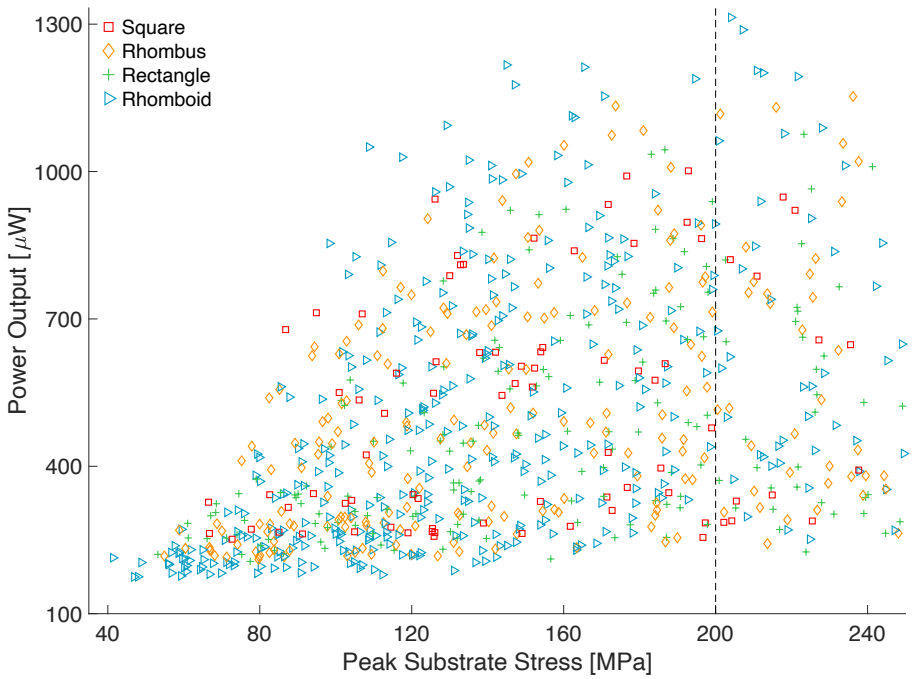

Figure 6-10: Parametric rotating parallelogram power vs. peak stress results (within material limits), differentiated by rotating unit. Safety limit indicated by dashed line.

Table 6-4: Best rotating parallelogram parametric sweep results, in descending order of output.

Sweep Input Values						*Results*		
h_A [mm]	h_b [mm]	R [%]	r [%]	θ [°]	φ [°]	P_{out} [μW]	Max T [MPa] Sub	Piezo
10	0.5	175	75	45	100	1313	~~204~~	12.5
10	0.5	175	50	60	100	1288	~~207~~	15.4
10	1	175	50	60	100	1217	145	14.7
10	1	175	75	45	100	1212	165	11.7
10	0.5	175	75	60	60	1206	~~211~~	12.6
10	1	175	75	60	100	1201	~~212~~	13.7
10	0.5	175	50	45	60	1193	~~222~~	11.5

The parametric results indicated that the best designs for harvesting were rhomboids with closely packed long holes, these aligned almost across the substrate. The slit width primarily affected the peak stresses (by determining how sharp the elliptical holes were), and how close together the slits could be (i.e. how stiff the 'hinges' between the rotating units were). Rhomboids had the advantage of a greater lateral extension, due to their elongated sides giving greater leverage than a square, and pointed corners granting more outward sweeping expansion than a rectangle. These features (alongside their greater representation within the sweep) aided in increasing the power output from the attached MFC. The grid angle, φ, could prime the rotating units to rotate outwards more easily. During

preliminary investigations (often without any constraining piezoelectric layer) having the long axis of the rotating region run parallel to the applied force tended to induce the largest auxetic response; hence the *diag* angle included in Table 6-3. This was no longer the case with MFC in place, as no models at this angle feature in the top results of Table 6-4[dd]. Most of the highest power results were slightly over the substrate stress safety limit (indicated by a strikethrough of the offending value in the tables), but still within the material limit; as this could be amended through the optimiser they were not entirely excluded.

The best results from the parametric sweep were all quite similar in appearance so, while they formed the general basis for the optimisations, many runs started from very different initial conditions to ensure a broader foundation. The optimised results, listed in Table 6-5, rarely ventured far from their starting points, unless that had a very low output. The best optimised result is shown in Figure 6-11. This features long slits cutting across the substrate, like of many of the best parametric results. The power output is 9.19 times greater than the plain baseline, much more than the prior honeycomb but with almost double the peak stress to contend with. Where the maximum strain the harvester is ever likely to be subjected to in use is known well in advance, this could be a good trade-off.

Table 6-5: Optimised Rotating Parallelogram Results, with selected design emboldened and shown in Figure 6-11.

Path	*Optimised Parameters*						*Results*		
#	h_A	h_b	R	r	θ	φ	P_{out}	*Max T [MPa]*	
	[mm]	*[mm]*	*[%]*	*[%]*	*[°]*	*[°]*	*[µW]*	*Sub*	*Piezo*
*#1**	*2.46*	*0.551*	*153.8*	*82.65*	*86.26*	*-0.164*	*1104*	~~*531*~~	*6.2*
*#2**	*2.44*	*0.572*	*155*	*81.83*	*79.07*	*0.312*	*1108*	*147*	*5.8*
#3	*5.74*	*0.531*	*155*	*95.23*	*78.93*	*1.388*	*1399*	~~*206*~~	*10.2*
#4	*10.4*	*0.990*	*155*	*84.95*	*71.19*	*-28.94*	*1255*	*175*	*10.4*
#5	*9.74*	*1.141*	*155*	*100*	*56.04*	*27.84*	*1456*	*182*	*15.3*
#6	*11.34*	*0.639*	*155.0*	*68.52*	*67.79*	*44.85*	*1429*	*198*	*12.9*
#7	*6.76*	*0.750*	*181.8*	*99.93*	*75.73*	*-0.914*	*931*	*200*	*9.3*
#8	*9.37*	*0.820*	*170.2*	*76.40*	*44.89*	*6.413*	*921*	*185*	*10.7*
*#9**	*10.36*	*0.5*	*164.4*	*59.16*	*44.39*	*44.39*	*1422*	*131*	*11.8*
#10	***10.56***	***0.518***	***153.6***	***61.61***	***62.45***	***76.86***	***1488***	***197***	***16.1***
#11	*12.51*	*0.504*	*154.3*	*45.20*	*87.78*	*89.91*	*1424*	*171*	*15.1*
#12†	*9.67*	*0.688*	*153*	*95.39*	*55.32*	*26.56*	*1483*	~~*211*~~	*16.8*
#13	*13.59*	*0.902*	*153*	*65.23*	*88.81*	*-43.22*	*1411*	*182*	*13.2*

** This run failed to optimise, so the maximum identified output is used instead.*

† The full route for this path was lost. Only the optimised result remains.

[dd] Future researches may wish to try φ=*diag*±90°, to align the long axis across the substrate.

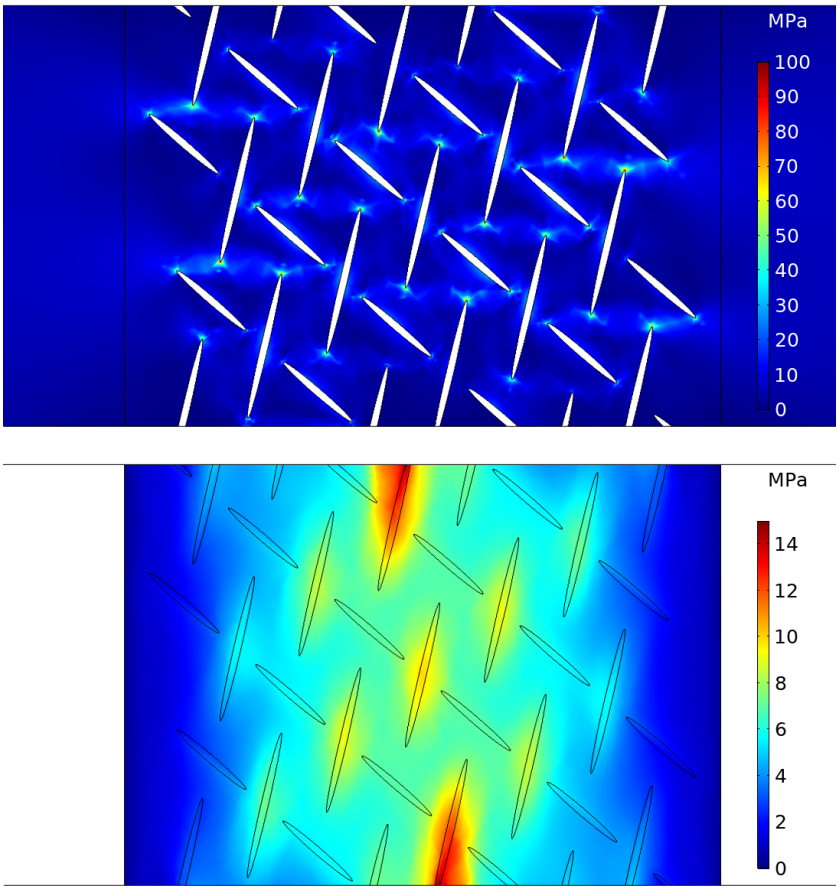

Figure 6-11: Selected rotating rhomboid auxetic region design, with slice through the substrate (upper) and piezoelectric layer (lower) to show stress concentrations.

6.2.4 For Rotating Hexagrams

The prior parallelograms were built on a grid of slits arranged along two crossing lines. An arrangement of three such intersecting lines produces a combination of regular triangles and hexagons[104,142]. Each hexagon has a triangle connected at every corner, forming a hexagram (this design is also known as the kagome-cut[142]), as depicted in Figure 6-12. Under tension it responds in a similar way to the rotating parallelograms; every unit rotating counter to its neighbours, opening the slits, and leading to the auxetic behaviour.

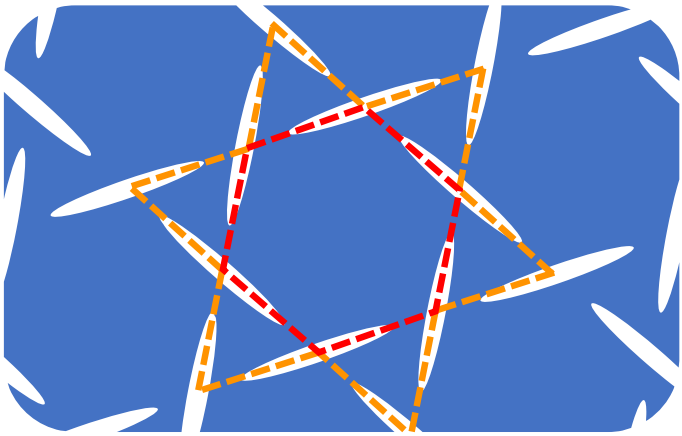

Figure 6-12: Rotating hexagram array example, with a hexagon unit highlighted in red and its assosiated triangle units in orange.

This design has four controllable parameters: h_A, the semimajor length of the slits; h_b, the semiminor width of the slits; R, the grid length ratio (which controls the slit spacing); and φ, the angle between the grid and the substrate. These are all depicted in Figure 6-13, with values listed in Table 6-6. The grid angle is fixed at 120˚ to keep the tessellation regular. This design was built outwards from a central cluster of six slits arranged around the rim of a hexagon unit. The parametric sweep results are shown in Figure 6-14, the highest output models with their optimised forms are listed in Table 6-7, with the final design in Figure 6-15.

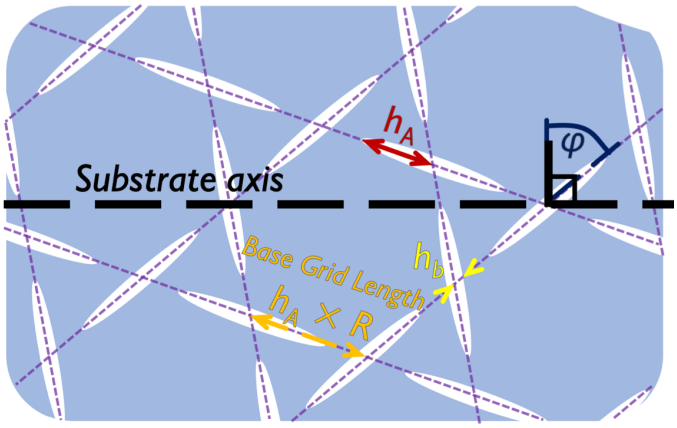

Figure 6-13: Rotating hexagram array parameters: h_A, elippse semimajor length; h_b, semiminor length; R, grid spacing ratio; φ , angle between grid and substrate.

Table 6-6: Parameters swept and optimisation ranges in rotating hexagram models.

Parameter		*Parametric values*	*Opt. range*	*Units*
Slit length	h_A	*15, 10, 5*	*3.5–17*	*mm*
Slit width	h_b	*1, 0.5*	*0.3–1.5*	*mm*
Grid ratio	*R*	*125, 150*	*110–175*	*%*
Grid angle	φ	*0, 15, 30, 45*	*-20–50*	˚

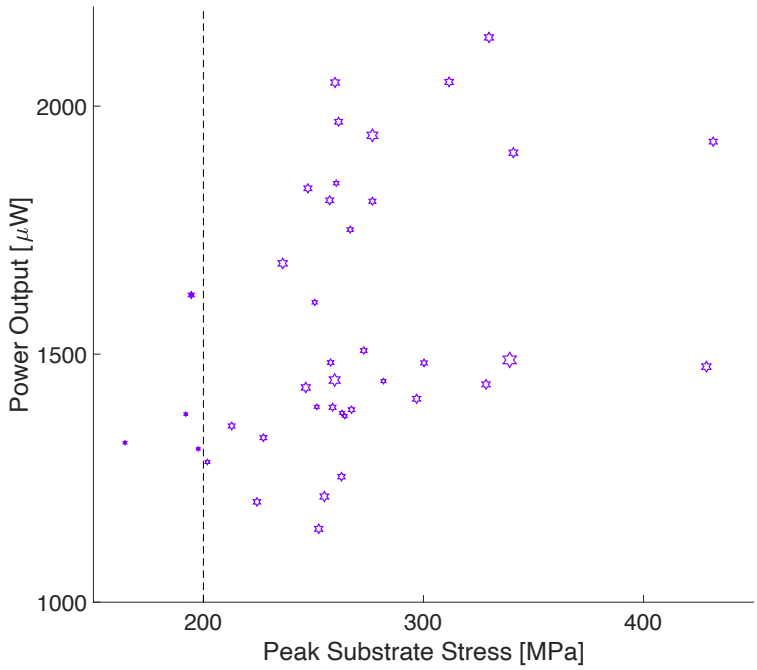

Figure 6-14: Parametric results distribution for rotating hexagram arrangement. Substrate stress limit indicated with dashed line.

Table 6-7: Best rotating hexagram parametric sweep results, in descending order of parametric output. These designs were then optimised. Final design emboldened, and depicted in Figure 6-15.

Parametric Results							*Optimised Parameters & Results*						
h_A [mm]	h_b [mm]	R [%]	φ [°]	P_{eff} [μW]	Max T [MPa] Sub	Piezo	h_A [mm]	h_b [mm]	R [%]	φ [°]	P_{eff} [μW]	Max T [MPa] Sub	Piezo
15	0.5	125	45	2139	~~330~~	~~17.9~~	16.88	1.11	129.2	44.80	1779	199	~~17.6~~
15	0.5	125	0	2049	~~312~~	16.9	14.43	0.93	159.6	-5.18	1269	~~201~~	14.8
15	1	125	45	2048	~~260~~	~~17.5~~	10.48	0.94	125.6	38.26	1587	192	16.0
15	1	125	0	1969	~~261~~	15.7	13.55	1.37	143.3	2.99	1615	198	13.2
10	0.5	125	45	1941	~~277~~	~~21.9~~	**8.87**	**0.85**	**127.5**	**41.86**	**1733**	**189**	**13.6**
10	1	125	30	1619	194*	16.0	9.70	1.06	132.2	27.36	1689	197	17.0

** This design had the highest power without breaching a limit, and was also optimised.*

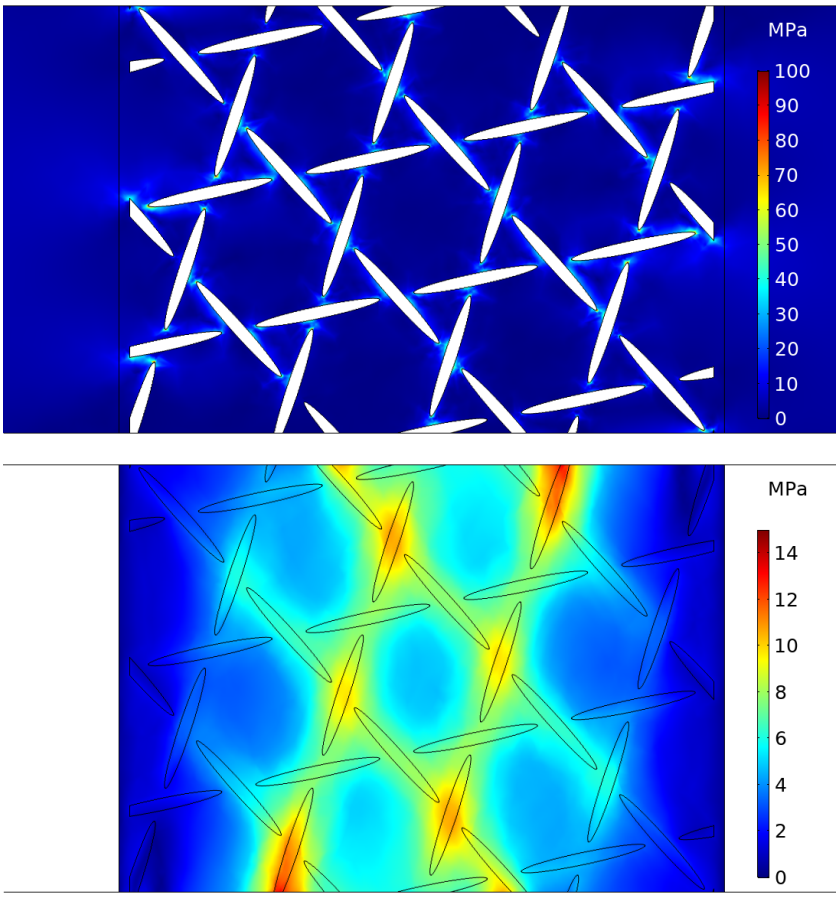

Figure 6-15: Selected optimal rotating hexagram arrangement, shown with stress map of the auxetic region of the substrate (upper) and piezoelectric layer (lower).

All the highest power models from the parametric sweep had long holes, with the tightest spacing available. They were also significantly over the peak stress limit, as were almost all the parametric results. The hinge regions were under a great deal of tensile and shear stress when acted upon. The width of the slits can influence the flexibility of these hinges, while also directing more stress there. The grid angle can again help prime the units to rotate.

As usual, the best parametric results were taken as starting points for the optimiser. For this model, the optimum power output had to go down compared to their starting point, in order to reach a design with a tolerable peak stress. The selected design has a gain of 10.7 times the plain baseline. This kind of design would be ideal for increasing the energy output of a harvester from a very low strain amplitude environment, but only if these excitations could be well known in advance. If an amplitude much less than 200 με were the expected maximum, this design could have delivered the highest gain of any tested in this chapter.

6.2.5 Rotating Triangles

By combining three elliptical slits regularly oriented at 120˚, one can create either six-pointed or three-pointed (made from hemi-ellipses cut along their minor axis) holes. Tiling the three-pointed holes can make the equilateral rotating triangle design[ee]; depicted in Figure 6-16(a). Under tension, the triangles are primed to rotate outwards, expanding these holes[104,107]. The six-pointed holes can be intermeshed to form a more complex auxetic structure, here dubbed rotating spring triangles, which has its triangles connected via arms at their corners, as indicated in Figure 6-16(b)[143].

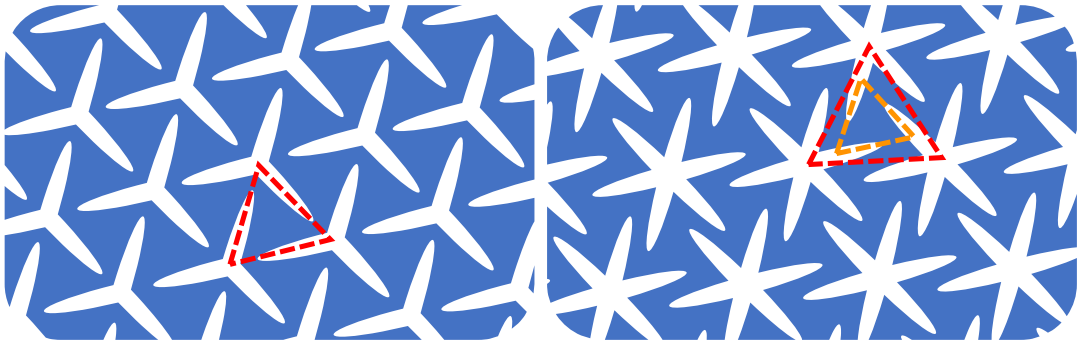

(a) (b)

Figure 6-16: Examples of (a) Rotating triangle array and (b) Rotating spring triangle (inner triangle indicated in orange, compared to the outer triangle in red).

The parameters for the rotating triangle model are: h_A, the semimajor hole length (i.e. the length from the centre of the hole to its tips); h_b, the semiminor width of the elliptical slits that make up the holes; R, the grid ratio (dictates hole spacing); and φ, the angle between the hole grid and the substrate. For the spring triangles, there is the additional factor of θ, the angle of the hole to its grid. In order to intermesh properly, this should to be approximately between 10˚ and 20˚, with 15˚ being the default[ff]. How these parameters are used to construct each model are shown in Figure 6-17, with their values listed in Table 6-8. These designs were built outwards from a central hole. Both models have checks to

[ee] Irregular triangles are possible, though tessellation becomes difficult to build in COMSOL.

[ff] The three-pointed holes could also have a θ angle, as indicated by Mizzi et al.[143], which at its extremes has hexagons connected via arms at their corners.

ensure an intact substrate[gg], and delete unattached pieces caught between the edge of the substrate and the corner of a hole during construction.

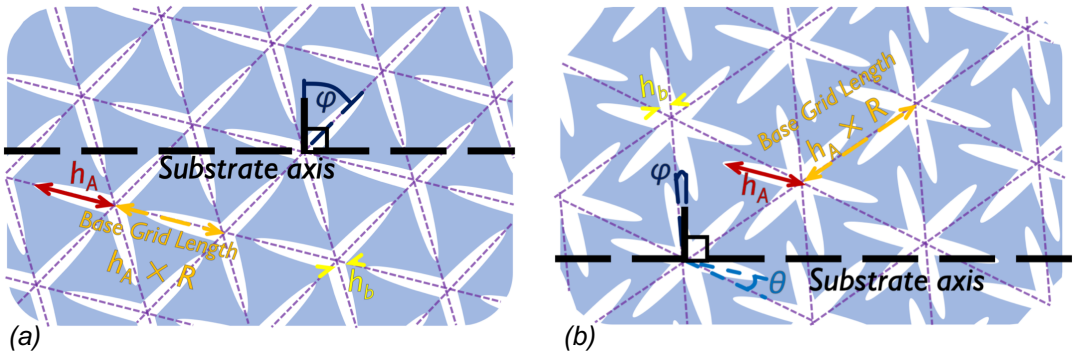

Figure 6-17: (a) Rotating triangle parameters: h_A, semimajor length; h_b, semiminor width; R, grid ratio; φ, angle between grid and substrate. (b) Rotating spring triangle has the same parameters, with the addition of θ, the angle of the holes to their grid.

Table 6-8: Parameters used in rotating (spring) triangle models.

Parameter		*Parametric values**		*Optimisation range**		*Units*
Slit length	h_A	*10, 5, 3*		*2.5–15*	*3–20*	*mm*
Slit width	h_b	*1, 0.5*		*0.45–1.5*	*0.4–1.5*	*mm*
Grid ratio	R	*66, 75, 90, 100, 125*	*70, 90, 100, 110*	*60–175*	*66–125*	*%*
Grid angle	φ	*0, 15, 30*		*-33–33*	*-15–33*	°
Hole angle	θ	*–*	*10, 13, 15, 17, 20*	*–*	*-5–25*	°

** Values split by rotating triangle | rotating spring triangle models, where distinct.*

The parametric results shown in Figure 6-18 form two largely distinct bands. The rotating triangle designs have greater outputs than most of the more pliable spring triangle arrangements. The few high powered spring triangles tend to have small inner triangles with bulky connecting arms (determined primarily by *R* & *θ*) which provide leverage and a highly auxetic response. The best results listed in Table 6-9 are dominated by tightly packed long holes. During the optimisations, a few extra designs starting from even longer holes were added to further investigate the design space. The rotating triangles quickly settled into a stable optimum, which the spring triangles could not overtake; suggesting this design is too pliable to exert as much of the applied force onto the piezoelectric layer.

[gg] Rotating Triangles parameter check: $h_A(2R-1) < 2h_b$.
Rotating Spring Triangles check: $h_A + h_b + 0.9\text{ mm} > \frac{4}{\sqrt{3}} R\, h_A \sin(60^\circ - \theta)$.

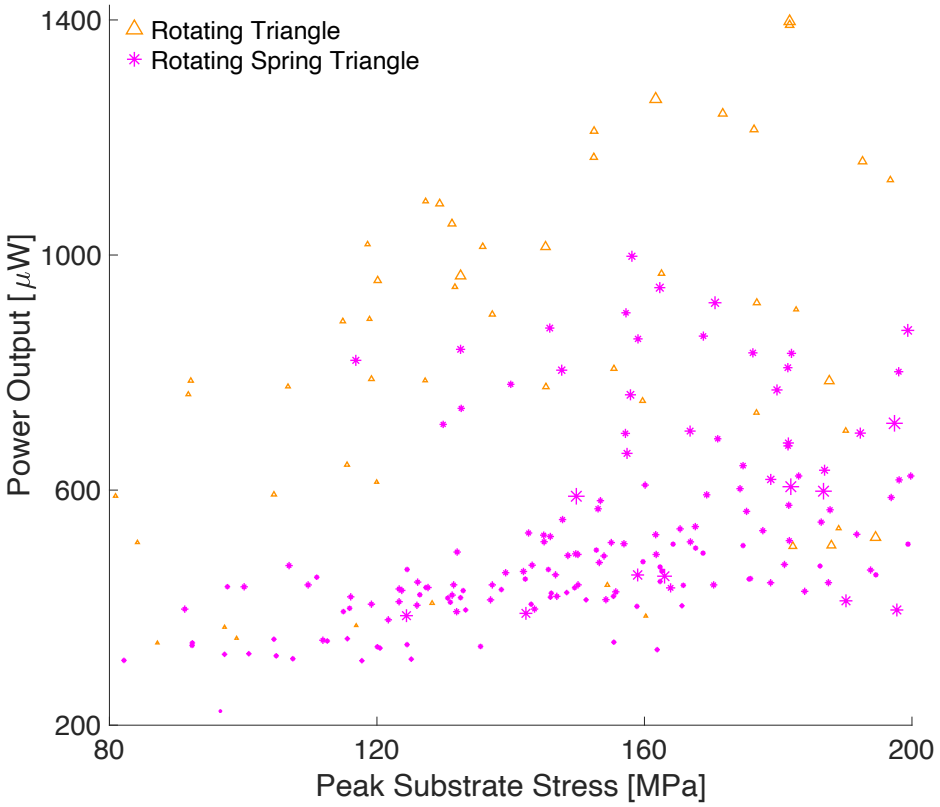

Figure 6-18: Simulated results for the rotating triangle and rotating spring triangle designs.

Table 6-9: Parametric and optimised rotating (spring) triangle results, with best designs emboldened and shown in Figure 6-19.

Design & Path #		Sweep Input Values					Sweep Results			Optimised Parameters & Results							
		h_A [mm]	h_b [mm]	R [%]	φ [°]	θ [°]	P_{out} [μW]	Max T [MPa] Sub	Max T [MPa] Piezo	h_A [mm]	h_b [mm]	R [%]	φ [°]	θ [°]	P_{out} [μW]	Max T [MPa] Sub	Max T [MPa] Piezo
Rotating Triangles	#1	10	0.5	66	15	–	1398	182	13.9	9.77	0.450	69.97	16.00	–	1531	187	14.9
	#2	10	0.5	75	30	–	1391	182	10.4	13.56	0.458	68.38	30.33	–	1646	199	10.7
	#3	10	1	75	15	–	1265	162	14.4	13.23	0.503	67.17	6.43	–	1593	194	~~17.7~~
	#4*	15	1	75	0	–	1001	146	12.5	**12.28**	**0.494**	**67.61**	**2.97**	**–**	**1656**	**191**	**14.6**
Rotating Spring Triangles	#1	10	0.5	90	0	15	944	162	11.8	9.65	0.451	88.06	-0.19	6.19	1086	208	12.9
	#2	10	0.5	90	0	17	919	171	12.1	10.17	0.450	82.07	0.17	10.29	1088	133	12.1
	#3	10	0.5	90	30	10	902	157	8.13	10.81	0.536	77.65	30.38	9.27	1114	128	11.1
	#4	10	1	90	0	10	876	146	9.83	15.38	0.802	84.55	1.24	9.22	1191	189	14.9
	#5	10	0.5	90	0	20	872	199	12.6	10.36	0.457	81.24	-0.54	17.36	1037	181	12.3
	#6*	15	1	100	15	15	867	~~234~~	12.3	17	0.452	83.62	15.81	9.22	1232	172	13.3
	#7*	17	0.5	90	15	15	1098	195	13.1	17.38	0.457	82.69	16.24	9.34	1231	169	13.3
	#8*	17	0.5	90	0	20	947	~~203~~	16.1	**16.67**	**0.45**	**75.83**	**0.49**	**16.54**	**1280**	**185**	**17.5**
	#9*	17	0.5	90	10	20	997	~~239~~	13.1	16.61	0.421	81.61	8.43	9.27	1227	196	16.7
	#10*	16	0.5	90	1	15	1094	~~266~~	~~21.4~~	15.05	0.572	85.41	1.16	11.45	1214	199	15.8

** This path did not originate in the parametric sweep, and was an extra optimisation.*

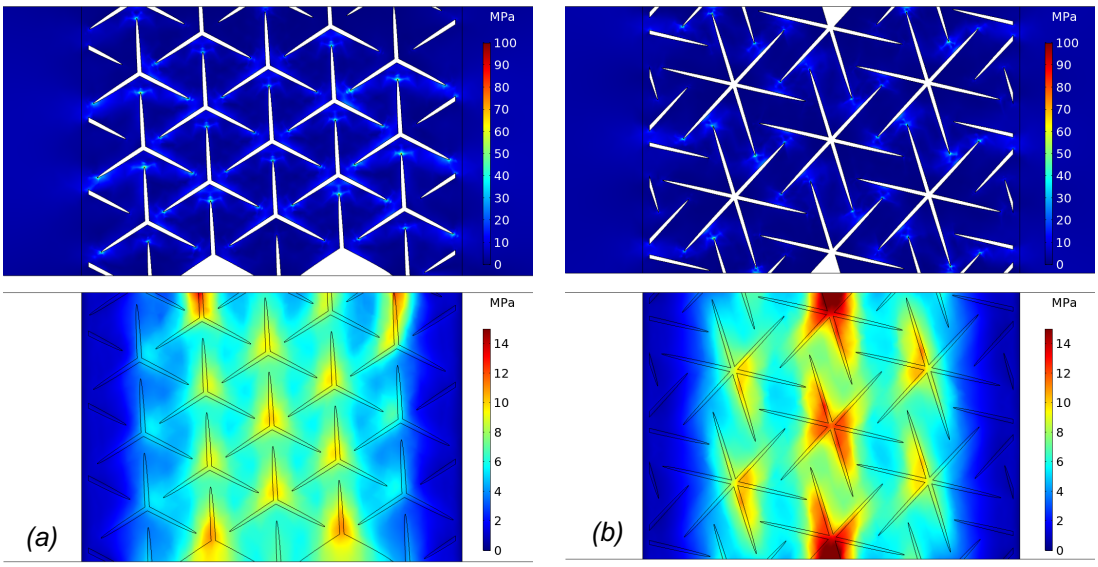

Figure 6-19: Stress concentrations in optimised (a) Rotating triangle and (b) Rotating spring triangle designs; substrate only view (upper) and MFC (lower).

The rotating triangle arrangement shown in Figure 6-19(a) produces a gain of 10.22 times the plain baseline, while the best spring triangle arrangement, shown in part (b), generates only 7.9 times as much; therefore only the regular rotating triangle design has been selected for manufacture. A small wedge of material was removed from this design (seen as the rightmost gap at the lower edge in Figure 6-19(a)), as it was only attached to the rest of the substrate by <0.3 mm of material and its absence made no significant loss to the power output.

6.2.6 For I-Holes

The final type of auxetic design covered in this chapter is based on interlocked I-shaped-holes; found in Mizzi, et al.[112], who liken its auxetic mechanism to a 'fibrils and nodules' structure, or (if the slits were tightly packed) a re-entrant honeycomb. Building these I-hole close together leaves an array of rectangular blocks connected by narrower S-shaped beams. Under tension, these beams will tend to rotate, and due to the mirrored arrangement of these S-shapes this pushes the rectangular areas outwards; leading to the auxetic behaviour.

Two versions of the design were tested: one with the I-holes aligned across the substrate axis, here called I-beams, and one with them aligned along the axis, henceforth dubbed H-beams[hh]; examples of both are shown in Figure 6-20. They are essentially the same arrangement, with one rotated 90˚ to the substrate[ii]. Both designs are controlled through the same five parameters: h_A, the length of the I-hole's crossbeams; t_b, the I-holes' beams width; r, the ratio of central beam to crossbeam length; and sep_{ax} & sep_{lat}, the axial & lateral separation between the holes (these control the S-shapes). These parameters are depicted in Figure 6-21 and their range of values listed in Table 6-10.

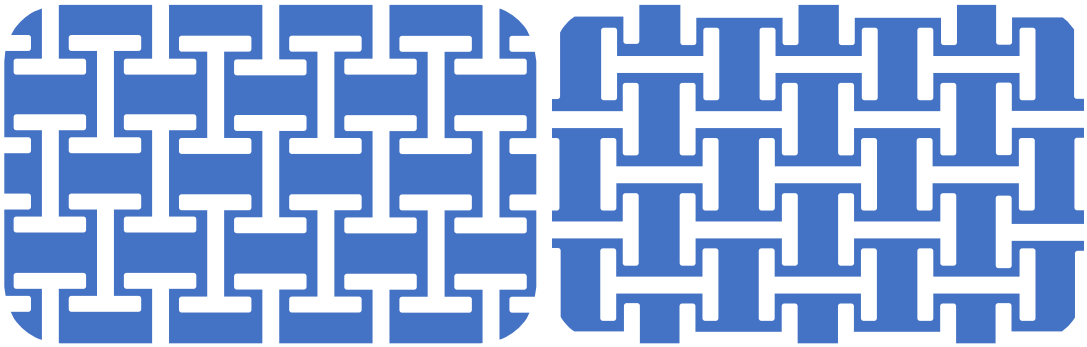

Figure 6-20: I-hole example constructions: (a) I-beam: all central beams perpendicular to substrate axis. (b) H-beam: all central beams parallel to substrate.

These designs were built outwards from an I-hole in the centre of the auxetic region. The prior domain checks were in place to maintain a viable substrate design, with a parameter check ensuring $gap = h_a - 2(sep_{ax} + t_b) > 0.5$ mm. All I-hole corners were filleted to a radius of $t_b/4$. The H-beam designs also removed any hanging pieces of the substrate, like the prior rotating triangles.

[hh] There was an intention to test an anti-tetrachiral interlocked arrangement of these I-holes, as seen in [112], but COMSOL continually gave insoluble decomposition errors.

[ii] Having an arbitrary φ angle in these designs is possible, but more complicated than the designs with elliptical holes (could arrange the holes, group them, then rotate them together).

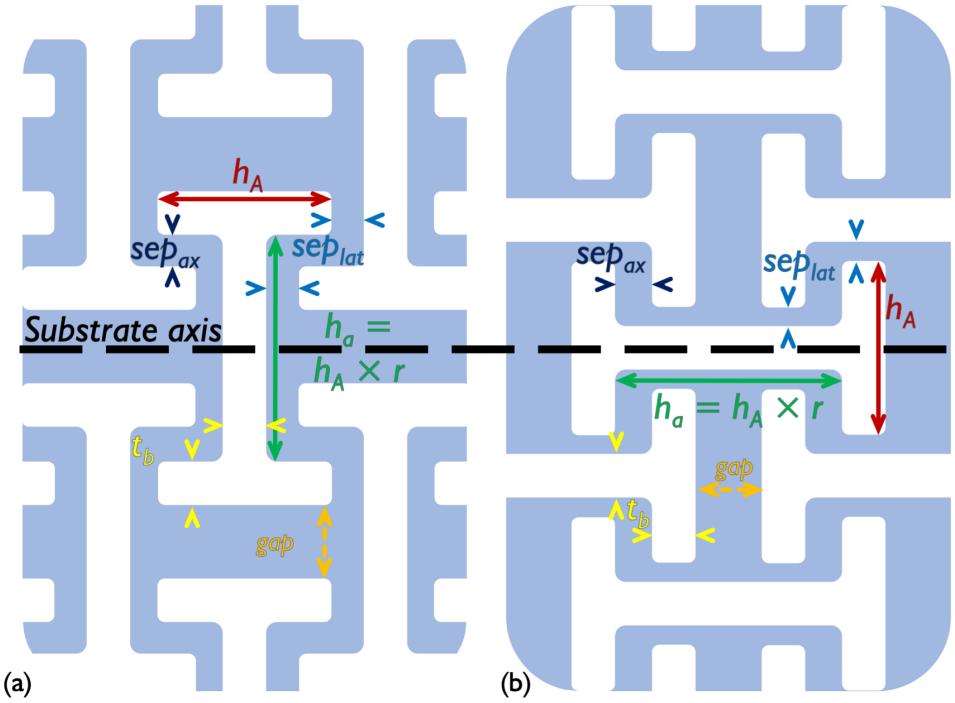

Figure 6-21: I-hole construction with parameters for (a) I- & (b) H-beam designs: h_A, I-beam crossbeam length; r, ratio of h_A to centre beam length; t_b, beam thickness; sep_{ax} & sep_{lat}, axial and lateral separation between beams respectively.

Table 6-10: Parameters used in both I–beam and H–beam models.

Parameter		Parametric values	Opt. range	Units
Hole length	h_A	5, 10, 15	5–15	mm
Hole width	t_b	1, 2.5, 5	0.45–6	mm
Hole ratio	r	50, 75, 100, 150, 200	50–250	%
Hole	sep_{ax}	1, 2, 5	0.5–7.5	mm
Spacing	sep_{lat}	1, 2, 5	0.5–7.5	mm

From the parametric results displayed in Figure 6-22, there is a clear divide between the I-beams, predominantly on the left (lower stress and power), and the H-beams, spread across to the right side. This indicates the H-beam configuration is likely to be more successful for harvesting purposes, though the higher peak stresses could become problematic. The difference is due to the orientation of the S-shaped hinge regions. The I-beam hinges are oriented such that each joint is primarily under shear stress, while the H-beam joints are also under direct tension while they flex. This makes the latter more susceptible to applied strains, and thus better able to pass them onto the MFC. The highest results, listed in Table 6-11, suggest large but narrow holes to be best; the I-beams worked better with the 10 mm than the 15 mm long crossbeams however, largely unlike the best H-beams. In all listed cases the central beam was longer than the crossbeams. The spacing between the I-holes tend to favour

the distance across the substrate, usually with a mismatch in their relative size. This, coupled with the narrow I-holes, results in bulky hinge regions between holes, rather than flexible S-shaped beams, which act as leavers (reminiscent of the prior rotating rectangles). The best parametric designs, with some extras to explore the design space, were the starting point for the optimisations.

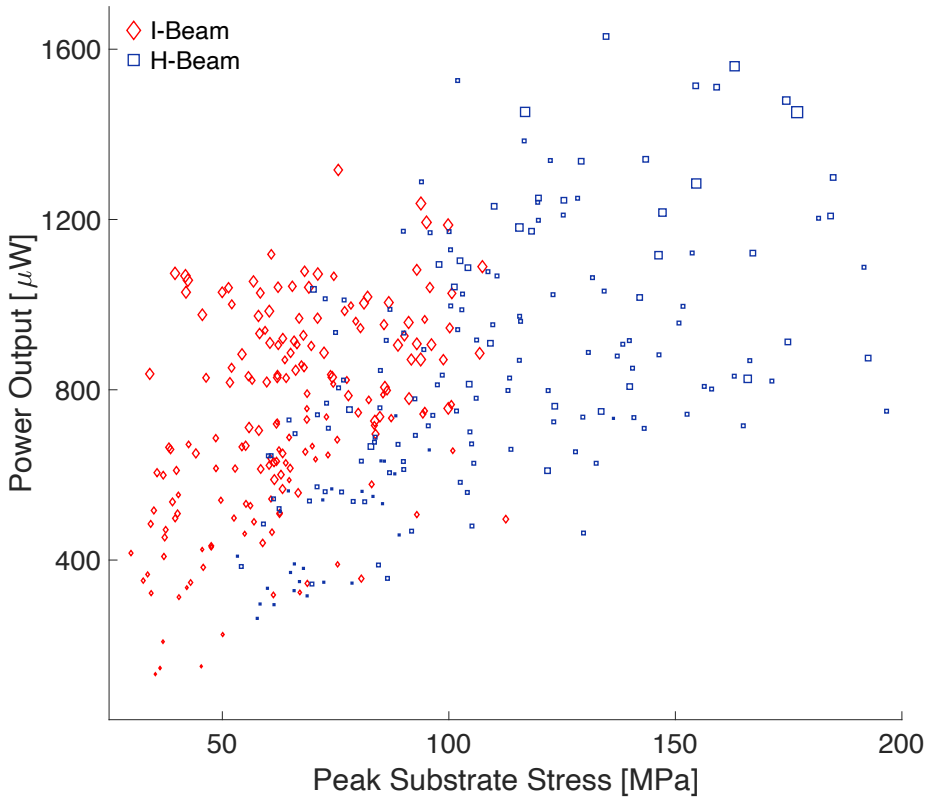

Figure 6-22: Parametric results for I-hole designs; overstressed models removed. Marker size indicated peak MFC stress.

Table 6-11: Best parametric and optimised I- and H-beam design results, with best designs emboldened and shown in Figure 6-23.

Design & Path		Sweep Input Values					Results			Optimised Parameters & Results							
		h_A [mm]	t_b [mm]	r [%]	sep_{ax} [mm]	sep_{lat} [mm]	P_{out} [µW]	Max T [MPa] Sub	Max T [MPa] Piezo	h_A [mm]	t_b [mm]	r [%]	sep_{ax} [mm]	sep_{lat} [mm]	P_{out} [µW]	Max T [MPa] Sub	Max T [MPa] Piezo
I-Beams	#1	10	1	200	5	5	1316	76	12.3	**13.22**	**0.5**	**141.2**	**3.46**	**5.38**	**1558**	**99**	**16**
	#2	10	1	150	5	2	1238	94	14.1	11.46	0.50	173.5	4.34	5.43	1473	129	14.4
	#3	10	1	150	5	1	1193	95	13.9	13.60	0.5	93.2	1.20	3.30	1496	112	13.3
	#4	10	1	200	5	2	1187	100	13.5	14.74	1.96	231.6	5.80	5.58	1361	69	~~17.5~~
	#5*	10	1	100	1	1	836	74	8.8	13.77	0.5	99.3	1.12	4.27	1493	95	12.7
	#6*	13	3	150	5	2	472	59	8.6	11.53	0.5	163.0	4.30	5.04	1476	126	16.0
H-Beams	#1	15	1	150	2	5	1630	135	10.0	**14.63**	**0.46**	**144.0**	**2.54**	**5.74**	**1937**	**186**	**11.3**
	#2	15	1	200	2	1	1560	163	~~17.5~~	14.90	0.63	202.4	1.86	1.79	1773	197	~~17.6~~
	#3	10	1	150	2	5	1526	102	7.0	10.32	0.45	161.7	2.17	5.81	1917	143	9.0
	#4	10	1	200	2	2	1514	154	9.2	11.58	0.46	170.5	1.58	2.67	1823	163	10.7
	#5*	5	1	145	1	1	1327	132	6.8	5.13	0.45	169.3	0.99	1.35	1512	130	7.0
	#6*	7.5	1	150	1	1	955	111	7.1	10.32	0.47	141.2	1.25	1.36	1618	170	12.6

** This path did not arise from the best parametric sweep results, but was an extra optimisation.*

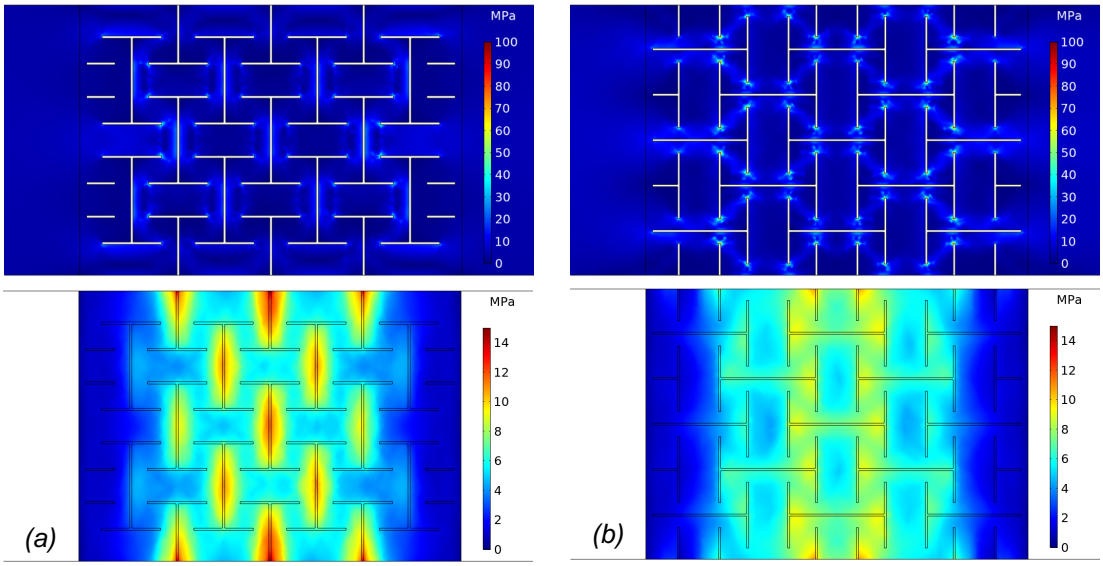

Figure 6-23: Best designs found for (a) I-beam, and (b) H-beam arrays; shown with stress concentration in substrate (upper) and MFC (lower).

Overall these results demonstrate that the H-beam orientation is better for the MFC's power output. The orientation of the rectangles nestled between the I-hole crossbeams is probably a significant factor; the long side aligned across the substrate makes the lateral expansion easier. Though both final designs appear quite similar, with their respective orientations being the most significant difference, their power outputs are 9.6 and 12.0 times the baseline respectively. It is worth noting the higher stress areas (in pale blue) in the H-Beam substrate design in Figure 6-23(b) form an outline reminiscent of the previously discussed re-entrant honeycomb arrays, indicating a similar mechanism[105,112]. Only the H-beam design was manufactured. It and all the selected substrates are shown in full in Figure 6-24.

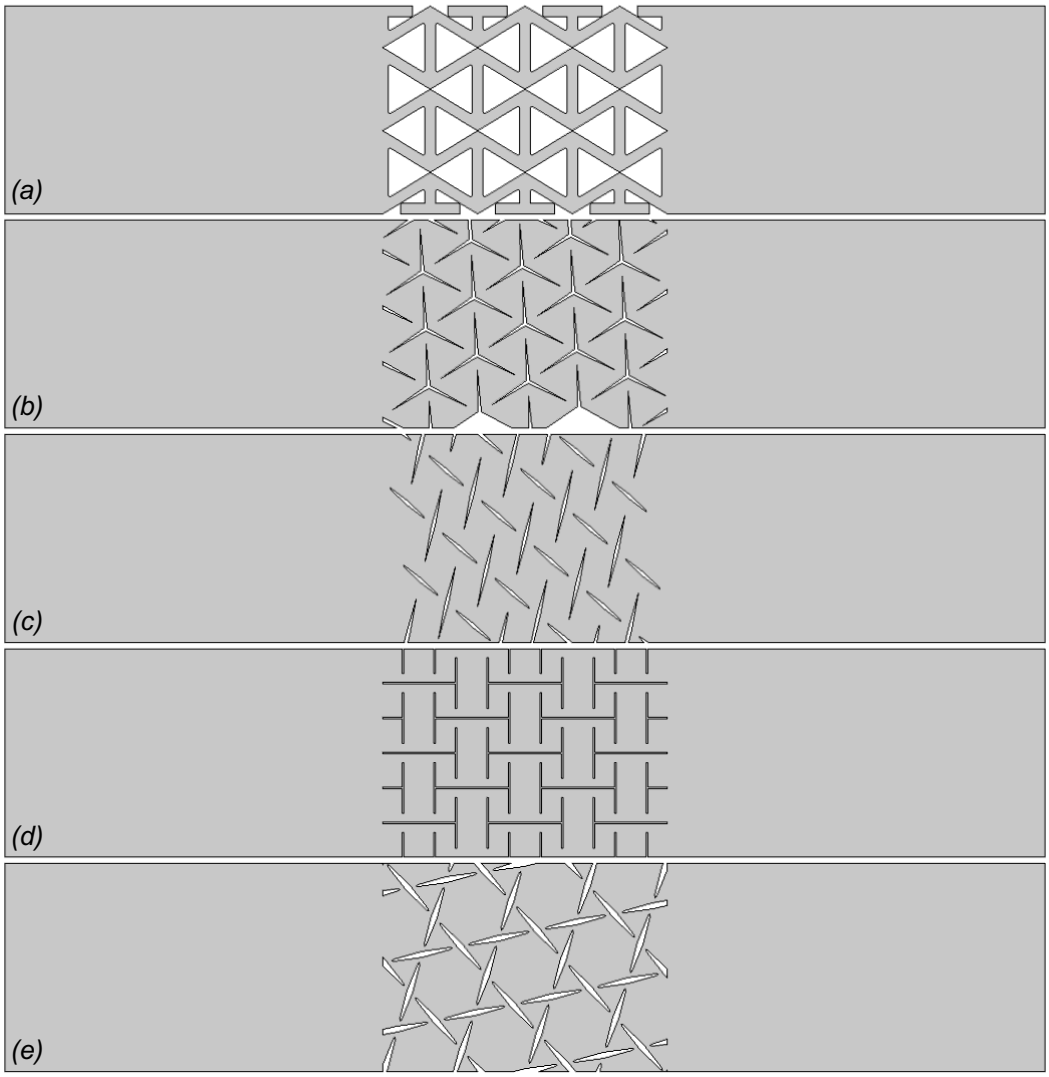

Figure 6-24: All optimised auxetic substrate designs: (a) re-entrant honeycomb; (b) rotating triangles; (c) rotating parallelograms; (d) H-beams; (e) rotating hexagrams.

6.3 Experimental Study

6.3.1 Method

Manufacturing the selected substrates was more complicated than in earlier chapters, as all the auxetic designs have narrow features closer than 0.4 mm. Laser cutting these in aluminium alloy would cause burns or melt the surrounding parts; while water jet or plasma cutting was too imprecise. This left electric discharge machining (EDM) as the most viable option, despite its expence[144–146]. The substrates were milled from a sheet to the plain's dimensions, then the auxetic designs were made by drilling pilot holes and EDM cutting. The bonding process is then similar to the prior method: applying epoxy to the middle of the substrate and clamping the MFC under pressure in a vice for over 24 hours at

room temperature. Wires were soldered to the electrode contact points, and taped down to reduce stress on the soldering joint and prevent shorting to the substrate. Due to the cost of MFC, only six harvester samples were made: one of each final design, and a plain baseline, as shown in Figure 6-25.

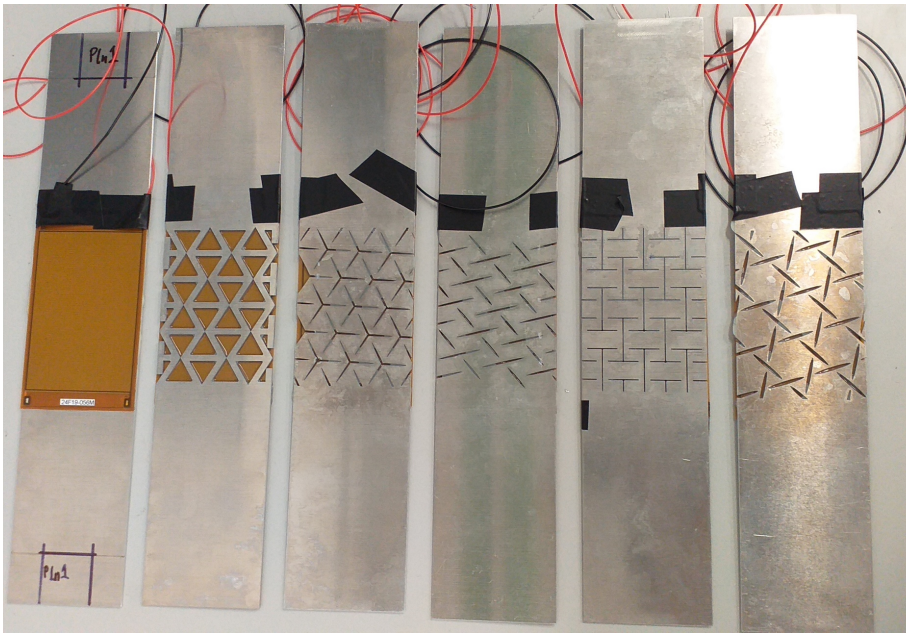

Figure 6-25: Photograph of all samples. Auxetic samples seen from the underside to better show the designs.

The experimental procedure and subsequent analysis is almost identical to that used in section 5.2.2. The only significant difference is that, due to the longer samples, the clamping depth was 25 mm and a 100 με excitation was thus 25 μm peak-to-peak. Otherwise, the test started by raising 1 mm more than the amplitude, to keep the sample in tension throughout, followed by the sinusoidal excitation for 200 s while the attached load was automatically ratcheted through the resistances listed in Table 5-6 and the voltage output from the MFC was recorded through the LabView interface.

To test a more realistic use case, a sample of arbitrary data was generated to emulate the typical noisy strain experienced by a bridge in use[33]. This excitation was used on all samples, across a fixed load of 448 kΩ (this includes the LabVIEW interface's internal impedance), to provide a consistent input for better comparison. The excitation displacement is shown in Figure 6-26, without the initial ramp (3 s, to gradually bring the sample to the starting point, and give the operator time to initiate voltage measurements). The procedure was otherwise similar to that of previous chapters. Gain was calculated by comparing each sample's total energy output during the excitation to that of the plain sample.

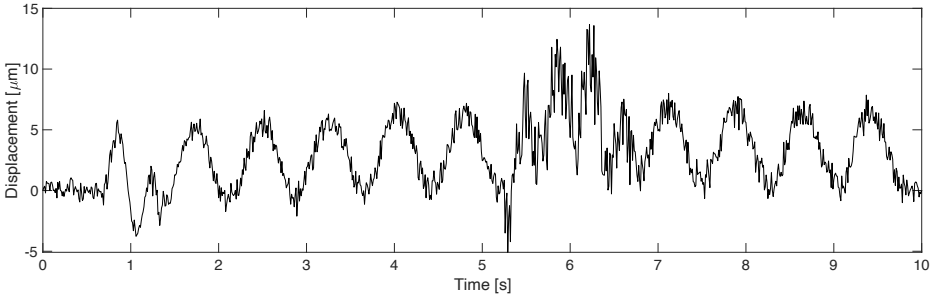

Figure 6-26: The bridge emulating excitation input displacement.

6.3.2 Results & Discussion

The highest output results from each of the six samples at the same excitation (10 Hz, 100 με peak-to-peak) are shown in Figure 6-27. The corresponding models are also shown here. The k_a values used in each model's TELs and the experimental optimum values they emulate are listed in Table 6-12. These values were derived by comparison to Figure 6-28, where the appropriate linear regions (k_a around 1-50 GN/m^3) are given in equation 6–1-6, along with R^2 fitting values.

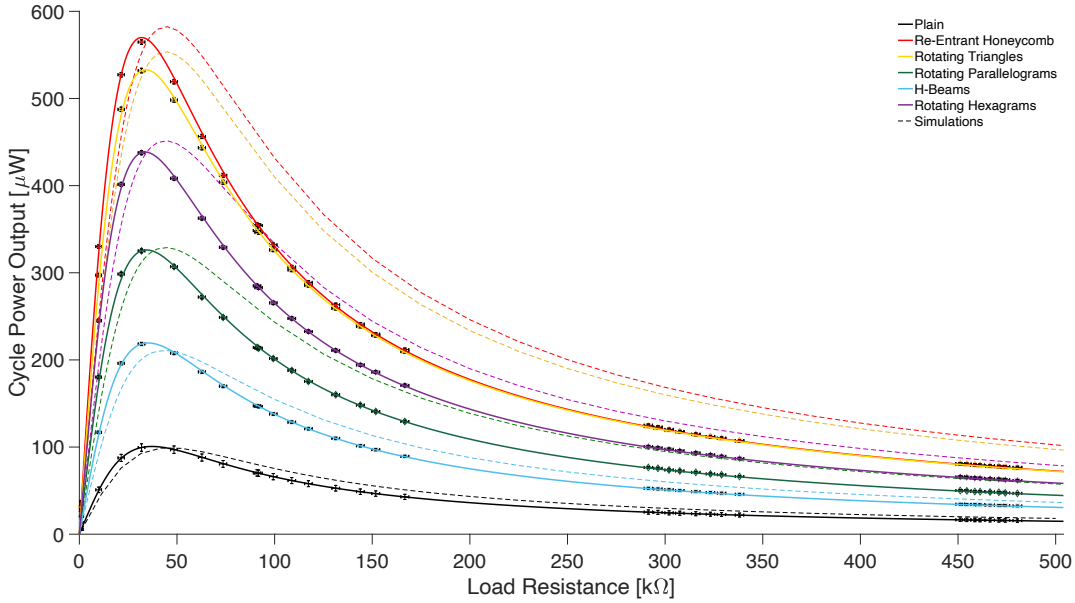

Figure 6-27: Best resistance sweep results from all samples at 10 Hz, 100 με (25 μm) excitations, with equivalent models as dashed lines in the same colours.

Table 6-12: Optimum results from Figure 6-27, with corresponding TEL spring constant, k_a.

Harvester	R_{Opt} [kΩ]	P_{Opt} [μW]	Gain	k_a [GN/m^3]
Plain	37.1	100.7	–	32.8
Honeycomb	31.9	569.9	5.66	25.5
Triangles	34.0	533.1	5.29	14.4
Parallelograms	34.4	326.1	3.24	10.5
H-Beams	35.3	219.4	2.18	5.5
Hexagrams	33.7	438.5	4.35	11.5

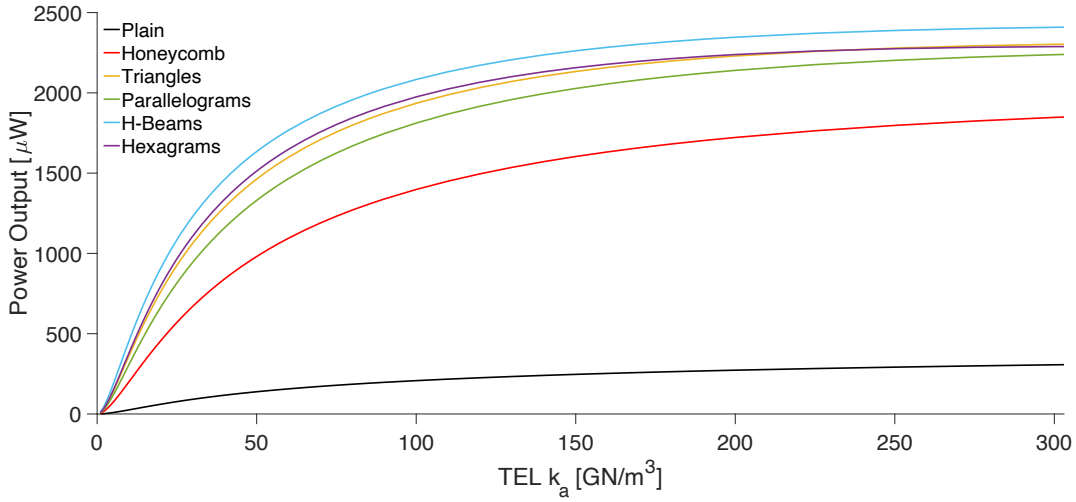

Figure 6-28: Thin Elastic Layer spring constant per unit area, k_a, for all designs.

$$P_{Plain} = 3.268\,k_a - 6.342\ ; \qquad R^2 = 0.9969 \qquad \text{Eq.6–1}$$

$$P_{Honeycomb} = 23.54\,k_a - 30.39\ ; \qquad R^2 = 0.9951 \qquad \text{Eq.6–2}$$

$$P_{Triangles} = 39.95\,k_a - 42.92\ ; \qquad R^2 = 0.9959 \qquad \text{Eq.6–3}$$

$$P_{Parallelograms} = 37.98\,k_a - 71.60\ ; \qquad R^2 = 0.9996 \qquad \text{Eq.6–4}$$

$$P_{H-Beams} = 49.76\,k_a - 54.38\ ; \qquad R^2 = 0.9976 \qquad \text{Eq.6–5}$$

$$P_{Hexagrams} = 42.94\,k_a - 55.45\ ; \qquad R^2 = 0.9971 \qquad \text{Eq.6–6}$$

The prior models indicated that the order of gain for the selected designs (from least to highest output) would be: re-entrant honeycomb (a gain of 6.09×); rotating parallelograms (9.19×); rotating triangles (10.23×); rotating hexagrams (10.70×); and H-beams (11.96×). The baseline plain sample performed far better than the model anticipated (with a k_a value almost double that found for the narrower MFC in section 6.1), and this lowered all the auxetic samples' experimental gains relative to it. Some of the lower than anticipated gain factors in Table 6-12 are also due to some epoxy leaking into the holes of the various auxetic regions,

which caused the experimental gains not to replicate the order of the models. Other than the honeycomb design (the only auxetic sample to exceeded the initially assumed k_a value), the holes are long and narrow, and could be inadvertently filled with epoxy quite easily; which would reduce their flexibility (embedded in the k_a value for that sample). This contributed to the honeycomb design being found to have the highest experimental gain, despite being the lowest found in the simulations. The H-beam sample had many of its especially narrow holes completely filled in during curing, hence it had the lowest output of any auxetic sample. Ideally a new sample would have been made and tested (along with multiple samples of each design) but the MFC was prohibitively expensive. Besides this sample, the auxetic model k_a values were found to be quite similar to each other and within the expected range. This demonstrates that the TELs are an appropriate way to emulate the bonding adhesion losses in designs other than the plain and re-entrant honeycombs; it may be advisable to calibrate any new design with a similar preliminary one to obtain the most accurate value of k_a during modelling, if feasible. More precise bonding than is possible by hand, with a smaller amount of epoxy more evenly applied to the substrate, would reduce the overflow and improve the power output dramatically.

The increased thickness of the aluminium substrate lead to an increased power output from the expectations found during modelling (from 0.9 mm thick, rather than the available 1.5 mm), for all but the rotating parallelogram and the H-beam samples. These were found to have the lowest k_a values, which counteracted the greater authority of the thicker substrates. The greatest increase from the modelled expectations were on the plain and honeycomb samples, due to their higher than modelled k_a values.

As with previous results, the same k_a value can be used to emulate a particular sample at any input excitation, as shown in Figure 6-29. This holds for all the different auxetic designs. The gain factors for all these samples remain approximately constant at any given input, as before.

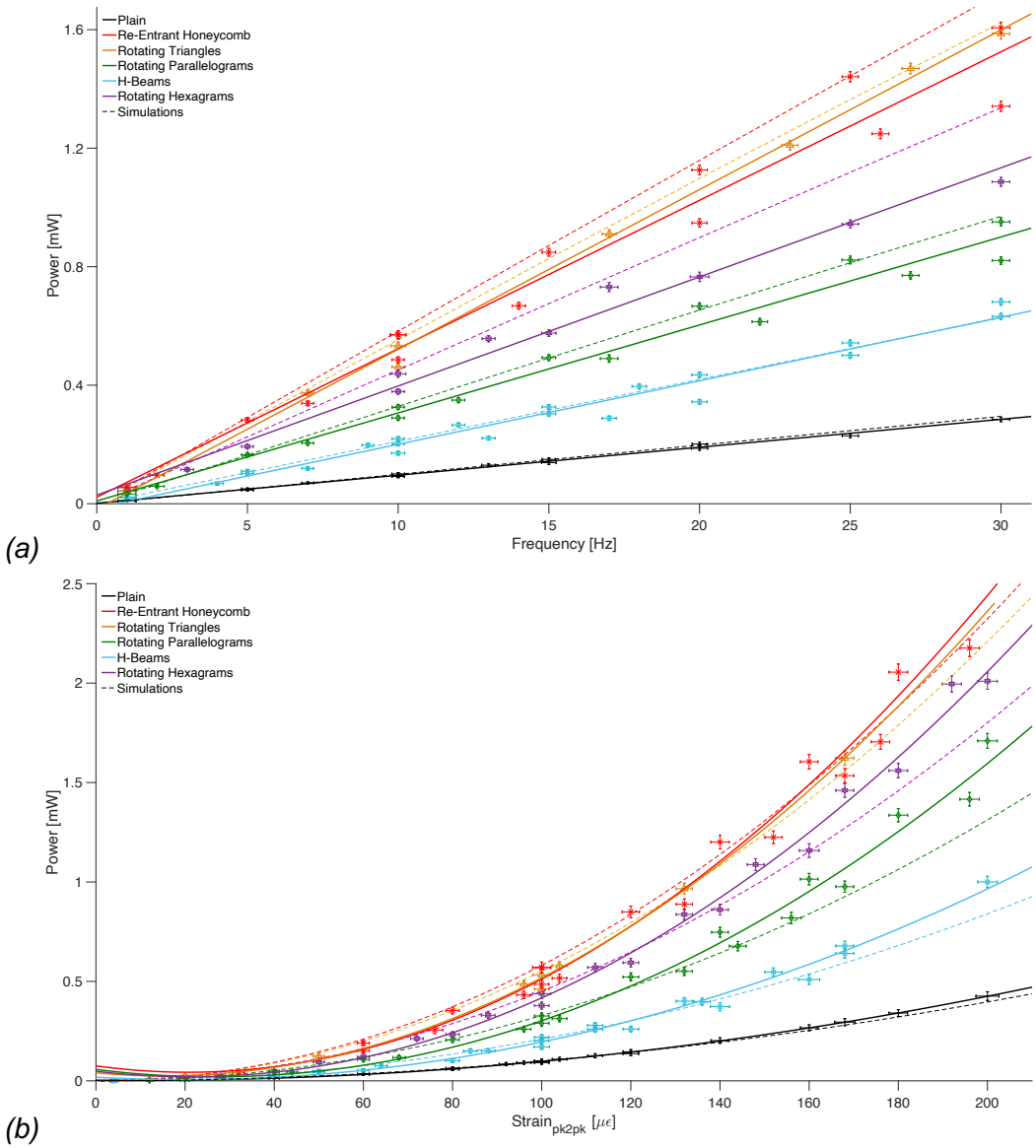

Figure 6-29: Results from (a) Frequency and (b) Amplitude sweeps on all samples. Experimental fits in solid lines, with dashed equivalent models of the same colours.

The amplitude sweep models slightly underestimate the experimental outputs at higher strains. This could indicate that assuming the materials are always in the linearly proportional regime (of their stress-strain relations) is not as valid at these higher excitations. The frequency sweeps are generally well matched to the experimental data. The hexagram has the largest deviation, due to some low datapoints bringing their regression down more significantly than other samples.

Compared to the MFC samples in chapter 5, the re-entrant honeycomb design produced a greater output at the 10 Hz, 100 με excitation (468 to 570 μW here) with similar k_a values (24 to 26 GN/m^3), while the plain samples showed a much more dramatic difference in both values: 41 to 101 μW and 13 to 33 GN/m^3. The difference in plain power arose entirely from the increased bonding strength seen on the newer sample; for example, equation 5–3 predicts that if that sample had

k_a = 33 GN/m^3 then it's output would have been 111 μW, quite comparable to this sample. Both honeycomb samples concentrated the majority of the applied strain into the region under the piezoelectric layer, so the latter sample's output is higher because the amplitude on the longer sample is larger (18 to 25 μm) for the same overall strain; thus the piezoelectric material is under more strain. The optimal load for all these samples was notably lower than the theoretical or chapter 5 ones. This is likely related to the MFC deriving from a different batch; for this chapter they were all grade B (rather than the prior grade A) due to its off-the-shelf availability. This was expected to have the same electrical properties, but slightly diminished optical ones.

The concentrating effect of the auxetic region also applied to dynamic excitations. The results from the bridge excitation on the plain and re-entrant honeycomb samples are shown in Figure 6-30, with the relative gain of all samples listed in Table 6-13. The voltage tracks of all samples had a similar shape, with the only significant difference being their amplitude. These gain factors were within experimental variation of those in Table 6-12, indicating the auxetic designs operate under arbitrary excitations in a similar way to the sinusoidal ones.

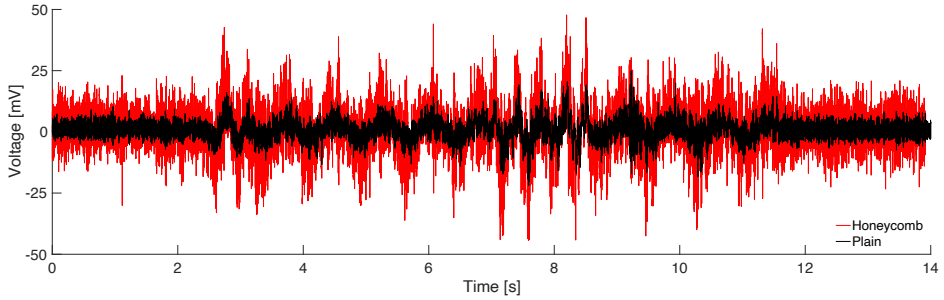

Figure 6-30: Voltage output of plain and honeycomb samples under the bridge emulating excitation.

Table 6-13: Gain results from all samples under the bridge emulating excitation.

Harvester	*E_{total} [nJ]*	*Gain*
Plain	*0.470*	*–*
Honeycomb	*3.006*	*6.39*
Triangles	*1.862*	*3.96*
Parallelograms	*1.526*	*3.25*
H-Beams	*1.137*	*2.42*
Hexagrams	*2.083*	*4.43*

These results demonstrate that any of these auxetic designs would be an improvement on the baseline. The cost to manufacture each sample was much higher than for those in chapter 5, due largely to the optimised designs having such narrow features that they could only be cut by EDM. Tighter controls on these features at the modelling stage would have allowed the much cheaper laser cutting to have been used but these designs would have had lesser outputs. Depending on the intended application and its intended lifespan, this may be an acceptable trade-off. Using the auxetic substrate is an easy to implement way to increase the power output from piezoelectric material. By concentrating the ambient strain energy into this material the output magnitude is increased, but otherwise doesn't alter the output signal's timing or waveform; making it quite simple to integrate with existing control circuitry for self-powering sensor nodes. This is ideal for structural health monitoring.

6.4 Conclusion

In this chapter, many auxetic harvester designs have been simulated for comparison. Five optimised designs were selected to be manufactured (and their power gain over a plain baseline): the re-entrant honeycomb (5.66×; i.e. 570 μW versus 101 μW at 10 Hz, 100 με); the rotating triangles (5.29×); rotating parallelograms, specifically rhomboids (3.24×); the H-beam holes (2.18×); and the rotating hexagrams (4.35×). These gains remained consistent at a range of input excitations. The modelling of a range of auxetic designs has shown that the process works for more than just the re-entrant honeycomb. The k_a values were of a similar range to each other, and were found capable of emulating all samples at a range of excitations with reasonable accuracy; which demonstrated their effectiveness as a fitting parameter for any auxetic design. These designs would be ideally suited for applications in self-powered structural health monitoring.

7 General Discussion

Looking at all of the previous work collectively, it is clear that using auxetic structures can significantly increase the power output of strain energy harvesters. Their stress concentration effect combined with the lateral expansion drives this power gain. The greatest power gain came from balancing the design's stiffness with its authority over the piezoelectric material. The former should be less than the rest of the substrate to focus as much of the applied strain into the auxetic region as possible, while the latter relates to how much of the strain in the substrate is transferred to the piezoelectric material. Part of this authority is derived from the available bonding area, but the ability to stretch the piezoelectric material also relies on the how forcefully the auxetic design expands; for example, the beam based re-entrant honeycomb designs had a smaller contact area than the other designs discussed in chapter 6, yet those with a larger area did not necessarily generate more power because their structures were less flexible and so couldn't expand out as much. In other designs, the width of the hinge regions were much narrower than the bonding regions and their increased outputs were evident throughout section 6.2; here the design's authority is based largely on its mechanical leverage. Note that the most highly auxetic design (i.e. the largest negative effective Poisson's ratio) is thus not necessarily the most effective design for energy harvesting (see also appendix C.VI), as these tend to lack the authority to exert their expansion onto the piezoelectric material. The most effective designs were those which increase the piezoelectric material's average overall stress while not increasing the peak stress too much in any local area. A good example of this was the peak piezoelectric material stresses in the I-beam verses H-beam designs, seen in Figure 6-23, which are much higher in the former, yet the power output of the latter is significantly greater because the increased stress is spread over a larger area of the piezoelectric material. This also protects the brittle piezoelectric material.

A selection of materials have been used throughout this work, in both the substrate and piezoelectric layer. For the active layer, this work initially focused on PZT, due to its greater power output compared to other ceramic materials or PVDF. Its brittleness was found to be even more of an issue than anticipated so LN was trialled as an alternative. This proved more resilient but also generated much less power; its greater stiffness also reduced the power gain achieved by

using the auxetic substrate (from up to 14.5 times for the PZT to only 3.6 times; see section 3.2.4). This suggested a more flexible piezoelectric material may be able to achieve larger gains. The piezo-composite MFC on the auxetic substrate had a much higher gain (11.3) than the bulk PZT equivalent (6.2), see section 5.2.3; though it still had a slightly lower output. While this was due at least in part to having a smaller volume of PZT, simply normalising the output by the active layer's volume obfuscates how the differing thickness impacts the stiffness and thereby the output; see also appendix C.I. To compensate for its lower output, MFC is more resilient to stress than bulk PZT and protected from moisture and particulates by its polymer encapsulation. It is an effective combination of flexibility and strong piezoelectric properties, ideal for use with auxetic substrates. The material for these substrates should ideally be strong to endure high stresses, while remaining flexible enough for the auxetic designs to move freely. Some other metals and non-metals were considered in early stage models but steel and aluminium were the most viable. A harder metal such as titanium might deliver a higher power output (from its much greater authority) but also required so much force to make it flex that the peak stresses in both components were untenable. Attempts at modelling plastic substrates found they were far too soft (PMMA and similar were also too brittle), absorbing much of the strain energy themselves and produced little power from an attached piezoelectric material. Steel and aluminium had the advantage of being widely available, and relatively easy to work with. Of these, aluminium is widely considered more difficult to laser cut than steel due to its thermal characteristics and more reflective surface; the designs in chapter 6 required the much more expensive EDM cutting process to shape them, in part because of this (as well as the >0.4 mm gaps). These factors are all worthy of consideration when selecting materials.

Finite element modelling proved itself an invaluable tool to aid in the design work for these harvesters. Testing the large range of possible designs experimentally would have been far too expensive and time consuming. Most models use at least one fitting parameter to better emulate the real world system they are based on, and throughout this work the main unknown during the modelling stages was the bonding strength between the components. These adhesion losses were simulated using thin elastic layers (TELs) at the boundaries between the glue and the other constituents; without these, the model outputs were unrealistically high. The spring constant per unit area, k_a, in the TELs was

used to quantify the bonding adhesion to the surface, however it would be possible (and probably less computationally intensive) to replace the entire glue layer with one TEL in future. The k_a values found to best emulate the experimental models were quite consistent in most cases; the biggest difference being found between the values in chapter 3 (in the 147-203 GN/m^3 range) versus the rest (5-33 GN/m^3). This is likely due to the smoother substrate surfaces of the latter relative to the mild steel used in chapter 3; though the much smaller size of the former's PZT was also a significant factor, as the impact of edge effects was more significant. When comparing MFC to PZT, the former samples' k_a values were consistently lower. This may have derived from the glue's weaker adhesion to the polymer encapsulation, compared to the PZT's bare electrode surfaces, or from the material parameters used to model the MFC. These were derived from Kaung[88] who did not use TELs or an equivalent in his models; the bonding losses between the MFC and his carbon fibre substrates could therefore be embedded within his material parameters. A value for k_a for any particular combination of materials can be quite easily established by testing them with a plain substrate and comparing to its model equivalent; the deviations found in the subsequent auxetic values would be small enough not to effect the modelling process. The model could then be used to optimise an auxetic design with more confidence.

A recurring problem with the experimental samples was the imperfect bonding between the substrate and piezoelectric material. The effects of this were most noticeable with the auxetic samples, as the epoxy could leak into the holes during curing and stiffen the mechanism. This occurred particularly in designs where the holes were much narrower than the re-entrant honeycomb. The bonding epoxy was applied by hand and, despite care, there was always an excess which caused these inconsistencies. If the bonding agent were applied in a more controlled way, such as through a fine spray with a mask over the holes, this could dramatically improve the quality of the bonds while also facilitating automated mass production.

These auxetic harvesters open up new applications in infrastructural health monitoring, but are restricted to those low-strain environments. The very small oscillations (of the order of 50-200 με, at around 10 Hz or less[33]) typically found in bridges (such as Figure 7-1), pipelines, or buildings are currently considered poor sources for vibration energy harvesting[10–12,18]. In order to power a sensor

(to make regular measurements of the structure's condition) in such places, engineers would currently have to choose between hundreds of meters of wires or a battery powered node (necessitating routine maintenance, in a position that could be very difficult to reach)[10,20,32,41]. With the significant gains made by the auxetic harvesters discussed above, self-powered nodes in these locations become more viable options. If the maximum strain in the target location were well known in advance then the type of auxetic design could be selected and tuned to maximise the power output within that limit. For example, in section 6.2.4 the rotating hexagram design was found to achieve a high power gain, but so severally stressed the substrate that its output had to be reduced to endure the applied load; if the intended location for the harvester was expected to never exceed a strain of 100 με (rather than that modelling stage target of 200 με) then this design could be used to greater effect. If the peak input strain were anticipated to occasionally exceed 200 με then the re-entrant honeycomb might be a more suitable design, as it had the lowest peak stress in any auxetic substrate. The stress concentration effect was sometimes found to be enough to break the piezoelectric material however. A high strain or turbulent area would therefore be inappropriate for this auxetic amplification technique. In high strain locations (such as aeroplane wings[32]) a resilient piezoelectric material could already be directly bonded to the surface, without requiring auxetic amplification. Being able to continually monitor the condition of infrastructure with these sensors would ensure any damage to the structure could be quickly identified, thereby making it easier and cheaper to schedule preventative maintenance and prevent dangerous deterioration.

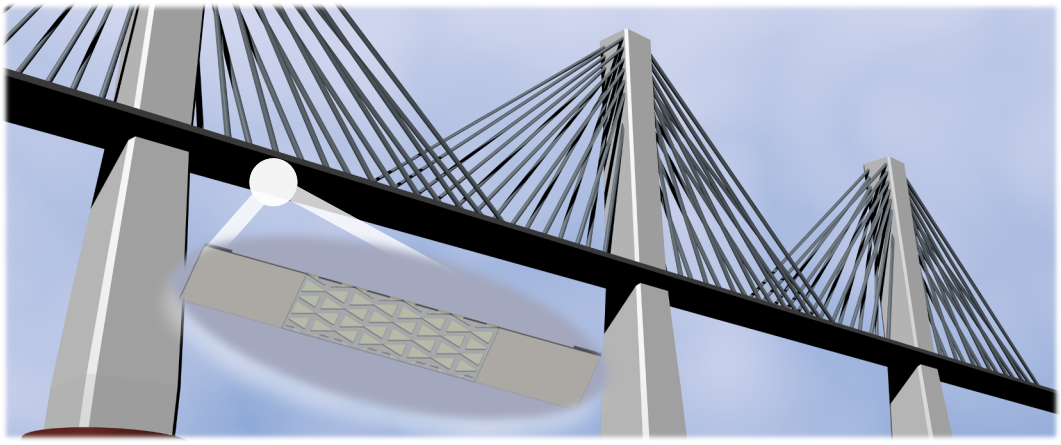

Figure 7-1: Potential application of surface mounted auxetic vibration energy harvester in situ under a bridge.

8 Final Conclusions

Using auxetic designs as the substrate of piezoelectric vibration energy harvesters has been shown to dramatically increase their power output; by 2.18-14.5 times that of their equivalent baseline. This method would be ideally suited for self-powered wireless sensor nodes in infrastructural health monitoring.

A finite element COMSOL model was used to find the increased power output arising from any particular auxetic design. Its results were found to correlate well with the experimental results once the bonding adhesion was considered with an appropriate value of spring constant, k_a, in thin elastic layers (TELs); a boundary condition placed at the top and bottom faces of the glue layer.

This model was used to maximise the output for a selection of auxetic designs, while keeping the localised peak stress in all components safely within their yield strengths. The parametric optimisation made this process much quicker than a series of manual sweeps.

The optimum substrate designs found through this model were manufactured and tested experimentally, using sinusoidal and recreated bridge excitations. This provided experimental validation of the model, as well as to establish the most appropriate k_a value for the TELs to emulate each sample. For all full size samples, k_a was in the range of 5-33 GN/m^3, and once identified for any particular harvester, each value was found to accurately emulate a range of other input conditions too.

As a baseline for comparison, each auxetic design had a solid plain substrate of the same overall dimensions and type of piezoelectric material. This could also be used to calibrate the model's TELs before designing the auxetic region.

Three piezoelectric materials were tested in this work: PZT, LN, and MFC. Of these, PZT would produce the greatest power output, but was brittle and liable to crack under high strains (>250 με) when combined with an auxetic substrate. LN was much more resilient, enduring up to 500 με without damage, but produced much less power than PZT under the same input conditions. The MFC generated slightly less power than the PZT, but on the auxetic substrate it was able to produce a much higher gain (11.3 versus 6.2 times) due to the MFC's greater flexibility. The MFC was thus found to be the most promising of these materials

for future research. Steel and aluminium were compared as substrate materials, and both were found to be viable options.

With MFC on aluminium, many auxetic designs were modelled and five were selected for experimental testing. The best of these was found to be the re-entrant honeycomb, with a gain of 5.66 times its plain baseline (570 to 101 μW at a 10 Hz, 100 με excitation). All of these optimised designs generated more than double their baseline, and each would be suitable for various energy harvesting applications; these can be selected according to the peak strain expected in their intended locations.

9 Future Work

This work above could be used to improve the viability of vibration energy harvesters in low strain environments. There are numerous ways this research could be further developed. For example, some longer term field tests could find that the stress limits used here were too stringent or too lax for the intended real-world applications. Where the harvester is surface mounted on some spacers, as in Figure 7-1, simply placing piezoelectric material on both faces of the auxetic region would be an improvement; this was prohibitively expensive for this research, but models suggests this would add an extra ~66% to power output[jj]. The use of auxetic designs could also offset the losses associated in switching from PZT to lead-free piezoelectric materials; as was shown in Figure 4-8, where the auxetic LN sample had a slightly higher output than the plain PZT one, while still being resilient enough to endure high strains (unlike the auxetic PZT samples).

Many flat auxetic designs have been previously researched[103–105,107,108,111–115], and some of these could prove even more effective than those tested in chapter 6. There are some hierarchical auxetic designs that could also be utilised for this in future[79]. Introducing smaller slits within the solid regions of the rotating unit designs, or lightning bolt kinks into the beams of the re-entrant honeycomb designs, could introduce greater flexibility and invite more auxetic behaviour to the substrate. Most auxetic designs found in literature, and those discussed here, have regular patterns made of an array of identical units. This makes them much easier to model (during their parametric construction, and there are potentially some symmetries that could be exploited to reduce the computation time), but may also limit development of non-uniform auxetic designs. Looking at the stress concentrations in some of these auxetic designs, such as Figure 5-6(b), the greatest substrate stress is often found near the edges of the auxetic region (where it joins the rest of the substrate) yet the stress in the piezoelectric material tends to be the lowest over these regions. These regions experience the most direct strain, while being least able to flex. If the auxetic design were non-uniform, the beams or hinges in the middle of the auxetic region could be narrower than those at the periphery. Procedurally generating these designs could be achieved

[jj] It is not a straightforward doubling of the output because the second layer constrains the substrate more than the one alone; though this could be countered by making it thicker.

with a radial position dependence in many of the geometric parameters. The end result should be an auxetic region which flexes outwards evenly, which could strain the piezoelectric material more uniformly; delivering more power without excessively stressing it.

There is a prospect to develop this work into three dimensional auxetic structures. Many 3D auxetic designs have been demonstrated where the framework collapses in on itself in all directions under compression[104]. Placing piezoelectric blocks within these frameworks would allow a stress to be applied from all sides, greatly increasing their power output. Compression based harvesting methods could be enhanced, and as most ceramic piezoelectric materials are stronger in compression than tension[60,93] their stress concentration is more tolerable. The mechanical losses from straining a bonding agent between these blocks and the auxetic framework could also be reduced. Integrating many such blocks into an auxetic network could be used to make a highly flexible piezoelectric metamaterial (though aligning the outputs of all the individual blocks would likely require complicated rectification to be useful, similar to ZnO fibre devices[70]), and potentially supersede bulk ceramic piezoelectric materials. These devices could be incorporated into the rubber supports under vibrating machinery to draw power while isolating them from the surroundings. The technique could also make harvesting from impacts, such as footsteps on pavements or ocean waves hitting harbour walls, more viable.

There have been some tests in putting slits directly into PVDF sheets[79], or forming the piezoelectric material into auxetic designs[100]. While preliminary simulations on the latter indicated that reducing the area would greatly diminish the power output, see appendix A.I.iv, there is scope for introducing some slits into MFC, between fibres, to encourage their motion. If these lined up in some way with the auxetic substrate (while not necessarily matching its shape), this could reduce the constraints on the substrate's motion, thus inducing more power from the strained piezoelectric fibres. Long term fatigue testing in the field would be needed to ensure these cuts would not cause severe degradation to the MFC.

Further developments on the piezo-composite materials could also support these auxetic harvesters. Having the aforementioned cuts securely built in to prevent tearing could help integrate them with an auxetic design. MFC is made from parallel fibres of PZT, and thus the auxetic nature of the substrate is only

partially utilised; the lateral expansion pulls every fibre outwards, causing them to stretch slightly more, but even without the auxetic substrate there would be some of this from its Poissonian contraction. Some of this lateral strain is inevitably lost to pulling apart the polymer encapsulation between fibres. If the fibres were arranged in a spiral or zig-zag pattern, or had an interlaced arrangement of fibres, then more of the lateral motion could be harnessed into electrical power by the fibres. By designing this fibre arrangement in tandem with the substrate, any benefits gained from the auxetic components could be further improved upon. Manufacturing this form of composite would be much more difficult than the parallel rows available now (as these are cut with a diamond saw in close-knit straight lines) but it is not an insurmountable problem; sintering or laser cutting thicker fibres into the desired shape would be possible[8,100].

Overall, this work has shown how using auxetic structures can dramatically increase the power output of vibration energy harvesters. This could easily be applied to infrastructural health monitoring, where the relatively low strains would otherwise be too small to harvest useful amounts of power from.

Appendices

Here are detailed some minor additional work that does not affect the main narrative thrust of the thesis, but could prove useful for researchers aiming to replicate or develop this work, or reassure a reader that certain minor objections that may have occurred to them have been investigated sufficiently to demonstrate they were not applicable to the main work. These are, in essence, footnotes to the main body of work that were too long or figure heavy to place upon the page.

A. Further To Chapter 3

A.I.i. Frequency vs. Time Domain

Working in the frequency domain made all the modelling much quicker; each model run would typically take anywhere from 25-150 s[kk]. A single model run of an auxetic design using a time domain analysis could take as much as 2 hours or more to generate results for a mere 5 s of excitation. Performing this for a wide range of parameter combinations would have greatly increased the processing time. Frequency domain analysis is limited to sinusoidal excitations however. Here both methods are demonstrated to arrive at the same results, with Figure A and Table a (time domain output found from the average power across the 5 s). The excitation was of the form: $10[\mu m]\, sin\left(2\pi \times 10[Hz] \times \mathrm{t[s]} - \frac{\pi}{2}\right)$; the $-\frac{\pi}{2}$ phase ensured it started from no extension to minimise discontinuity. These example results were compiled after inclusion of the TELs (k_a=100 GN/m^3 here).

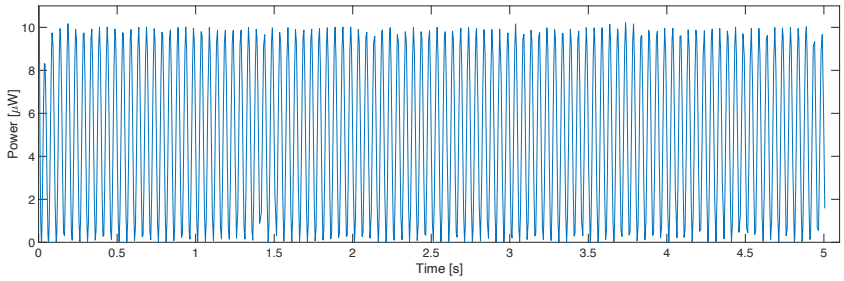

Figure A: Time-domain power output of the plain harvester.

[kk] Unless the mesh of the model was sufficiently dense to require more than the available RAM to process, in which case it could be as much as 20 minutes or more as it progressively consumed more hard drive space for memory; if this too overflowed, COMSOL would crash.

Table a: Simulated cycle power output from each design, comparing time domain and frequency domain analyses.

	Power from Domain Analysis [μW]	
Model	*Time*	*Frequency*
Auxetic	*66.244*	*67.061*
Plain	*5.260*	*5.165*

As can be seen from these results, the difference in power output is minimal. What small differences there are can be accounted for through the mismatch between the peaks and troughs of the excitation with the calculated values of *t*, which could shift the average. Slightly different timesteps could lead to a small change in the overall cycle power. Frequency domain analysis was much more consistent.

A.I.ii. The Need for Thin Elastic Layers

In most of the preliminary work (none of which is included outside this section due to its lack of rigour), the elastic modulus of the epoxy was mistakenly entered into COMSOL as '1e6' N/m^2; not '1e9' N/m^2 as it should have been. This mistake was only found after the proof of concept substrates had been manufactured and tested with some PZT from the research group's stores. One reason this was not spotted earlier was that the power output results were within expectations and the experimental results were actually quite close to those found from this model. When the error was identified and corrected, the modelled power output became far too high to be considered plausible (>1.5 mW from a 10 μm excitation of a thin 2 cm square of PZT would have been optimistic even with an auxetic substrate; the plain baseline would supposedly reach around 0.6 mW under these conditions), and the calculated stress in the piezoelectric layer was untenable (nearly 200 MPa in auxetic case; in plain models it approached 20 MPa). This problem was eventually solved through use of COMSOL's Thin Elastic Layers. After these had been implemented the design process restarted, and fortunately the new optimal design was indistinguishable from the previous optimal design found without them. Before arriving at this solution many attempts were made.

9.1.1.1 Glue Thickness

Initially it was thought that any discrepancy between the model and its experimental equivalent would be the thickness of the glue, this being rather hard to control while manufacturing the sample harvesters. Here in Figure B are the simulated sweep results both before and after correcting the epoxy's elasticity, as described previously.

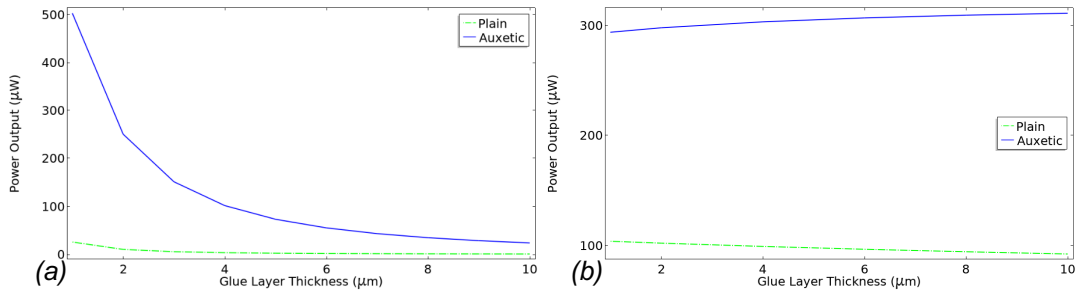

Figure B: Models without TELs, showing thickness sweep results using the (a) uncorrected and (b) corrected epoxy material. 10 Hz, 100 με (4 μm) excitation.

As might be expected, the glue layer being thinner transfers more of the applied strain into the piezoelectric layer and so its power output is higher. That is with the exception of the auxetic model once corrected, where there is a slight increase with thicker glue (this does eventually come back down, but only with an implausibly thick layer of ~1 mm or more). Why this should be opposite to the plain model is difficult to ascertain; possibly the slightly greater leeway allows the outward flexing corners of the structure a little more range to expand. Both corrected models are however quite flat, and so adjusting this variable to more accurately emulate the experiment seemed unfeasible.

9.1.1.2 Preliminary PZT Results

The preliminary version of the experimental proof of concept work used PZT-5H, left over from Pozzi's work[56]. This material had been in a drawer ever since, and was quite old. Most of the pieces were visibly broken, and their size was predetermined: 20×20×0.2 mm (10×10×0.2 mm was also available, but this was deemed too small to build a viable re-entrant hexagon design under). The experimental results were far from an exact match with the model, but by using the parametric sweep of the glue thickness (within the bounds of what could be measured on the samples with a calliper, model results in Figure B) it was reasonable to match the output level if not at the same optimal load resistance.

When the aforementioned error with the epoxy was found and corrected, the model no longer approximated the experiment. There was a reasonable assumption that the issue was the dubious quality of the PZT, and so it was replaced by PIC151 of the same standard size. The results of these can be compared in Figure C. The difference was negligibly small for the plain baseline. While there was a substantial difference for the auxetic samples, the new results were insufficient to explain the disparities to the model.

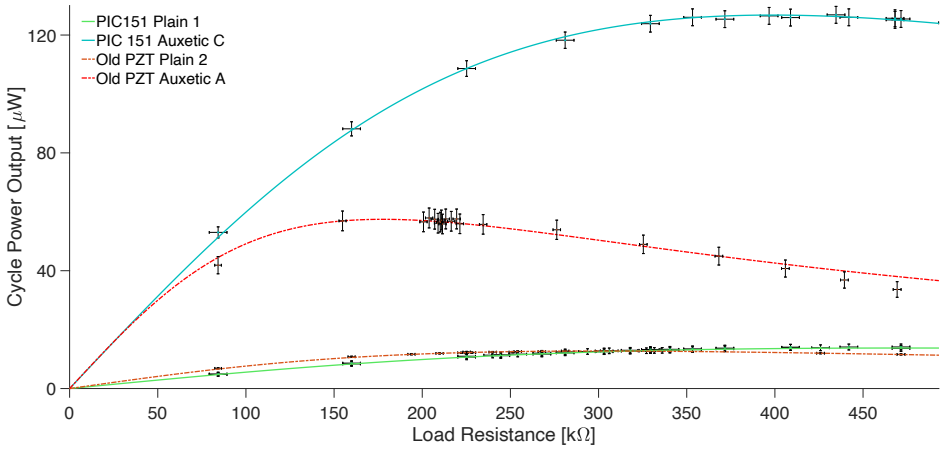

Figure C: Comparison of old PZT to PIC151 (previously shown in Figure 3-13) at an excitation of 10 Hz and 250 με (10 μm).

9.1.1.3 Testing All Available Types of PZT in COMSOL

COMSOL had several different varieties of PZT in its built in materials library. Simulations with each of these materials used for the piezoelectric were run in hopes of identifying the unknown type discussed previously. The difference between these materials proved insufficient to explain the disparity between the simulation and experiment, as indicated in Figure D.

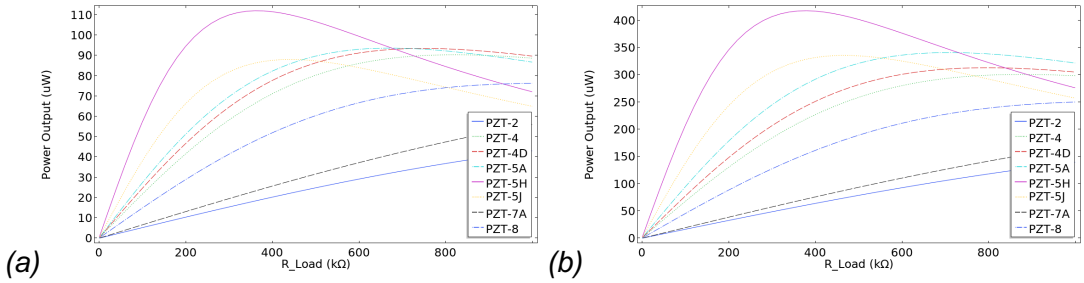

Figure D: Piezoelectric material sweeps on the (a) Plain and (b) Auxetic proof of concept harvesters.

9.1.1.4 Isolated PZT

To ensure the issue did not lie with COMSOL's modelling of piezoelectricity itself, an isolated version of the piezoelectric layer was directly stressed. This was then compared directly to the analytic equation 2–5, as shown in Figure E. This was found to be a perfect match. A similar analytic check on the stress distribution in the isolated plain substrate found the expected result. This confirmed the issue was in the bonding between these parts.

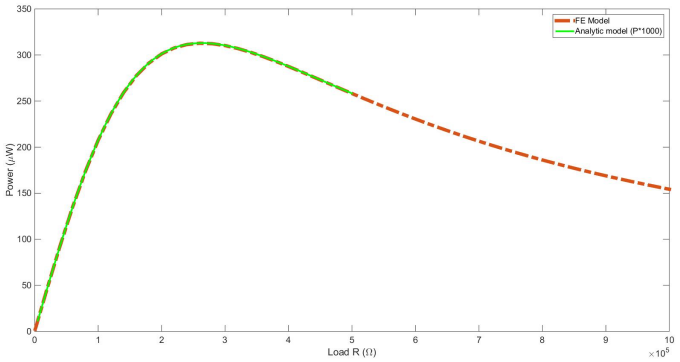

Figure E: Comparison of Finite Element and Analytic modelling of piezoelectricity.

9.1.1.5 Measuring the Epoxy's Elastic Modulus

A sample of the epoxy was clamped until cured between two sheets of plastic to have isolated material for a tensile test. The epoxy was peeled away from the plastic and seven dog-bone shaped samples were cut out. These were tested in an Instron 3367 tensile testing machine, and the results are shown in Figure F. The average gradient for the linear regions of these samples was 1.010 GPa. This was approximated to 1 GPa for the modelling.

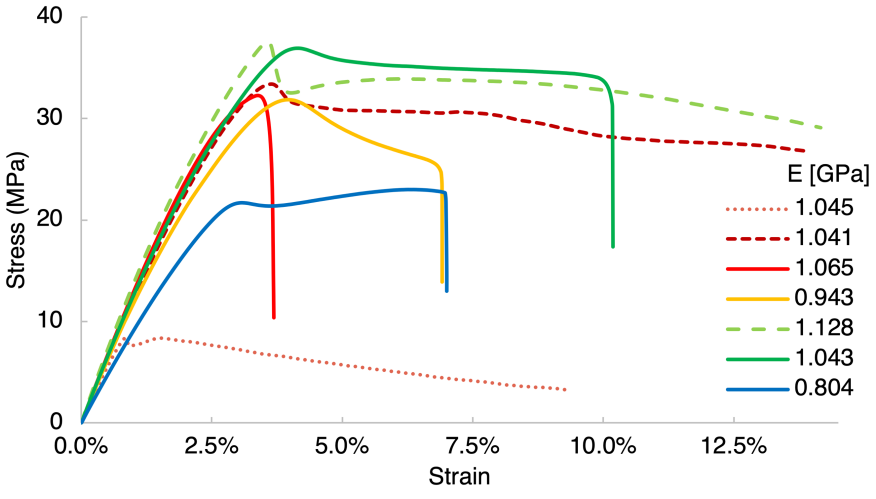

Figure F: Tensile test results of Scotch-Weld™ 460[134] epoxy.

9.1.1.6 Thin Elastic Layers

Thin elastic layers (TELs) are a boundary condition available in COMSOL[II] to emulate layers of material significantly thinner than neighbouring domains without resorting to an uneven mesh element distribution. This can make models run faster by removing dense areas of mesh while maintaining the same mechanical effect between parts. The initial use of this TEL was to replace the epoxy altogether (using the same material data and measured thickness to allow COMSOL to calculate the equivalent stiffness per unit area) which, as designed, produced near identical results to modelling the epoxy layer within the mesh; as shown in Figure G.

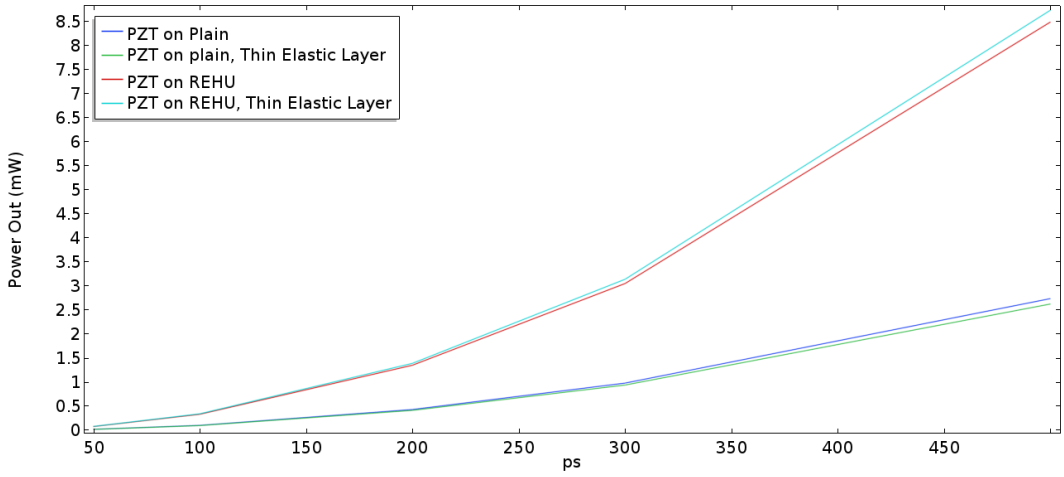

Figure G: Simulations of both proof of concept designs, comparing those with explicit glue layers to models where thin elastic layers replaced this glue.

The TELs were abandoned, until a communication with COMSOL's support suggested using TELs between the epoxy and each of the other components. This gave a single tuneable value to the model to act as a fitting parameter: the spring constant per unit area, k_a. If this value was significantly different in order to match the plain and auxetic samples, then this usage of TELs would have also been abandoned. The first set of values found were listed in Table 3-3. Fortunately these values were all in the same order of magnitude, and the variation between auxetic samples was explainable in terms of the epoxy filling the auxetic structure and causing it to become stiffer to an unpredictable degree. That the same value could be applied to each of the samples under any excitation

[II] Many other available boundary conditions were tried unsuccessfully; either there was no transfer of strain to the piezoelectric layer, or the model failed to start, or there was little difference with them enabled. These failures may be due to using these features incorrectly.

gave further credence to the TELs usefulness. The TELs were used in all subsequent models, with some adjustment to the scale required to emulate the adhesion between different materials, as described in the prior chapters.

These TELs could be used to replace the entire glue layer and include the effects of surface adhesion and variations in the glue's thickness (see below). The reticence to this was that it would discard all information about the epoxy material, and require identifying a new value for every combination of substrate, glue and piezoelectric material (more specifically, that material's under-surface electrode); though that became necessary for each new stage of work in any case, so this would most likely be the best course for any future developments.

9.1.1.7 Glue Thickness with TELs

The thickness of the model's glue layer was initially used as the fitting parameter before identifying the error with its elasticity. With this corrected, the thickness became a less potent means of correcting the model, and with the introduction of the TELs, the variation of the thickness became still less significant; as demonstrated in Figure H.

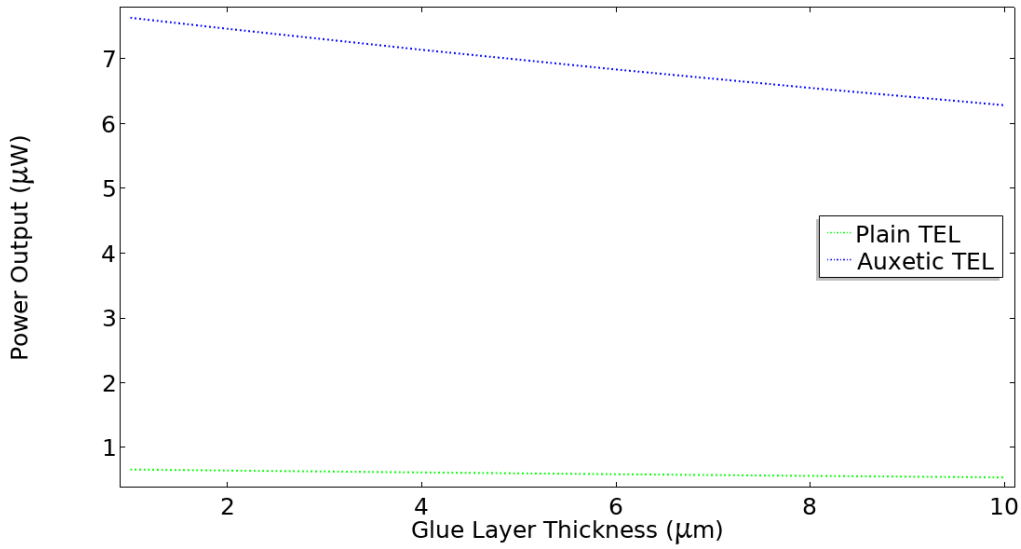

Figure H: Corrected epoxy under PZT-5H with TEL 100 GN/m^3, 100 με, 10 Hz.

A.I.iii. Cross Section Excitation

When the proof of concept designs was excited in the COMSOL simulations, the clamping area's top and bottom surfaces were considered as being the sights of excitation to best emulate the experimental setup. The two faces at one end were set as fixed, and the two faces at the other were given an extension equal to the peak-to-peak displacement of the excitation. Some may consider instead setting the fixed and excited regions in the cross sectional area of the substrate, as indicated in Figure I. The difference between methods was therefore investigated to ensure the effect was small. The other parameters and excitation magnitude in the model were as the final design of the substrate detailed in section 3.1.1, including TELs of 100 GN/m^3.

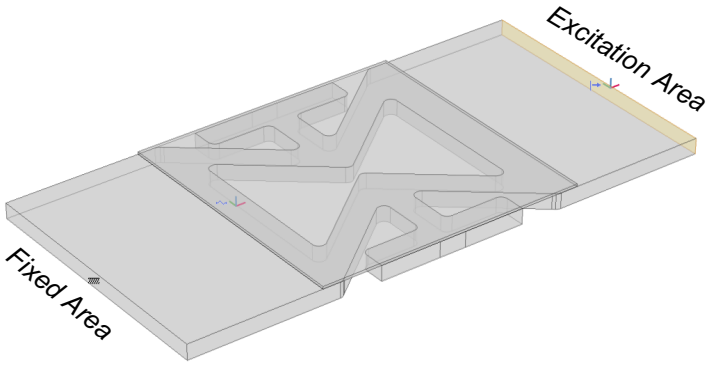

Figure I: Auxetic design without clamping regions; excited cross sections indicated.

Table b: Power output from each design, with surface mounted and cross sectional excitations.

	Power from Excitation Area [μW]	
Model	*Clamping Surfaces*	*Cross Section*
Auxetic	*67.061*	*66.956*
Plain	*5.717*	*5.891*

From Table b, where the excitation is applied can be seen to make little difference. The effect on the plain model is slightly larger because the stress field is less uniform at these cross sectional faces than in the auxetic design (where the stress is concentrated into the auxetic region, see Figure 3-7). As the clamping surface method more closely emulates the experimental setup, this has been selected throughout the work. This more explicit approach is also far more appropriate for the larger harvesters, where their full width does not fit within the width of the Instron clamps.

A.I.iv. Auxetic Piezoelectric Layer

Some of the work listed in the literature review suggest having the piezoelectric layer follow the auxetic shape of the substrate[113]. This was tested using the optimised proof of concept model, at the same excitation and conditions (10 Hz, 10 μm, k_a=100 GN/m^3) used in section 3.1. The piezoelectric layer had the shape of the auxetic substrate, projected through the glue layer. This removed almost half the area of the square PZT layer (and would be quite difficult to manufacture outside a computer model).

The result of this model was only 1.832 μW. Compared to the clamping surface results in table b, the output has been greatly reduced by removing this hanging PZT. The stress in the PZT is shown in Figure J and peaked at 51 MPa, much more than its tensile limit. This kind of design is therefore highly impractical.

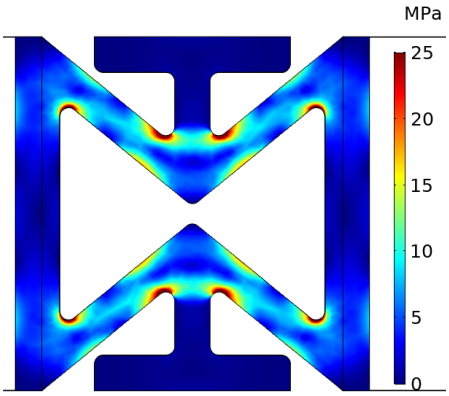

Figure J: Stress concentration in auxetic-shaped PZT. Colour range capped for clarity.

B. Further to Chapter 4

B.I. Test Piece Switch Matrix

To ensure that using the switch matrix did not affect the power output of the sample being tested, one of the plain harvester samples used in chapter 3 was retested. It was excited by the same 10 Hz, 250 με input from the Instron, with the output going through either the manual variable varistor setup described in section 3.2.2 or the switch matrix one discussed in section 4.1.2 (using the resistance values listed in Table 5-6). The results are shown in Figure K. This shows the switch matrix does not affect the measured output; while making the process of taking data much quicker, and thus more reliable and easier to take data from more varied excitations.

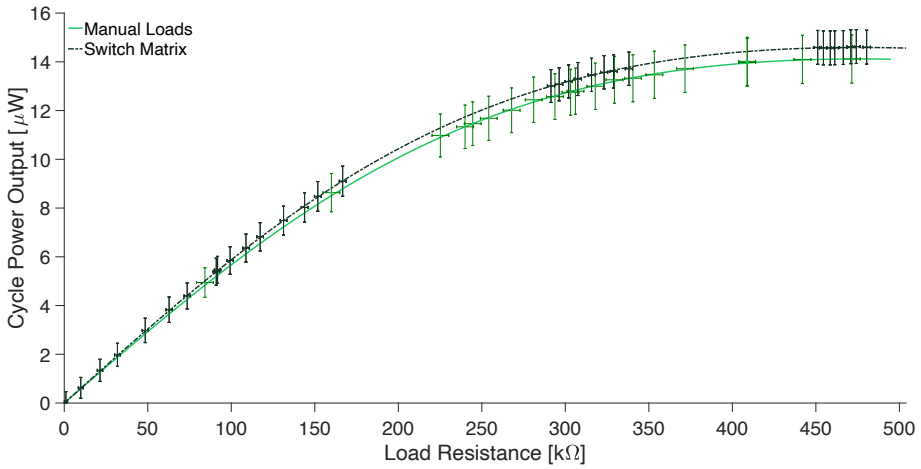

Figure K: The experimental results from Plain 1 sample comparing measurements using the manual variable resistor and switch matrix resistance sweeps.

B.II. Extended Frequency Sweep

The FEMTO-ST group wished to explore applications up to 60 Hz, however the Instron proved less reliable at input frequencies above 30 Hz. The variation in power output in frequencies beyond this were traced to a variation in the force applied to achieve the same displacement; the more force was necessary the greater the power output. A similar pattern in both the plain an auxetic samples as to which frequency was over or under performing our expectations can be seen in figure L. Most of these deviations are not due to the difference between these substrates but primarily the testing apparatus. Both 55 Hz results demonstrate this, as the Instron applied much less force to the samples and the power output is accordingly below expectations.

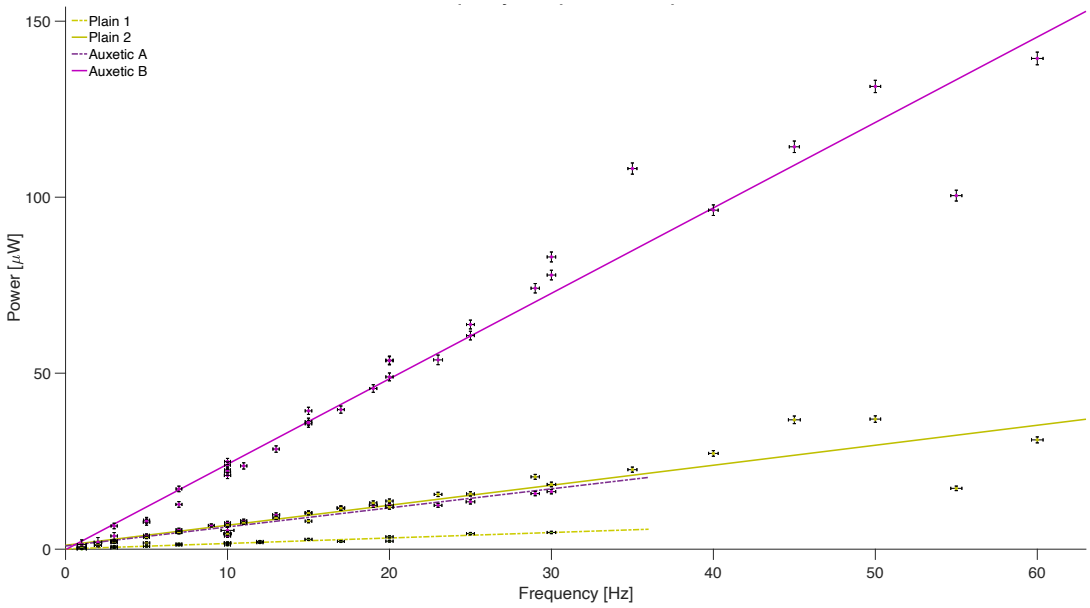

Figure L: Additional higher frequency results to extend Figure 4-7

C. Further to Chapter 5

C.I. t_p on Different Auxetic Regions

As a piece of preliminary work for the larger auxetic region in chapter 5, the relative effect of the thickness of the PZT on 36 different re-entrant honeycomb substrate designs was tested (following the setup discussed in section 5.1, with k_a of 200 GN/m^3 in the TELs and PZT layers). This was to find out if the results would be consistent; i.e. would a design that worked well with one thickness also work well with a thicker piece of PZT (in case the intended one was unavailable). The 36 models gave one for each $M \times N$ array, where both M & N are integers in the range 1-6. Values for the b_t, d & cb parameters for each of these 36 designs were selected arbitrarily to give a reasonable spread of designs (some close packed, some open, others deliberately weak, etc.), while ensuring all were viable designs with no intersections.

The resulting power output, shown in Figure M indicated that the difference is quite small. The trajectories are approximately parallel, especially after the peaks (recall the thickness at the design stage was 180 μm while the thinnest available was later found to be 550 μm). These peaks seem to form two clusters, most peaking at or above 80 μm, with some peaking nearer 50 μm. The latter group is primarily populated by high-M by low-N designs (many units stacked across the substrate, but fewer, stretched-out ones along), though not all of them. This may

indicate that while most designs have the peak PZT stress over the centre of the re-entrant units, these few have more significant contributions from other areas. Even with these outliers, there is little to indicate that an optimised design at one piezoelectric layer thickness would be significantly worse than some other design with the same thickness.

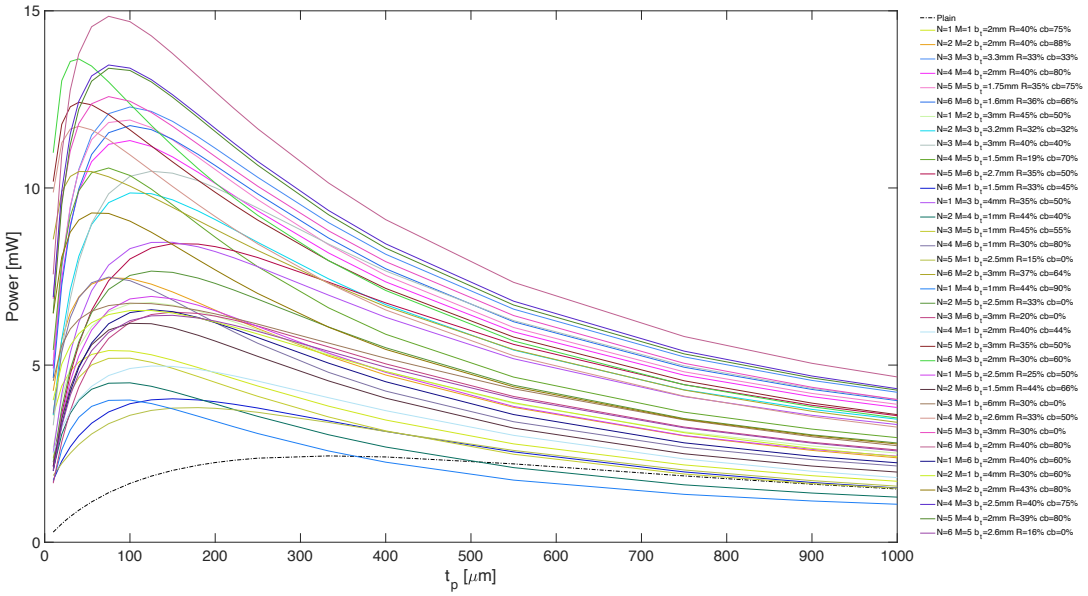

Figure M: Simulated power output from 36 different re-entrant honeycombs with varying piezoelectric layer thickness, t_p. Plain comparison in dot-dashed black.

C.II. TEL k_a on Different Auxetic Regions

To investigate the potential effect of differing values for k_a with various designs, 36 re-entrant honeycomb designs (the same ones as used in appendix C.I) were modelled and tested (according to the setup discussed in section 5.1, with 180 μm thick PZT). This was to find out whether the use of TELs would be consistent across all these different designs; i.e. would a design that was best with one particular k_a value still be the best with some other value. Fortunately, the results shown in figure N demonstrate that there is little relative shifting between models at different values of k_a.

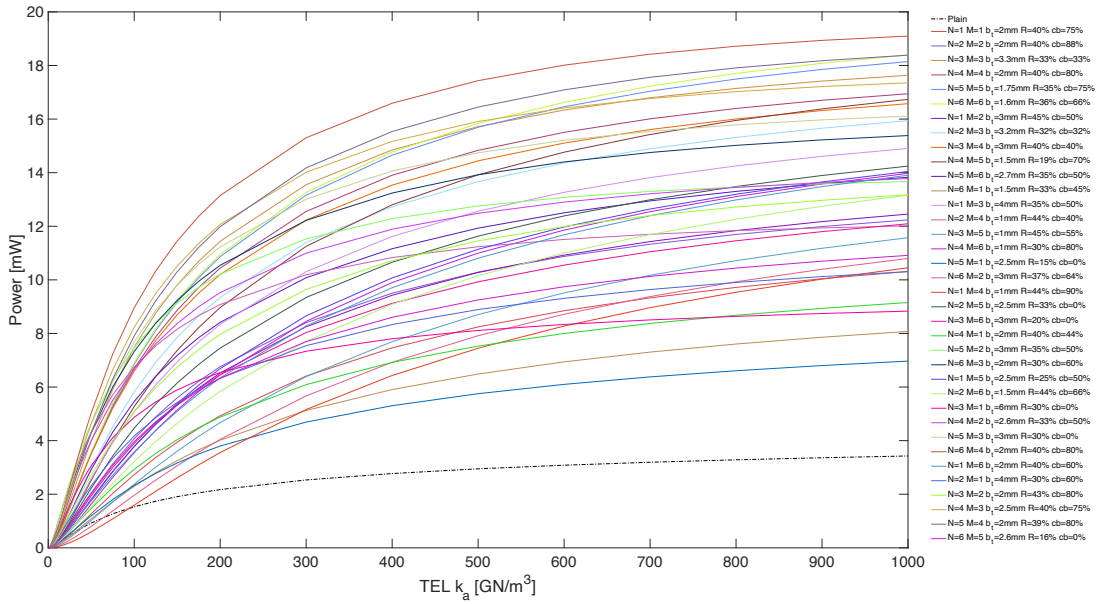

Figure N: Simulation of power output from 36 different re-entrant honeycomb designs against their bonding adhesion strength k_a. Plain equivalent also shown.

Looking at Figure N, the tracks of most of the 36 designs appear parallel. There are a few cross-overs where one design gradually falls short; again, these are all the high-*M* by low-*N* designs. These crossovers indicate that for these designs, increasing the bonding adhesion can't improve their output as much as the other designs. Overall though, these results show that a design that works well with a low k_a still works well with a high one. This effect if therefore sufficiently negligible to relegate its discussion to this appendix.

C.III. Clamping Length

During the experimental work, it was noted that the power output of the samples were higher when the clamping length was shorter. Somewhat paradoxically, less material in the clamps seemed to lead to a better grip. It was observed that only after testing with a clamping depth of around 1 cm were there any noticeable bite marks from the clamps found on the stainless steel, so the same gripping pressure on a smaller area could have been a factor; the clamping depth effect persisted with aluminium substrates however, where bite marks could be observed at any clamping depth, so it was not the only factor. Figure O shows the results of a systematic investigation, comparing equal stains (the solid lines at 100 με) and five equal displacements at a range of clamping depths (which were always the same at both ends) on the PZT Plain sample. The plain

was chosen because the auxetic substrate would be expected to concentrate the larger displacements into the auxetic region and thus increase the output, whereas the plain one would not. The tests and analysis were carried out according to the procedure described in section 5.2.2.

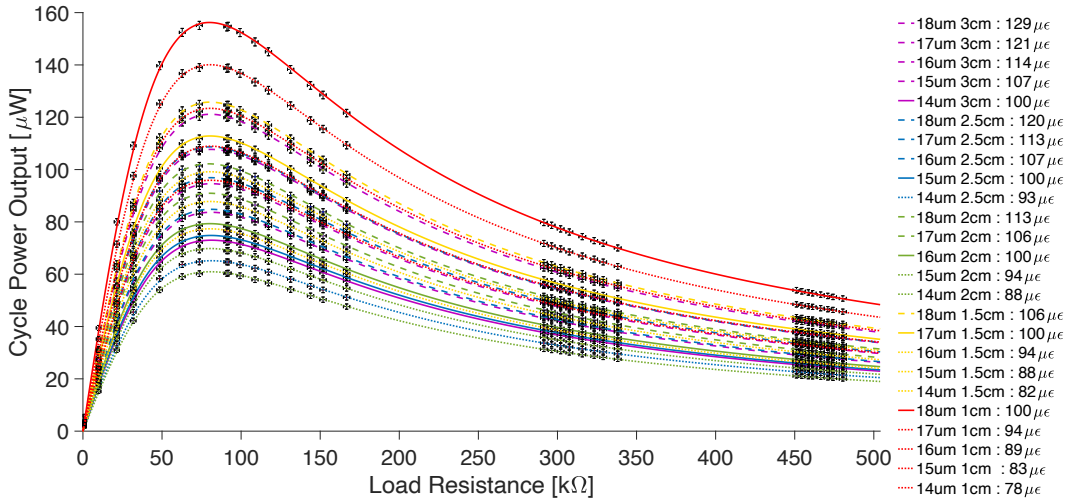

Figure O: Experimental results from PZT Plain at five matching displacements, and a matching strain (100 με, solid line) at five clamping lengths (grouped by colour).

These results show a dramatic increase in equal strain output for 1.5 and 1 cm clamping, while the other three depths all have similar results. The equal displacements at differing depths do not lead to the same outputs. At each clamping depth, the results are as expected however: the higher strain inputs have higher outputs, in their expected orders. Looking at Figure P, we can see the smaller clamping depths result in more uniform displacements across the substrate around the PZT. The larger clamping depths feature increasingly prominent bulges in this area. This non-uniformity is likely the other factor in why the greater clamping distance is less potent. Results like this prompted both the testing of all the samples in chapter 5 at a 1 cm clamping depth, and the 300 mm long substrates in chapter 6. In a practical application, this issue is less likely to arise, as the substrate would be attached to the host structure across its full width; akin to the chapter 3 & 4 samples, which were narrower than the exciting clamps.

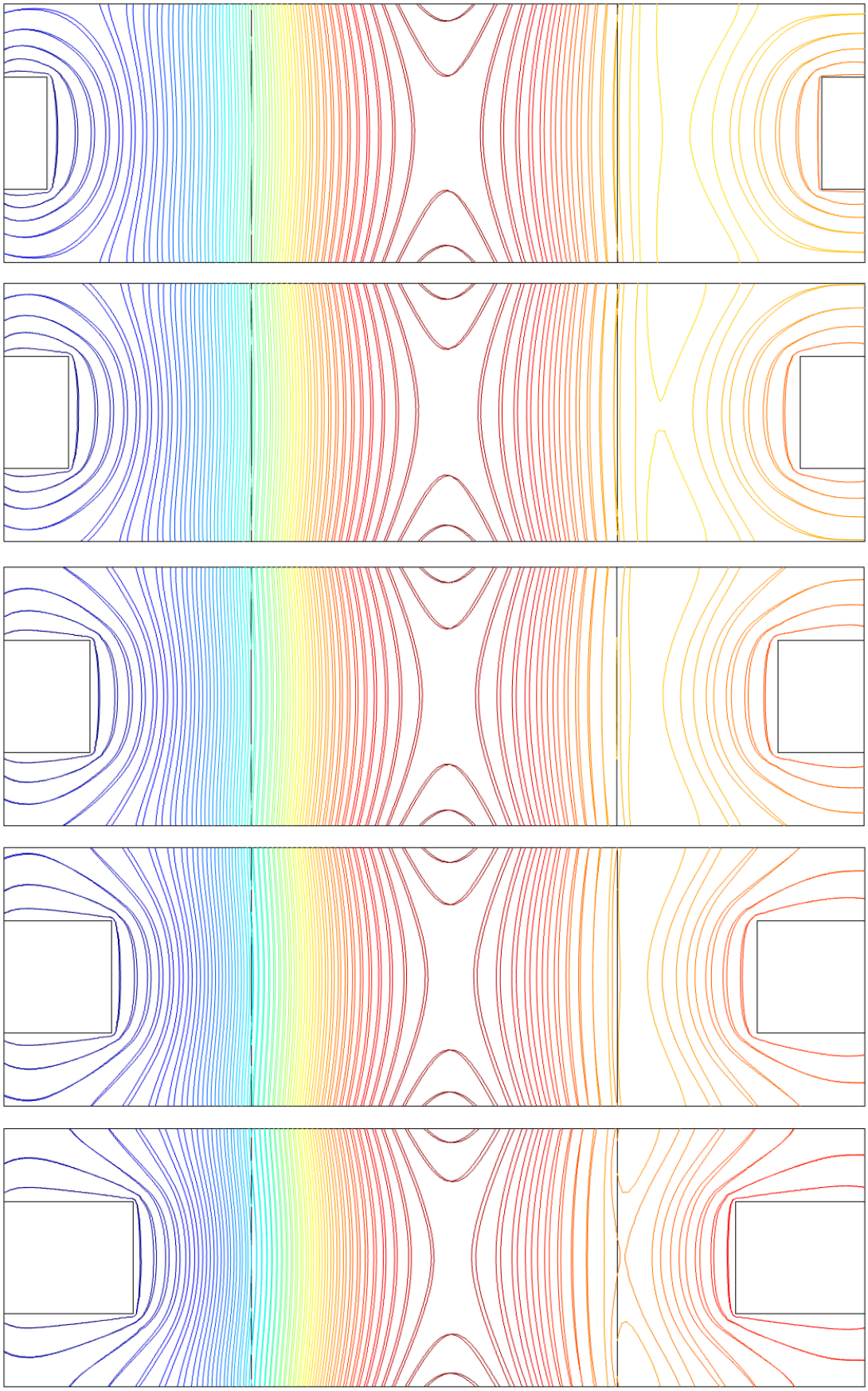

Figure P: Simulated contour maps of displacement at equal strain for a range of outlined clamping depths (1-3 cm) for the Plain PZT sample.

C.IV. Surface Conditioning

A simple way to increase the epoxy's adhesion to the substrate surface might be to make that surface rougher. Sandblasting is a simple way to increase the surface roughness of metals[147]. This was used on a pair of substrates (of the design found in chapter 5) as shown in Figure Q, then MFC was bonded to each and then tested (following the procedure described in section 5.2). The results compared to the equivalent non-sandblasted samples are shown in Figure R.

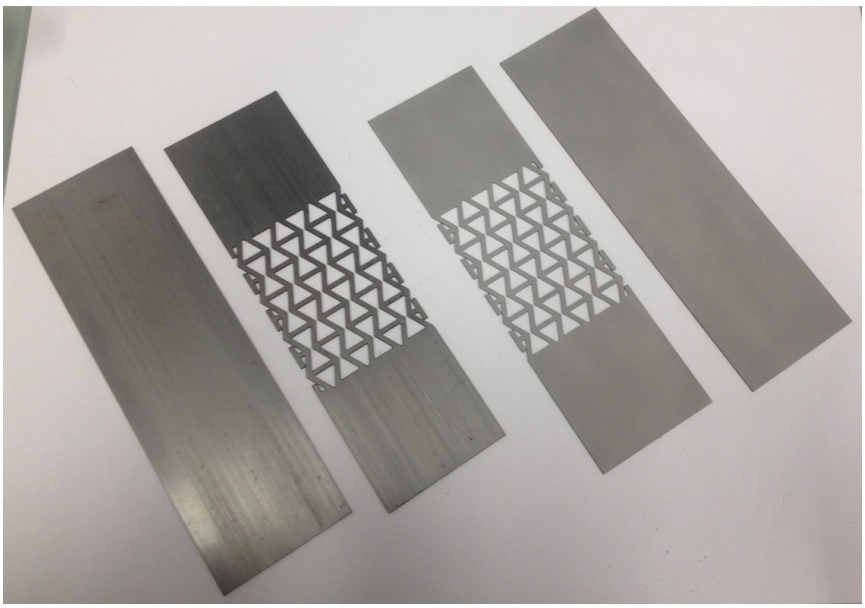

Figure Q: Bare plain and auxetic substrates. The pair on the right have been sandblasted, while the pair on the left have not.

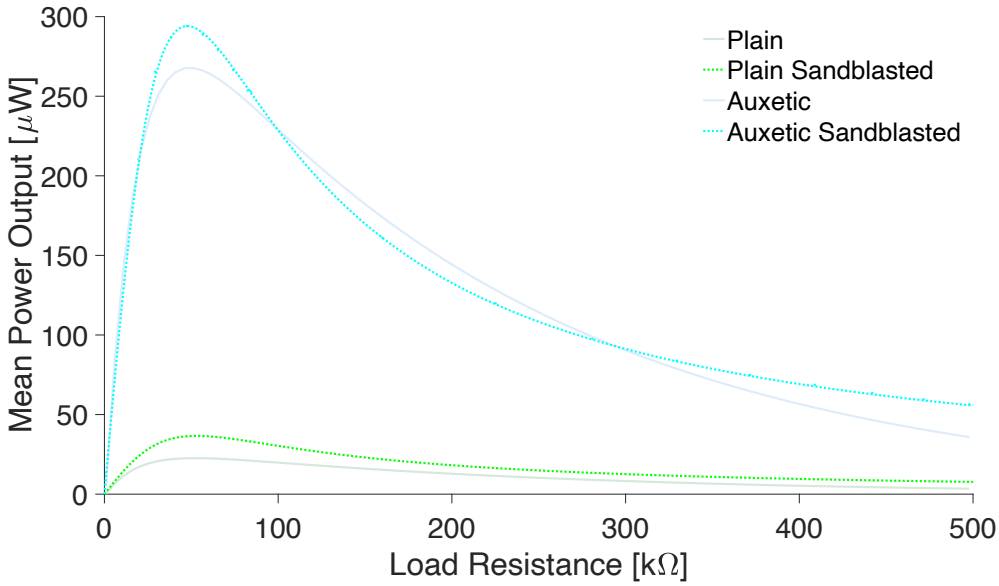

Figure R: Output comparison of MFC samples with untreated substrates against sandblasted ones, at the same 10 Hz, 100 με, all with 2 cm clamping depth.

These results demonstrate that increasing the surface roughness can improve the bonding adhesion, and thus the power output. The plain sample output increases by 63%, while the auxetic sample only gains around 10% on its non-sandblasted version (presumably due to the smaller contact area involved). It is however worthwhile to note that despite the moniker ‘stainless’ steel, after mere months left alone in a drawer (in dry conditions and cool to moderate temperatures) both sandblasted substrates had partially corroded (if superficially) due to the pitted surface; unlike their untreated counterparts held in the same drawer. This suggests that despite a modest increase in output, sandblasting, and many other techniques to roughen the surface, are not worth the likely shortening to the working life of an energy harvester.

C.V. Parametric Sweep Results

The parametric results (with unviable models filtered out) broken up by beam thickness, re-entrancy, and crossbeam fraction give an indication of the range of power outputs there obtained, as shown in Figure S. They also indicate what *M*×*N* array delivers that output range. The best beam thickness here is 2 mm, though this is influenced by the fact that the high *M* & *N* arrays often struggle to fit the thick beams in. A similar story is true of the re-entrant results, as the high outputs come from the most re-entrant units, but at the high end of the 40% column the results become more sparse; again a consequence of the limited space in such small units. The crossbeam fraction results indicate that whenever there is space to put a longer crossbeam, this will increase the power output from the piezoelectric layer.

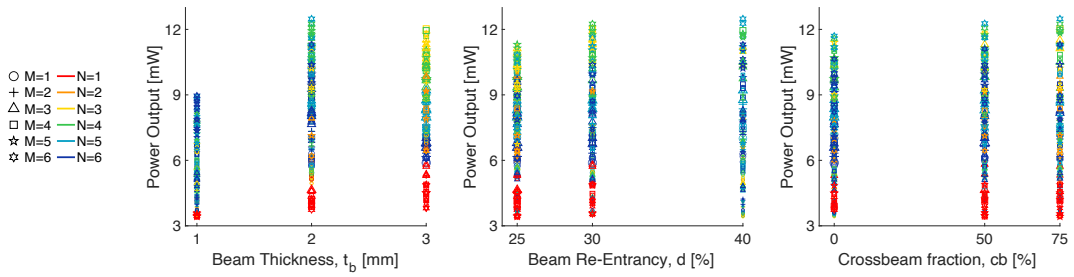

Figure S: Simulated parametric results, with overstressed and unviable models filtered out. The power output is shown compared to the input beam thickness, re-entrancy, and crossbeam fraction respectively. M×N array indicated by shape and colour of the marker.

C.VI. Analytic Model

While working on the large re-entrant honeycomb array harvesters, it was suggested that an analytic model might be much faster than a finite element model. Utilising the relationships derived by Masters and Evans[111], listed in equations C–1-5, the effective Young's Modules and Poisson ratio, along with the contact area of the auxetic region using equation C–6, were calculated for all the models in the parametric sweep, and some optimisation paths, covered in section 5.1. The former are shown on a 3D scatter plot in Figure T. A similar result for the raw parameters explored on some optimisation paths is shown in Figure U. These results show highly non-linear distributions in both cases, indicating that the designing of constrained auxetic regions for this purpose cannot be adequately predicted by analytical modelling.

$$E_{eff} = \frac{1}{\frac{t_b \cos\alpha}{h/l + \sin\alpha}\left[\frac{\cos^2\alpha}{K_f} + \frac{\cos^2\alpha}{K_h} + \frac{2h/l + \sin^2\alpha}{K_s}\right]} \quad \text{Eq.C–1}$$

$$\nu_{eff} = -\sin(\alpha)\,(h/l + \sin\alpha)\left[\frac{-\frac{1}{K_f} - \frac{1}{K_h} + \frac{1}{K_s}}{\frac{\cos^2\alpha}{K_f} + \frac{\cos^2\alpha}{K_h} + \frac{2h/l + \sin^2\alpha}{K_s}}\right] \quad \text{Eq.C–2}$$

$$K_f = E_{Al}\, t_s \left(\frac{t_b}{l}\right)^3 \quad \text{Eq.C–3}$$

$$K_h = \frac{E_{Al}}{2+2\nu_{Al}}\, t_s\, \frac{t_b}{l} \quad \text{Eq.C–4}$$

$$K_s = E_{Al}\, t_s\, \frac{t_b}{l} \quad \text{Eq.C–5}$$

$$A_{REHA} = 2\,M\,t_b(N(h+2l) + CB + def) + 2\,L_{buf}\,W_s \quad \text{Eq.C–6}$$

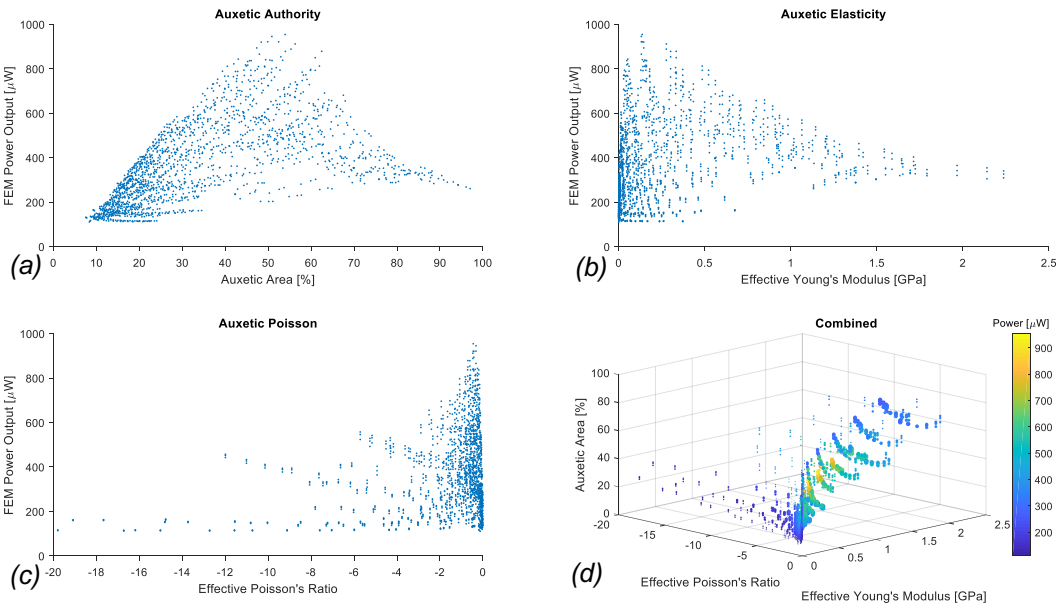

Figure T: Results of the parametric sweep, broken up by power from (a) area, (b) effective elasticity and (c) effective Poisson's ratio of the auxetic region. (d) shows these three axes combined with power indicated as the colour of the points.

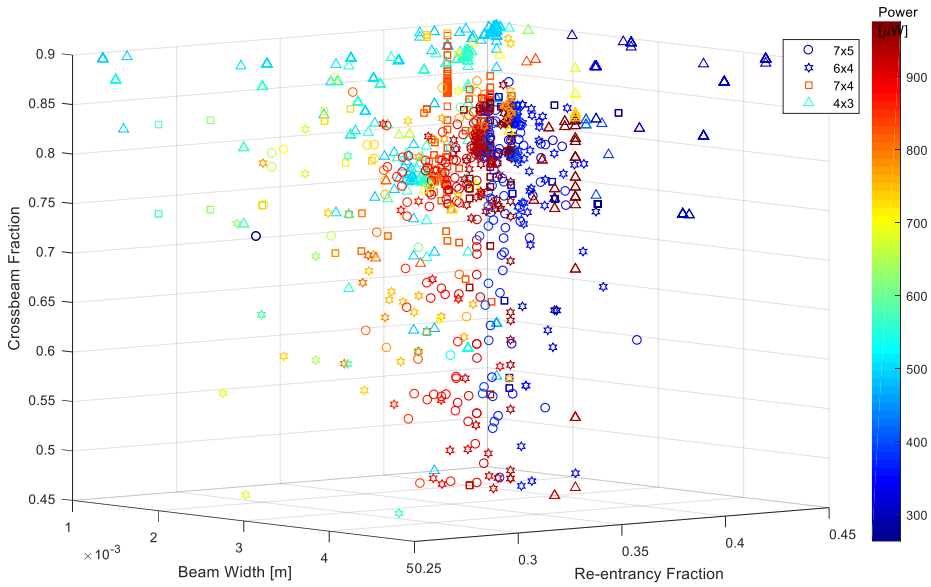

Figure U: Power output from varied model inputs for all optimisation routes from the four best M×N designs.

Some of these results may not have been immediately expected, such as the maximum power output occurring for only slightly negative Poisson ratios, and diminishing at more negative ones. This can be explained by looking at Figure T(d), where the more negative Poisson ratios are accompanied by smaller surface areas with particularly low elasticity; together these limit how much of that increased lateral strain can be imposed on the piezoelectric material, and thus

there is little power gained from the extremely auxetic designs. There is nothing particularly intuitive about where the optimum balance is, simply from the relative values of the input parameters. The region with models of the highest output is interspersed with many inappropriate models with much lower power outputs, so simply having a value within that 'optimal' region is insufficient to predict a successful model.

It is worth noting some limitations of the model used here. The Masters and Evans[111] equations assume a large area of honeycomb, and don't consider edge effects. They also don't consider any constraining layer on the honeycomb, as is the case here. Both of these are significant oversimplifications in this case. Fixing these analytically by forming the honeycomb from a specified number of hinged beams, all in known positions, leads to what is effectively a very course finite element model. Under this regime, any advantages of a general analytic model are lost. This attempt was thus abandoned at this point.

D. Further to Chapter 6

D.I. Plain Comparison to Carbon Fibre

The long plain substrates from section 6.1 were the same area (of substrate and the standard narrow MFC size) as some carbon fibre substrates our group had previously worked upon[44,56,88,138]. Comparisons of stainless steel and aluminium to carbon fibre can thereby be drawn, though the latter is too brittle for auxetic designs; hence relegation to this appendix. The carbon fibre samples had aluminium clamps at each end, as seen in Figure V(a), so the Instron's grips would not fray the fibres. It was thought this may be a worthy addition to the metal ones too, see Figure V(b). The output from each case is shown in Figure W.

(a) 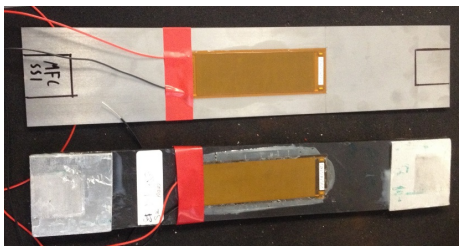 (b) 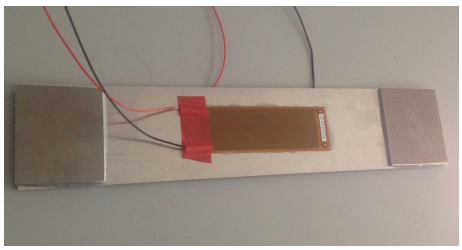

Figure V: Photographs of the 300 mm long substrates, showing (a) stainless steel (left), carbon fibre and (b) aluminium with clamps. Both metal samples were previously shown in Figure 6-2.

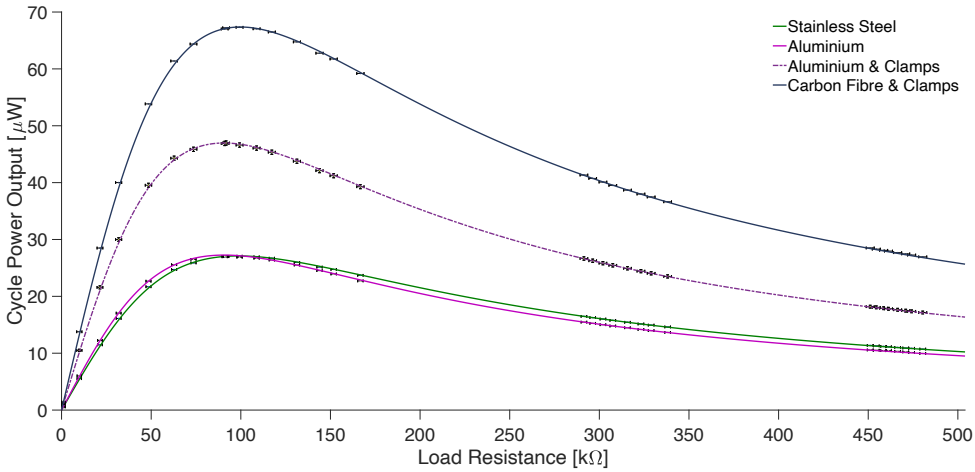

Figure W: Experimental results from three plain substrates of different materials, all subjected to 100 με (25 μm) 10 Hz excitations. The first two datasets were in Figure 6-3.

Placing clamps on the aluminium appears at first glance to be highly beneficial, however considering that the free region of the substrate between the clamps is now shorter, the strain there is then approximately 1.25 times higher (from the same given displacement). Using this and assuming a quadratic relation between power and strain amplitude, the power output at optimal load can be estimated to increase from 27 to 42 μW; this was born out in Figure W. This effect will be at least part of why the carbon fibre substrate generates more power (alongside its much greater thickness giving more authority over the MFC, and its rougher surface allowing greater adhesion to the epoxy).

D.II. Regular Honeycomb

It was thought of interest to compare the auxetic honeycomb, discussed in section 6.2.2, to a non-auxetic honeycomb; to ensure the increased power came from it being auxetic and not merely from the reduced stiffness in that substrate

region. To test this, a regular honeycomb frame was modelled to fit into the auxetic region. This was built from a repeating regular-hexagonal loop, shown in Figure X, where the controlling parameters were the overall size of the hexagons, determined by the number of units that fit along the substrate axis, *N*, and the thickness of their beams, t_b. Note that as this design lacks any crossbeams at the edges, *N* no longer had to take on an integer value. The only other constraints were that *N* had to be at least 2, and t_b couldn't become too large[mm].

There were two approaches taken to this design. The first was to perform a parametric sweep and then optimise from the best of those results, as usual; the other was to calculate parameters that would closely match the auxetic honeycomb design in terms of effective stiffness.

With only two parameters to this design, the parametric sweep could quickly plot the design space; shown in Figure Y. This displays a ridge of higher power results that curves around from high-t_b with low-*N*, to low-t_b with high-*N*; either side of which the output falls off (models where both inputs are high are physically impossible). The best parametric result, $N = 4$, $b_t = 5$ mm, was then the starting point for the optimiser (ranges given in Table c). This easily came to a stable maximum, listed in Table d and shown in Figure AA(a).

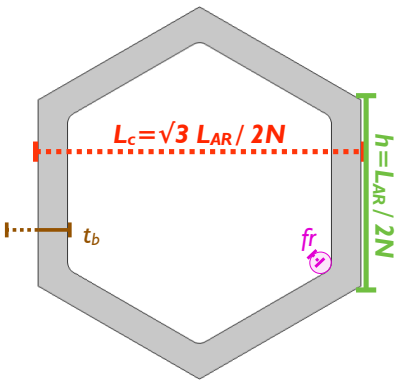

Figure X: Regular hexagon unit with parameters.

Table c: Input values for parametric sweep and optimisation of regular honeycomb.

Parameter [unit]		*Swept Values*	*Opt. Range*
No. of cells in L_{AR}	*N*	*2, 3, 4, 5, 6, 7, 8, 9, 10, 11, 12, 13, 15, 17.5, 20, 25*	*2–33*
Beam Width [mm]	t_b	*1, 2, 3, 4, 5*	*0.5–6*

[mm] The $N \geq 2$ condition was required to ensure there is more than one continuous beam connecting the solid ends of the substrate. The t_b parameter check: $L_{AR}/\sqrt{3}N - t_b/2 < 2fr$ (if true, break) ensured the holes are all larger than a circle 1 mm in diameter. E.g. if the beams are 1 mm thick, this limits N to a maximum of 31; while if $t_b = 4$ mm, *N* is limited to <16.

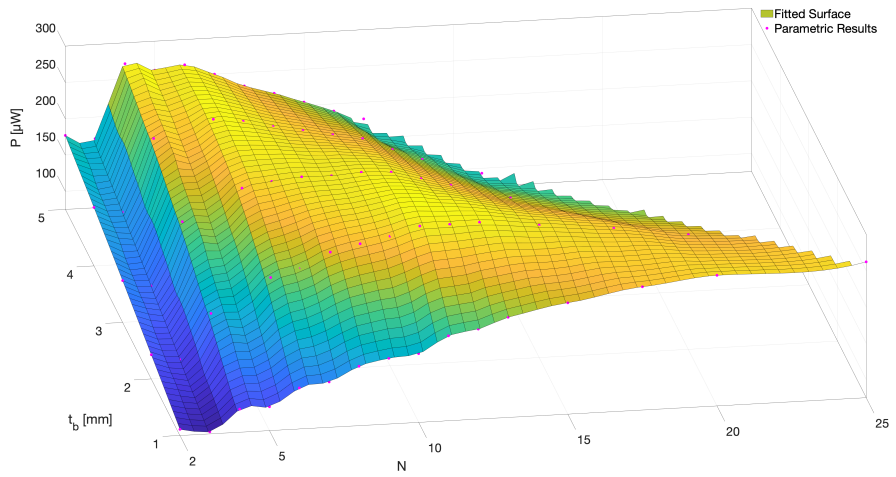

Figure Y: Interpolated surface from regular honeycomb parametric sweep results.

The second method used equation C-1 adapted from Masters and Evans[111] to calculate the effective Young's modulus of the selected re-entrant honeycomb, and then reverse engineered the parameters for the best matching regular honeycomb in terms of effective Young's modulus, E_{eff}. These parameters were then used to model the power output from that design. For the re-entrant honeycomb: $l = L_C \sec(\alpha)/2$ (length of the re-entering beams), $h = H_c$ and α is negative to denote its re-entrancy. For the regular honeycomb: $l = h = L_{AR}/2N$ (all unit side lengths) and $\alpha = +30°$. Remaining terms were defined in Table 5-3 (for re-entrant parameters: α, L_{AR}, L_c, & H_c), and in chapter 6 (the aluminium properties E_{Al} & ν_{Al}, and the substrate thickness, t_s).

From equation C-1, the selected re-entrant honeycomb had a very low effective Young's modulus of 77.2 MPa. A broad spread of datapoints for regular honeycombs was generated from equation C-1, and a surface of their effective Young's moduli plotted in Figure Z. Comparing this to a flat surface representing the target re-entrant value showed a small family of possible matches to be found at the intersection. These solutions were all at the edge of the available range, limiting the choice of design. Ideally one with a similar area or Poisson's ratio (in value but of opposing sign) to the selected re-entrant design would have been picked, but such were unavailable. In order to keep sufficient units and beam thickness, N = 2.4, t_b = 1.5 mm was selected as a balance between the two parameters. Putting these into COMSOL found the power output to be 100 μW, see Table d; even lower than the plain baseline. Comparing to Figure Y, a similarly low output persists for any other model in that region. This demonstrates that the greater elasticity of the auxetic designs is not the only reason for the increased power output of the piezoelectric layer atop them.

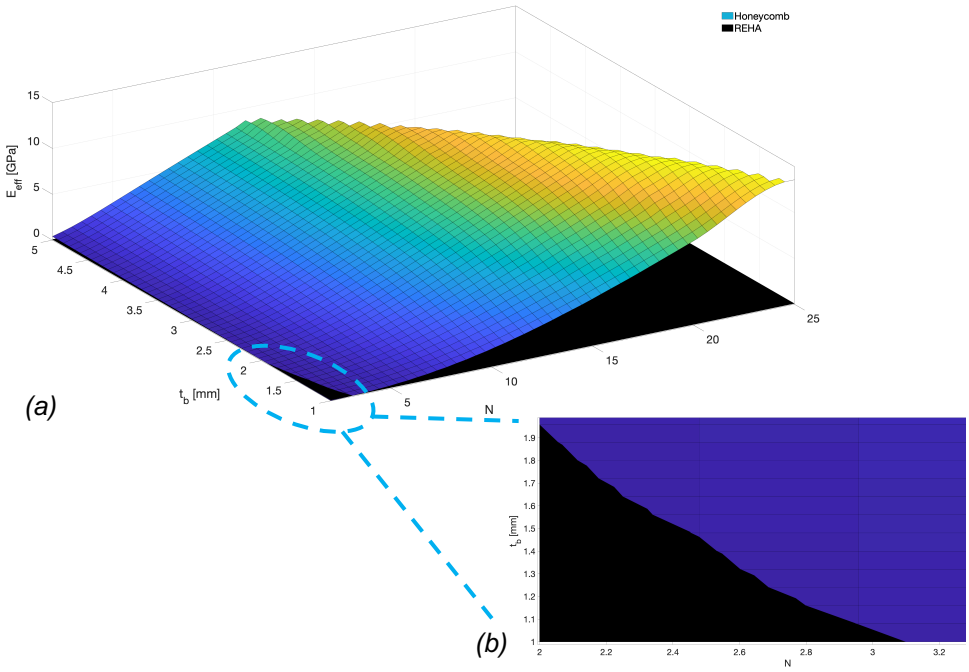

Figure Z: (a) Effective Young's modulus of regular compared to selected auxetic honeycomb (Figure 6-7), based on equation C–1. (b) Closeup of overlapping region.

Table d: Simulation outputs from both regular honeycomb building methods.

Honeycomb Method	Inputs		Power [μW]	Peak Stress [MPa]	
	N	t_b [mm]		Substrate	Piezo
Optimised	18.16	1.433	269	77	4.3
E_{eff} Match	2.4	1.5	100	57	3.8

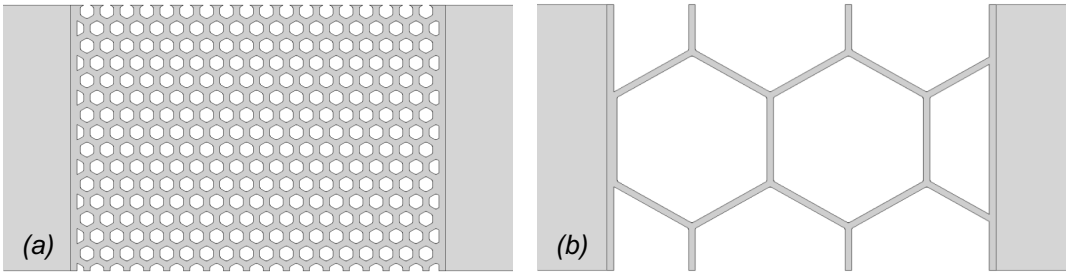

Figure AA: Regular honeycomb designs, from (a) Optimisation, & (b) Matching E_{eff}.

Equations C–1-5 assume no significant edge effects and no constraining layers (especially not only on one side, as is the case for these harvesters). Both auxetic and regular honeycomb models deviate from these assumptions, so these equations are likely a poor approximation to the finite element models. Despite the FEM being much more time consuming, it is the only method that is sufficiently accurate to be of use.

Both of these methods demonstrate that the gain found by using the auxetic substrates is not due to their reduced stiffness alone, but specifically due to them being auxetic. There is no indication that any regular honeycomb design could

come close to being as effective for these energy harvesting purposes as the re-entrant honeycombs. Neither of these regular honeycomb designs were considered sufficiently promising to test experimentally.

D.III. Parametric Sweep Results

The parametric results of all the model sweeps are here broken up by parameter to show the power output is shown compared to each of the input parameters. This shows the range of impact that each parameter can have. Overstressed and unviable models have been filtered out, apart from the hexagram results.

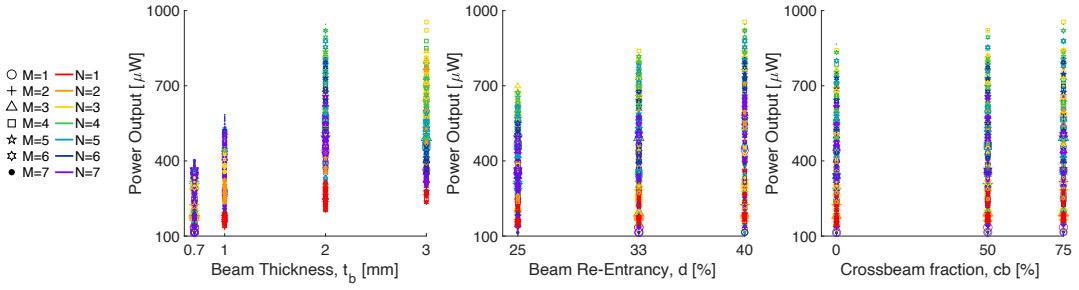

Figure BB: Parametric results for the re-entrant honeycomb design from Table 6-1. M×N array indicated by marker shape and colour.

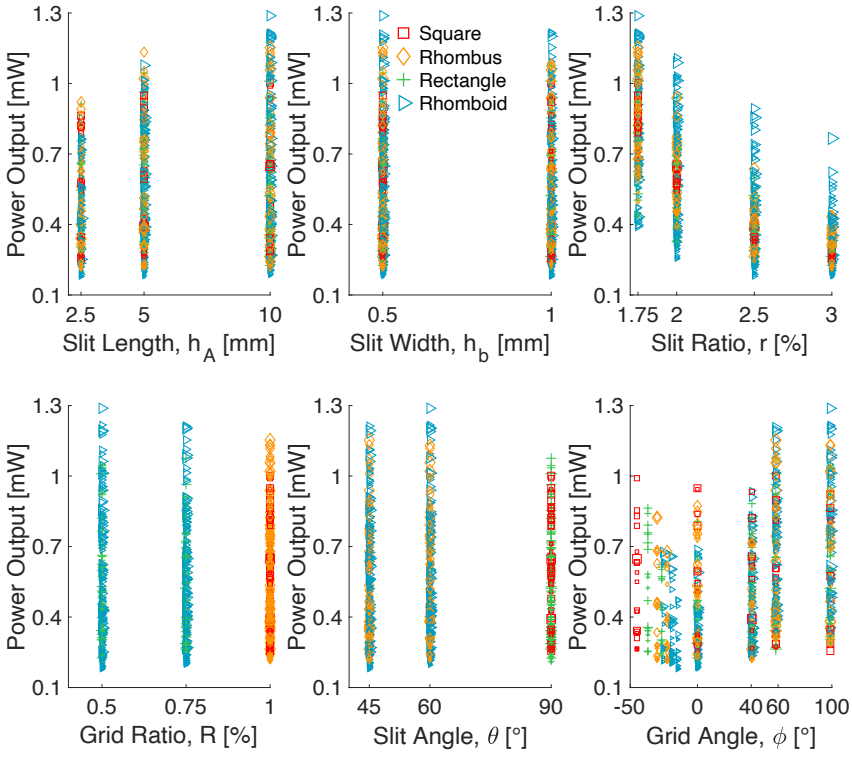

Figure CC: Parametric sweep results for the rotating parallelograms, from Table 6-3. Rotating unit shape indicated by marker.

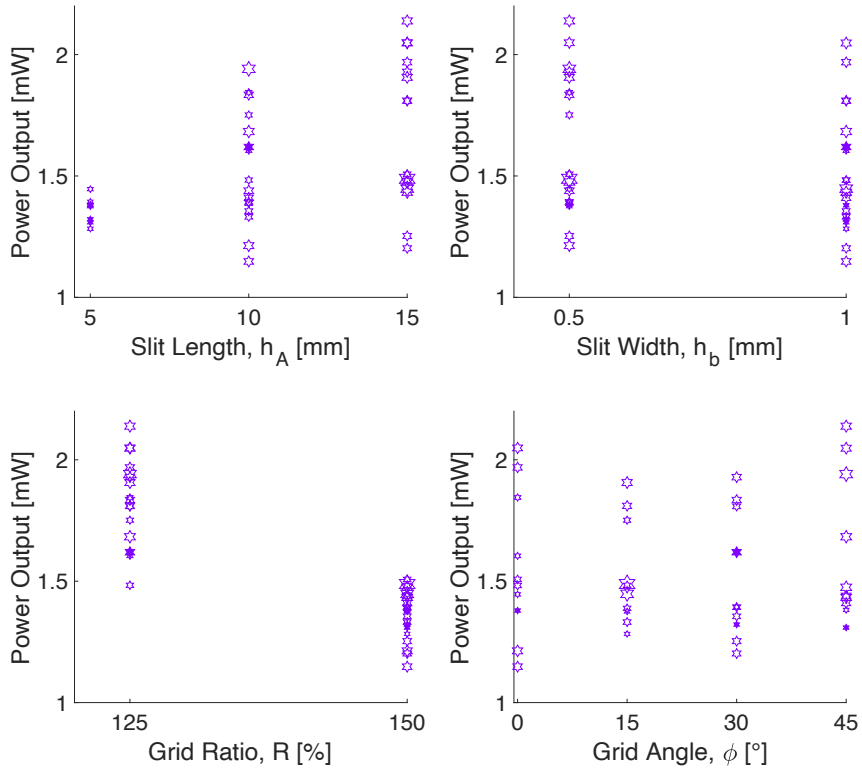

Figure DD: Parametric sweep results for rotating hexagrams, from Table 6-6.

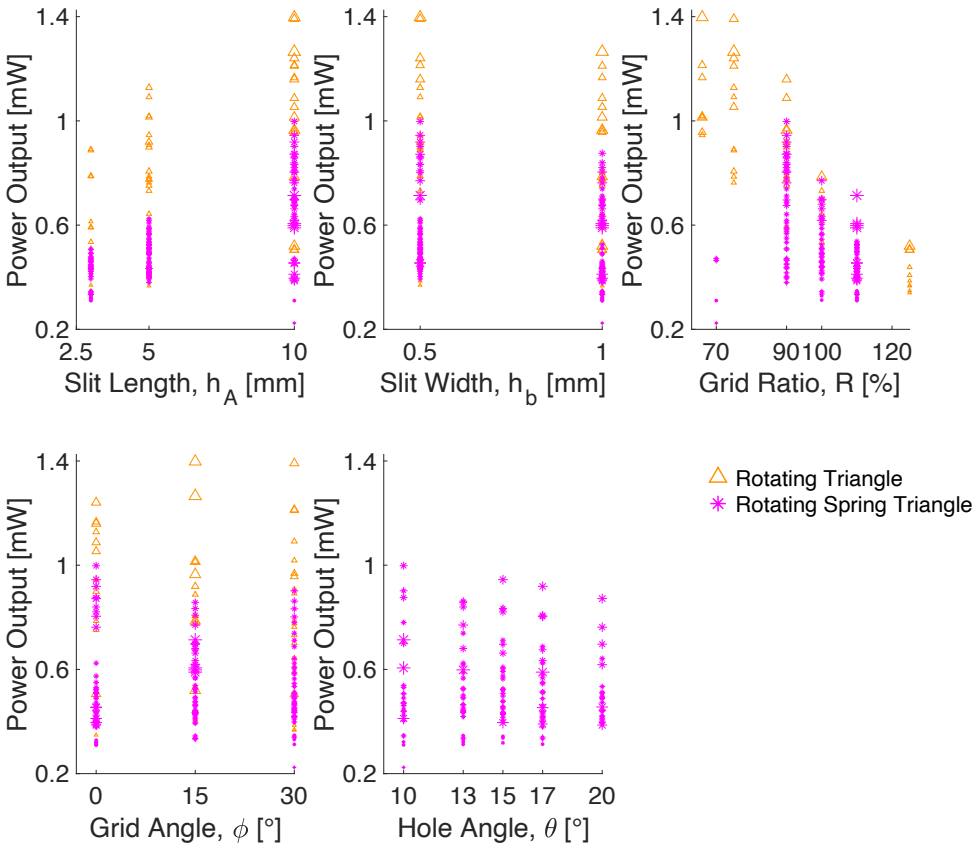

Figure EE: Parametric results for rotating (spring) triangle designs, from Table 6-8.

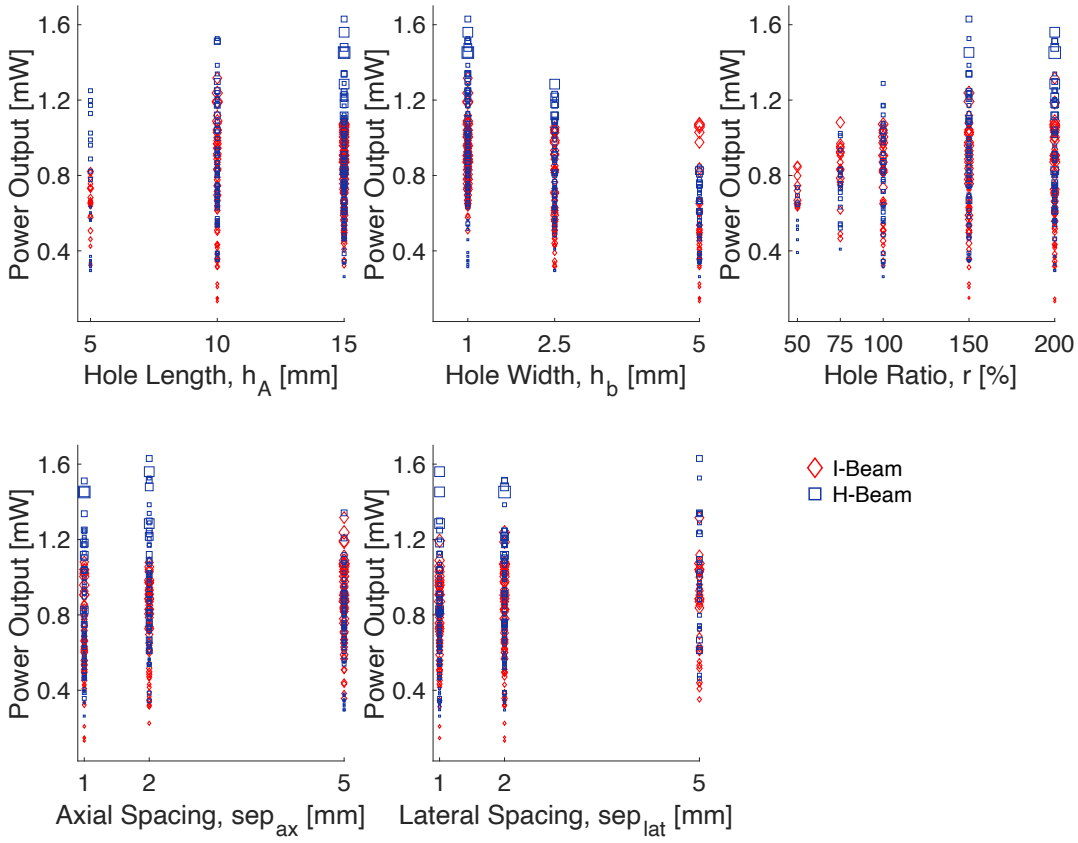

Figure FF: Parametric results for I-hole designs, from Table 6-10.

References

1. Ferguson, W. J. G., Kuang, Y., Evans, K. E., Smith, C. W. & Zhu, M. Auxetic structure for increased power output of strain vibration energy harvester. *Sensors Actuators A Phys.* **282**, 90–96 (2018).
2. Kong, L. B. *et al. Waste Energy Harvesting: Mechanical and Thermal Energies*. **24**, (Springer, 2014).
3. Selvan, K. V. & Mohamed Ali, M. S. Micro-scale energy harvesting devices: Review of methodological performances in the last decade. *Renew. Sustain. Energy Rev.* **54**, 1035–1047 (2016).
4. Chen, Z., Guo, B., Yang, Y. & Cheng, C. Metamaterials-based enhanced energy harvesting: A review. *Phys. B Condens. Matter* **438**, 1–8 (2014).
5. Priya, S. & Inman, D. J. *Energy harvesting technologies*. *Energy Harvesting Technologies* (Springer, 2009). doi:10.1007/978-0-387-76464-1
6. Bowen, C. R., Topolov, V. Y. & Kim, H. A. *Modern Piezoelectric Harvesting Materials*. (Springer, 2016). doi:10.1007/978-3-319-29143-7 Library
7. Pozzi, M. & Zhu, M. Plucked piezoelectric bimorphs for energy harvesting. *Adv. Energy Harvest. Methods* 119–140 (2012). doi:10.1007/978-1-4614-5705-3_5
8. Mescia, L., Losito, O. & Prudenzano, F. *Innovative Materials and Systems for Energy Harvesting Applications*. *Innovative Materials and Systems for Energy Harvesting Applications* (2015). doi:10.4018/978-1-4666-8254-2
9. Shi, Y., Hallett, S. R. & Zhu, M. Energy Harvesting behaviour for Aircraft Composites Structures using Macro-Fibre Composite: Part I – Integration and Experiment. *Compos. Struct.* (2016). doi:10.1016/j.compstruct.2016.11.037
10. Elvin, N. & Erturk, A. *Advances in Energy Harvesting Methods*. (Springer, 2013).
11. Bowen, C. R., Kim, H. a., Weaver, P. M. & Dunn, S. Piezoelectric and ferroelectric materials and structures for energy harvesting applications. *Energy Environ. Sci.* **7**, 25–44 (2014).
12. Karimi, M., Karimi, A. H., Tikani, R. & Ziaei-Rad, S. Experimental and theoretical investigations on piezoelectric-based energy harvesting from bridge vibrations under travelling vehicles. *Int. J. Mech. Sci.* **119**, 1–11 (2016).
13. Harb, A. Energy harvesting: State-of-the-art. *Renew. Energy* **36**, 2641–2654 (2011).
14. Priya, S. *et al.* A Review on Piezoelectric Energy Harvesting: Materials, Methods,

and Circuits. *Energy Harvest. Syst.* **4**, 3–39 (2017).

15. Bito, J., Hester, J. G. & Tentzeris, M. M. Ambient RF Energy Harvesting from a Two-Way Talk Radio for Flexible Wearable Wireless Sensor Devices Utilizing Inkjet Printing Technologies. *IEEE Trans. Microw. Theory Tech.* **63**, 4533–4543 (2015).

16. Ye, G. & Soga, K. Energy harvesting from water distribution systems. *J. Energy Eng.* **138**, 7–17 (2012).

17. Jamieson, P. *et al. Energy Harvesting: Solar, Wind, and Ocean*. *Renewable Energy* **2013**, (CRC Press, 2013).

18. Abdelkefi, A. Aeroelastic energy harvesting: A review. *Int. J. Eng. Sci.* **100**, 112–135 (2016).

19. Chew, Z. J., Tuddenham, S. B. & Zhu, M. Airflow energy harvesting for high speed vehicles. in *PowerMEMS 2016* 4–7 (Journal of Physics: Conference Series, 2016). doi:10.1088/1742-6596/773/1/012091

20. Chiu, M. C., Karkoub, M. & Her, M. G. Energy harvesting devices for subsea sensors. *Renew. Energy* **101**, 1334–1347 (2017).

21. Lee, H. J., Sherrit, S., Tosi, L. P., Walkemeyer, P. & Colonius, T. Piezoelectric energy harvesting in internal fluid flow. *Sensors (Switzerland)* **15**, 26039–26062 (2015).

22. Akaydin, H. D., Elvin, N. & Andreopoulos, Y. Energy harvesting from highly unsteady fluid flows using piezoelectric materials. *J. Intell. Mater. Syst. Struct.* **21**, 1263–1278 (2010).

23. Dias, J. A. C., De Marqui, C. & Erturk, A. Hybrid piezoelectric-inductive flow energy harvesting and dimensionless electroaeroelastic analysis for scaling. *Appl. Phys. Lett.* **102**, (2013).

24. Chen, J. *et al.* Personalized Keystroke Dynamics for Self-Powered Human - Machine Interfacing. *ACS Nano* **9**, 105–116 (2015).

25. US Navy; Roberts et al. Energy Harvesting Device using auxetic materials - US 9048761 B1. 8 (2015).

26. Kuang, Y., Daniels, A. & Zhu, M. A sandwiched piezoelectric transducer with flex end- caps for energy harvesting in large force environments. *J. Phys. D. Appl. Phys.* **50**, 1–14 (2017).

27. Boyle, G. *et al. Renewable Energy: Power for a Sustainable Future*. (Oxford University Press, in association with The Open University, 2012).

28. Perpetuum. Perpetuum: Rail Applications. *Perpetuum* (2017). Available at: https://perpetuum.com/rail-applications/. (Accessed: 9th October 2017)

29. Ni, Y.-Q. & Xia, Y.-X. Strain-Based Condition Assessment of a Suspension Bridge Instrumented with Structural Health Monitoring System. *Int. J. Struct. Stab. Dyn.* **16**, 23 (2016).

30. Capella, J. V., Bonastre, A., Ors, R. & Peris, M. A step forward in the in-line river monitoring of nitrate by means of a wireless sensor network. *Sensors Actuators, B Chem.* **195**, 396–403 (2014).

31. Arafa, M., Akl, W., Majeed, M., Al-Hussain, K. & Baz, A. Energy harvesting of gas pipeline vibration. *Act. Passiv. Smart Struct. Integr. Syst.* **7643**, 76430L (2010).

32. Le, M. Q. *et al.* Review on energy harvesting for structural health monitoring in aeronautical applications. *Prog. Aerosp. Sci.* **79**, 1–11 (2015).

33. Yoon, H. J., Song, K. Y., Choi, C., Na, H. S. & Kim, J. S. Real-Time Distributed Strain Monitoring of a Railway Bridge during Train Passage by Using a Distributed Optical Fiber Sensor Based on Brillouin Optical Correlation Domain Analysis. *J. Sensors* **2016**, (2016).

34. Kuang, Y., Yang, Z. & Zhu, M. Design and characterisation of a piezoelectric knee-joint energy harvester with frequency up-conversion through magnetic plucking. *Smart Mater. Struct.* **25**, 085029 (2016).

35. Qi, Y. & McAlpine, M. C. Nanotechnology-enabled flexible and biocompatible energy harvesting. *Energy Environ. Sci.* **3**, 1275 (2010).

36. Karami, M. A. & Inman, D. J. Powering pacemakers from heartbeat vibrations using linear and nonlinear energy harvesters. *Appl. Phys. Lett.* **100**, (2012).

37. Shaikh, F. K. & Zeadally, S. Energy harvesting in wireless sensor networks: A comprehensive review. *Renew. Sustain. Energy Rev.* **55**, 1041–1054 (2016).

38. Matiko, J. W., Grabham, N. J., Beeby, S. P. & Tudor, M. J. Review of the application of energy harvesting in buildings. *Meas. Sci. Technol.* **25**, (2014).

39. Yang, Z., Zhou, S., Zu, J. & Inman, D. High-Performance Piezoelectric Energy Harvesters and Their Applications. *Joule* **2**, (2018).

40. gelmi. Carbon Monoxide Detector: The Road So Far. *Element14 Community* (2013). Available at: https://www.element14.com/community/community/design-challenges/energy-harvesting/blog/2013/07/17/carbon-monoxide-detector-the-road-so-far. (Accessed: 22nd August 2017)

41. Ceriotti, M. *et al.* Monitoring heritage buildings with wireless sensor networks: The

Torre Aquila deployment. *2009 Int. Conf. Inf. Process. Sens. Networks* 277–288 (2009). doi:10.1145/1602165.1602191

42. European Commission Business Innovation Observatory. *Clean Technologies: Energy Harvesting*. (2014).

43. Ramakrishnan, M., Rajan, G., Semenova, Y. & Farrell, G. Overview of Fiber Optic Sensor Technologies for Strain/Temperature Sensing Applications in Composite Materials. *Sensors* **16**, 99 (2016).

44. Ruan, T., Chew, Z. J. & Zhu, M. Energy-Aware Approaches for Energy Harvesting Powered Wireless Sensor Nodes. *IEEE Sens. J.* **17**, 2165–2173 (2017).

45. Chew, Z. J., Ruan, T. & Zhu, M. Energy Harvesting Powered Wireless Sensor Nodes With Energy Efficient Network Joining Strategies. in *IEEE International Conference on Industrial Informatics, INDIN'19* (IEEE, 2019). doi:http://hdl.handle.net/10871/37398

46. Chew, Z. J., Ruan, T. & Zhu, M. Strain Energy Harvesting Powered Wireless Sensor System Using Adaptive and Energy - Aware Interface for Enhanced Performance. *IEEE Trans. Ind. Informatics* (2017). doi:10.1109/TII.2017.2710313

47. Lesieutre, G. A., Ottman, G. K. & Hofmann, H. F. Damping as a result of piezoelectric energy harvesting. *J. Sound Vib.* **269**, 991–1001 (2004).

48. Lucia, B., Balaji, V., Colin, A., Maeng, K. & Ruppel, E. Intermittent Computing: Challenges and Opportunities. *SNAPL* 1–8 (2017). doi:10.4230/LIPIcs.SNAPL.2017.8

49. Colin, A. & Lucia, B. Chain: tasks and channels for reliable intermittent programs. *Proc. 2016 ACM SIGPLAN Int. Conf. Object-Oriented Program. Syst. Lang. Appl. - OOPSLA 2016* 514–530 (2016). doi:10.1145/2983990.2983995

50. Zhang, H., Corr, L. R. & Ma, T. Issues in vibration energy harvesting. *J. Sound Vib.* **421**, 79–90 (2018).

51. Harne, R. L. & Wang, K. W. A review of the recent research on vibration energy harvesting via bistable systems. *Smart Mater. Struct.* **22**, (2013).

52. Uchino, K. Piezoelectric Energy Harvesting Systems—Essentials to Successful Developments. *Energy Technol.* **6**, 829–848 (2018).

53. Marin, A. *et al.* Mechanical Energy Harvesting for Powering Distributed Sensors and Recharging Storage Systems. (Virginia Tech, 2013).

54. Sahu, G., Sen, P. K., Sharma, R. & Bohidar, S. A Review on Power Generation Using Piezoelectric Material. *Int. J. Res.* **02**, 732–739 (2015).

55. Li, Q., Kuang, Y. & Zhu, M. Auxetic piezoelectric energy harvesters for increased electric power output. *AIP Adv.* **015104**, (2017).

56. Pozzi, M., Canziani, A., Durazo-Cardenas, I. & Zhu, M. Experimental characterisation of macro fibre composites and monolithic piezoelectric transducers for strain energy harvesting. in *Smart Structures (NDE)* **8438**, 834832 (2012).

57. Pozzi, M., Guo, S. & Zhu, M. Harvesting energy from the dynamic deformation of an aircraft wing under gust loading. *Proc. SPIE Heal. Monit. Struct. Biol. Syst. 8348 Smart Struct. 2012* pp834831-1/11 (2012). doi:10.1117/12.917039

58. Duarte, F., Casimiro, F., Correia, D., Mendes, R. & Ferreira, A. Waynergy people : a new pavement energy harvest system. *Munic. Eng.* **166**, 1–7 (2013).

59. PaveGen. PaveGen. (2017). Available at: http://www.pavegen.com/product. (Accessed: 23rd October 2017)

60. Zheng, Y. H., Li, Y. F., Wang, S. W. & Zhao, Y. Experiment on yield strength of PZT-4 piezoelectric generating column. *Appl. Mech. Mater.* **441**, 62–65 (2014).

61. Moheimani, S. O. R. & Fleming, A. J. *Piezoelectric Transducers for Vibration Control and Damping*. (Springer, 2006). doi:10.1007/1-84628-332-9

62. Bassani, G., Jean-Mistral, C. & Ruffaldi, E. Development of an auxetic frame for scavenging human kinetic energy. in *Journées Nationales sur la Récupération et le Stockage d'Energie (JNRSE)* 10–11 (2017).

63. Roshani, H., Dessouky, S., Montoya, A. & Papagiannakis, A. T. Energy harvesting from asphalt pavement roadways vehicle-induced stresses: A feasibility study. *Appl. Energy* **182**, 210–218 (2016).

64. Jamieson, P. *et al. Energy Harvesting_ Solar, Wind, and Ocean Energy Conversion Systems (Energy, Power Electronics, and Machines) (2009)*. *Renewable Energy* **2013**, (CRC Press, 2009).

65. Rostami, A. B. & Armandei, M. Renewable energy harvesting by vortex-induced motions: Review and benchmarking of technologies. *Renew. Sustain. Energy Rev.* **70**, 193–214 (2017).

66. Orrego, S. *et al.* Harvesting ambient wind energy with an inverted piezoelectric flag. *Appl. Energy* **194**, 212–222 (2017).

67. Haidar, A. M. A., Senan, M. F. M., Noman, A. & Radman, T. Utilization of pico hydro generation in domestic and commercial loads. *Renew. Sustain. Energy Rev.* **16**, 518–524 (2012).

68. Manzano-Agugliaro, F., Taher, M., Zapata-Sierra, A., Juaidi, A. & Montoya, F. G. An overview of research and energy evolution for small hydropower in Europe. *Renew. Sustain. Energy Rev.* **75**, 476–489 (2017).

69. Lucid Energy. Spinning Gravity Into Renewable Energy. (2017). Available at: http://lucidenergy.com. (Accessed: 17th February 2020)

70. Wang, Z. L., Chen, J. & Lin, L. Progress in triboelectric nanogenerators as a new energy technology and self-powered sensors. *Energy Environ. Sci.* **8**, 2250–2282 (2015).

71. Teklu, A. A. & Sullivan, R. M. A prototype DC triboelectric generator for harvesting energy from natural environment. *J. Electrostat.* **86**, 34–40 (2017).

72. Su, Y. *et al.* Hybrid triboelectric nanogenerator for harvesting water wave energy and as a self-powered distress signal emitter. *Nano Energy* **9**, 186–195 (2014).

73. Gupta, V., Kandhalu, A. & Rajkumar, R. (Raj). Energy harvesting from electromagnetic energy radiating from AC power lines. in *Proceedings of the 6th Workshop on Hot Topics in Embedded Networked Sensors - HotEmNets '10* 1 (ACM New York, 2010). doi:10.1145/1978642.1978664

74. Wang, K., Sanders, S. R., Dubey, S., Choo, F. H. & Duan, F. Stirling cycle engines for recovering low and moderate temperature heat: A review. *Renew. Sustain. Energy Rev.* **62**, 89–108 (2016).

75. Ikeda, T. *Fundamentals of Piezoelectricity*. (Oxford Science Publications, 1990). doi:10.1524/zkri.1992.199.1-2.158

76. Qin, Q. H. *Advanced mechanics of piezoelectricity*. *Advanced Mechanics of Piezoelectricity* (2013). doi:10.1007/978-3-642-29767-0

77. Jaffe, B., R. Cook Jr., W. & Jaffe, H. *Piezoelectric Ceramics*. *Piezoeletric ceramics* **3**, (Academic Press Inc., 1971).

78. Zak, A. K., Chen, G. W. & Majid, W. H. A. Dielectric properties of PVDF/PZT. *AIP Conf. Proc.* **1328**, 238–240 (2011).

79. Fang, L., Li, J., Zhu, Z., Orrego, S. & Kang, S. H. Piezoelectric polymer thin films with architected cuts. *J. Mater. Res.* **33**, 330–342 (2018).

80. Malič, B. *et al.* Sintering of lead-free piezoelectric sodium potassium niobate ceramics. *Materials (Basel).* **8**, 8117–8146 (2015).

81. Topolov, V. Y. & Bowen, C. R. High-performance 1-3-type lead-free piezo-composites with auxetic polyethylene matrices. *Mater. Lett.* **142**, 265–268 (2015).

82. Clementi, G. *et al.* Characterization of Lead-Free LiNbO3 Vibrational Energy

Harvesters. in *2019 Micro and Nanotechnology for Power Generation and Energy Conversion Applications (Power MEMS)* (2019).

83. Sohn, J. I. *et al.* Engineering of efficiency limiting free carriers and an interfacial energy barrier for an enhancing piezoelectric generation. *Energy Environ. Sci.* **6**, 97 (2013).

84. Malakooti, M. H., Patterson, B. A., Hwang, H.-S. & Sodano, H. A. ZnO nanowire interfaces for high strength multifunctional composites with embedded energy harvesting. *Energy Environ. Sci.* **2**, 634–643 (2016).

85. Kim, H. *et al.* Enhancement of piezoelectricity via electrostatic effects on a textile platform. *Energy Environ. Sci.* **5**, 8932 (2012).

86. Bischur, E. & Schwesinger, N. Piezoelectric PVDF film energy harvester for powering a wireless sensor system. **8688**, 868804-868804–6 (2013).

87. Pi, Z., Zhang, J., Wen, C., Zhang, Z. bin & Wu, D. Flexible piezoelectric nanogenerator made of poly(vinylidenefluoride-co-trifluoroethylene) (PVDF-TrFE) thin film. *Nano Energy* **7**, 33–41 (2014).

88. Kuang, Y. & Zhu, M. Evaluation and validation of equivalent properties of macro fibre composites for piezoelectric transducer modelling. *Compos. Part B Eng.* (2018). doi:10.1016/j.compositesb.2018.09.068

89. Smart Material. MFC. (2017). Available at: https://www.smart-material.com/MFC-product-main.html. (Accessed: 24th October 2017)

90. Upadrashta, D. & Yang, Y. Experimental investigation of performance reliability of macro fiber composite for piezoelectric energy harvesting applications. *Sensors Actuators, A Phys.* **244**, 223–232 (2016).

91. Yang, Z. & Zu, J. Comparison of PZN-PT, PMN-PT single crystals and PZT ceramic for vibration energy harvesting. *Energy Convers. Manag.* **122**, 321–329 (2016).

92. Guillon, O., Thiebaud, F. & Perreux, D. Tensile fracture of soft and hard PZT. *Int. J. Fract.* **117**, 235–246 (2002).

93. Fett, T., Munz, D. & Thun, G. Tensile and bending strength of piezoelectric ceramics. *J. Mater. Sci. Lett.* **18**, 1899–1902 (1999).

94. Li, J. F., Wang, K., Zhang, B. P. & Zhang, L. M. Ferroelectric and piezoelectric properties of fine-grained Na 0.5K 0.5NbO 3 lead-free piezoelectric ceramics prepared by spark plasma sintering. *J. Am. Ceram. Soc.* **89**, 706–709 (2006).

95. Wang, K., Zhang, B.-P., Li, J.-F. & Zhang, L.-M. Lead-free Na0.5K0.5NbO3

piezoelectric ceramics fabricated by spark plasma sintering: Annealing effect on electrical properties. *J. electroceramics* **21**, 251–254 (2008).

96. Smart Material. Macro Fiber Composite (MFC). 8 (2014).

97. Sirohi, J. & Chopra, I. Fundamental Understanding of Piezoelectric Strain Sensors. *J. Intell. Mater. Syst. Struct.* **11**, 246–257 (2000).

98. De Bellis, M. L. & Bacigalupo, A. Auxetic behavior and acoustic properties of microstructured piezoelectric strain sensors. *Smart Mater. Struct.* 28 (2017). doi:10.1088/1361-665X/aa7772

99. Iyer, S., Alkhader, M. & Venkatesh, T. A. Electromechanical behavior of auxetic piezoelectric cellular solids. *Scr. Mater.* **99**, 65–68 (2015).

100. Fey, T. *et al.* Mechanical and electrical strain response of a piezoelectric auxetic PZT lattice structure. *Smart Mater. Struct.* **25**, 015017 (2016).

101. Evans, K. E., Nkansah, M. A., Hutchinson, I. J. & Rogers, S. C. Molecular network design. *Nature* **353**, 124–124 (1991).

102. Alderson, A. A triumph of lateral thought. *Chemistry and Industry* **10**, 384–391 (1999).

103. Mir, M., Ali, M. N., Sami, J. & Ansari, U. Review of mechanics and applications of auxetic structures. *Adv. Mater. Sci. Eng.* **2014**, 1–18 (2014).

104. Saxena, K. K., Das, R. & Calius, E. P. Three Decades of Auxetics Research - Materials with Negative Poisson's Ratio: A Review. *Adv. Eng. Mater.* **18**, 1847–1870 (2016).

105. Lim, T. C. Analogies across auxetic models based on deformation mechanism. *Phys. Status Solidi - Rapid Res. Lett.* **11**, (2017).

106. Alderson, K., Alderson, A., Ravirala, N., Simkins, V. & Davies, P. Manufacture and characterisation of thin flat and curved auxetic foam sheets. *Phys. Status Solidi Basic Res.* **249**, 1315–1321 (2012).

107. Grima, J. N. & Gatt, R. Perforated sheets exhibiting negative Poisson's ratios. *Adv. Eng. Mater.* **12**, 460–464 (2010).

108. Pozniak, A. A., Wojciechowski, K. W., Grima, J. N. & Mizzi, L. Planar auxeticity from elliptic inclusions Artur. *Malays. J. Microbiol.* **12**, 177–181 (2016).

109. Bianchi, M. & Scarpa, F. Vibration transmissibility and damping behaviour for auxetic and conventional foams under linear and nonlinear regimes. *Smart Mater. Struct.* **22**, 084010 (2013).

110. Bhullar, S. K. Three decades of auxetic polymers: A review. *E-Polymers* **15**, 205–215 (2015).

111. Masters, I. G. & Evans, K. E. Models for the elastic deformation of honeycombs. *Compos. Struct.* **35**, 403–422 (1996).

112. Mizzi, L., Azzopardi, K. M., Attard, D., Grima, J. N. & Gatt, R. Auxetic metamaterials exhibiting giant negative Poisson's ratios. *Phys. Status Solidi - Rapid Res. Lett.* **9**, 425–430 (2015).

113. De Bellis, M. L. & Bacigalupo, A. Auxetic behavior and acoustic properties of microstructured piezoelectric strain sensors. *Smart Mater. Struct.* **26**, (2017).

114. Cabras, L. & Brun, M. Auxetic two-dimensional lattices with Poisson's ratio arbitrarily close to - 1. *Proc. R. Soc. A Math. Phys. Eng. Sci.* **470**, 1–26 (2014).

115. Smith, C. W., Grima, J. N. & Evans, K. E. Novel mechanism for generating auxetic behaviour in reticulated foams: Missing rib foam model. *Acta Mater.* **48**, 4349–4356 (2000).

116. Körner, C. & Liebold-Ribeiro, Y. A systematic approach to identify cellular auxetic materials. *Smart Mater. Struct.* **24**, 025013 (2015).

117. Alderson, K. L., Webber, R. S. & Evans, K. E. Novel variations in the microstructure of auxetic ultra-high molecular weight polyethylene. Part 2: Mechanical properties. *Polym. Eng. Sci.* **40**, 1906–1914 (2000).

118. Umino, Y., Tsukamoto, T., Shiomi, S., Yamada, K. & Suzuki, T. Development of vibration energy harvester with 2D mechanical metamaterial structure. in *Power MEMS 2017* (ed. Suzuki, F.) 1–4 (Power MEMS, 2017).

119. Rafsanjani, A. & Pasini, D. Bistable auxetic mechanical metamaterials inspired by ancient geometric motifs. *Extrem. Mech. Lett.* **9**, 291–296 (2016).

120. Mousanezhad, D. *et al.* Hierarchical honeycomb auxetic metamaterials. *Sci. Rep.* **5**, 18306 (2015).

121. Bertoldi, K., Vitelli, V., Christensen, J. & Van Hecke, M. Flexible mechanical metamaterials. *Nat. Rev. Mater.* **2**, (2017).

122. Nike. The New Dimensions of Nike Free. *Nike News* (2016). Available at: https://news.nike.com/news/nike-free-2016-running-training. (Accessed: 12th October 2017)

123. Hu, H. & Zulifqar, A. Auxetic Textile Materials - A review. *J. Text. Eng. Fash. Technol.* **1**, 1–20 (2016).

124. Zhang, G., Ghita, O. & Evans, K. E. The manufacture and mechanical properties

of a novel negative Poisson's ratio 3-component composite. *20th Internaional Conf. Compos. Mater.* 19–24 (2015).

125. Miller, W., Hook, P. B., Smith, C. W., Wang, X. & Evans, K. E. The manufacture and characterisation of a novel, low modulus, negative Poisson's ratio composite. *Compos. Sci. Technol.* **69**, 651–655 (2009).

126. Wright, J. R., Burns, M. K., James, E., Sloan, M. R. & Evans, K. E. On the design and characterisation of low-stiffness auxetic yarns and fabrics. *Text. Res. J.* **82**, 645–654 (2012).

127. Hammetter, C., Rinaldi, R. & Zok, F. Pyramidal Lattice Structures for High Strength and Energy Absorption. *J. Appl. Mech.* **1**, 407 (2012).

128. Chandrasekharan, N. & Thompson, L. L. Increased power to weight ratio of piezoelectric energy harvesters through integration of cellular honeycomb structures. *Smart Mater. Struct.* **25**, 045019 (2016).

129. Adeshara, J. Design optimization of geometrical parameters and material properties of vibrating bimorph cantilever beams with solid and honeycomb substrates for maximum. *All Theses. Pap. 1717.* (2013).

130. Kwon, S. C. & Oh, H. U. Experimental validation of satellite micro-jitter management strategy in energy harvesting and vibration isolation. *Sensors Actuators A Phys. A Phys.* **249**, 172–185 (2016).

131. Bowen, C. R., Betts, D. N., Kim, H. A. & Yu. Topolov, V. 2-2 composites based on [011]-poled relaxor-ferroelectric single crystals: Analysis of the piezoelectric anisotropy and squared figures of merit for energy harvesting applications. *Microsyst. Technol.* **20**, 709–717 (2014).

132. Brownjohn, J. M. W., Stefano, A. De, Helmut, Y. X. & Emin, W. A. Vibration-based monitoring of civil infrastructure : challenges and successes. 79–95 (2011). doi:10.1007/s13349-011-0009-5

133. Physik Instrumente. Piezo Material Data. (2011). Available at: http://www.pi-usa.us/tutorial/Piezo_Material_Datasheet_Cofefficients_Temperature_Measurements.pdf.

134. 3M. Adhesives DP460 Off-White and DP460NS. 1–8 (2017).

135. CFS Fibreglass. Resin Proof Tape 50mm wide. *CFSNET* Available at: https://www.cfsnet.co.uk/acatalog/Resin-Proof-Tape-50mm-wide-TTACEL_050.html. (Accessed: 6th May 2019)

136. APC. Physical and Piezoelectric Properties of APC Materials. 841–842 (2019).

137. Nelder, J. A. & Mead, R. A Simplex Method for Function Minimization. *Comput. J.* **7**, 308–313 (1965).

138. Shi, Y., Hallett, S. R. & Zhu, M. Energy harvesting behaviour for aircraft composites structures using macro-fibre composite: Part I – Integration and experiment. *Compos. Struct.* **160**, 1279–1286 (2017).

139. Grima, J. N. & Evans, K. E. Auxetic behavior from rotating squares. *J. Mater. Sci. Lett.* **19**, 1563–1565 (2000).

140. Grima, J. N., Zammit, V., Gatt, R., Alderson, A. & Evans, K. E. Auxetic behaviour from rotating semi-rigid units. *Phys. Status Solidi Basic Res.* **244**, 866–882 (2007).

141. Grima, J. N., Gatt, R., Alderson, A. & Evans, K. E. On the auxetic properties of 'rotating rectangles' with different connectivity. *J. Phys. Soc. Japan* **74**, 2866–2867 (2005).

142. Shan, S., Kang, S. H., Zhao, Z., Fang, L. & Bertoldi, K. Design of planar isotropic negative Poisson's ratio structures. *Extrem. Mech. Lett.* **4**, 96–102 (2015).

143. Mizzi, L. *et al.* Mechanical metamaterials with star-shaped pores exhibiting negative and zero Poisson's ratio. *Mater. Des.* **146**, 28–37 (2018).

144. Gostimirović, M., Kovač, P., Sekulić, M., Rodić, D. & Pucovsky, V. Machining Characteristics of Electrical Discharge Machining – a Review. *J. Prod. Eng.* **19**, (2016).

145. Kar, C., Surekha, B., Jena, H. & Choudhury, S. D. Study of Influence of Process Parameters in Electric Discharge Machining of Aluminum - Red Mud Metal Matrix Composite. in *Procedia Manufacturing* **20**, 392–399 (Elsevier B.V., 2018).

146. Patel, J. D. & Maniya, K. D. A Review on: Wire cut electrical discharge machining process for metal matrix composite. *Procedia Manuf.* **20**, 253–258 (2018).

147. Horodek, P., Eseev, M. K. & Kobets, A. G. Studies of stainless steel exposed to sandblasting. *Nukleonika* **60**, 721–724 (2015).